A Multi-scale Radio Study of Gamma-ray Burst Afterglows

James K. Leung

A thesis submitted in fulfilment of the requirements for the degree of

Doctor of Philosophy (PhD)

THE UNIVERSITY OF SYDNEY

The University of Sydney
Faculty of Science
School of Physics

November 8, 2023

For my dearest Grandmas

Statement of Originality

This is to certify that to the best of my knowledge, the content of this thesis is my own work. This thesis has not been submitted for any degree or other purposes.

I certify that the intellectual content of this thesis is the product of my own work and that all the assistance received in preparing this thesis and sources have been acknowledged.

James K. Leung

November 8, 2023

Authorship Attribution Statement

I confirm that the authorship attribution statements given in the Preface and at the beginning of each chapter are correct to the best of my knowledge.

James K. Leung

November 8, 2023

As supervisor for the candidature upon which this thesis is based, I confirm that the originality and authorship attribution statements given above, in the Preface, and at the beginning of each chapter are correct.

Prof. Tara Murphy

November 8, 2023

Abstract

The radio afterglows of gamma-ray bursts (GRBs) reveal important details about the properties of the blast wave and the circumburst environment, while also lending themselves as cosmic laboratories for studying physics in the most extreme environments of the Universe. In this thesis, I demonstrate how modern radio interferometry on different angular scales — from wide-field surveys conducted with the Australian SKA Pathfinder (ASKAP) to high-resolution observations performed through Very Long Baseline Interferometry (VLBI) — can help answer some of the important open questions about GRBs and their afterglows.

I present a targeted search for radio emission from all long GRB afterglows located in the Rapid ASKAP Continuum Survey footprint. I show the resulting detection of late-time radio emission from the low-luminosity GRB 171205A, the first confirmed detection of a radio afterglow in a wide-field radio survey, with subsequent observations and analysis revealing a circumburst environment shaped by pre-explosion stellar winds. I describe a novel matched-filter approach to finding orphan afterglows in the multi-epoch ASKAP Variables and Slow Transients Pilot Survey. The matched-filter search yielded five candidates, including one synchrotron transient candidate, VAST J175036.1−181454, which I interpreted as either a likely off-axis GRB or tidal disruption event. I outline the radio observing campaign for the ultra-long GRB 220627A, which included VLBI observations aimed at testing a possible gravitational lensing scenario. While the VLBI observations were inconclusive, partly due to insufficient sensitivity, the wider observing campaign helped to characterise the properties of the ultra-long GRB radio afterglow, of which only a handful have been previously studied. I conclude by summarising the body of work in this thesis and describing avenues of future research that have been enabled by this work.

This thesis was primarily written at my home and at the University of Sydney, on the land of the Dharawal and Gadigal people respectively. The work presented in this thesis uses observations from the Australia Telescope Compact Array, which stands on the land of the Gomeroi people, and the Australian SKA Pathfinder, which stands on the land of the Wajarri Yamatji people.

Preface

This thesis started off as an exploration of what the Australian SKA Pathfinder (ASKAP; Johnston et al., 2007) was capable of achieving for the advancement of gamma-ray burst (GRB) science.

It coincided with the launch of the first ASKAP radio survey, the Rapid ASKAP Continuum Survey (RACS; McConnell et al., 2020) in 2019. Much of the early work of this thesis was put into commissioning for the survey, focused on ensuring the data quality was sufficient for scientific use.

The timing of this thesis also coincided with exciting developments in GRB science that were enabled by radio interferometry. Very Long Baseline Interferometry (VLBI) provided critical evidence supporting an off-axis structured jet interpreation for the first multi-messenger gravitational-wave event, GW170817 and GRB 170817A (Mooley et al., 2018; Ghirlanda et al., 2019). Reports of orphan afterglow candidates (e.g., FIRST J141918.9+394036; Law et al., 2018) were also surfacing from searches in much more sensitive wide-field surveys, such as the VLA Sky Survey (VLASS). Given the improvements in instantaneous sensitivity and field-of-view from instrumental developments in ASKAP, the natural next step of exploration was to seek out whether routine, unbiased, ASKAP surveys could contribute to the search for and monitoring of radio afterglows.

This became the core work of this thesis: I had conducted both targeted and untargeted searches for radio afterglows in ASKAP data, resulting in the discovery of late-time radio emission from GRB 171205A and the discovery of a possible off-axis GRB afterglow. Following these discoveries, this thesis had since evolved into a broader work, a multi-wavelength and multi-scale attempt to better understand GRB phenomena. This work is therefore aptly titled: *A Multi-scale Radio Study of Gamma-ray Burst Afterglows.*

It is important to recognise the tremendous support I had from my supervisors and colleagues in shaping this thesis. Broadly speaking, my supervisors Prof Tara Murphy and Dr Emil Lenc have provided general supervision and guidance — both scientific and professional in nature — that unvariably shaped every aspect of this thesis. For Chapters 2 and 3, in particular, Dr Giancarlo Ghirlanda and Prof David Kaplan provided valuable scientific advice that shaped many aspects of the findings presented in those chapters. More specific contributions, where applicable, are detailed at the beginning of each chapter. I outline in the following pages a brief summary of the publications that resulted from the work of this thesis.

This thesis contains two peer-reviewed publications and one that will be submitted for publication.

> Chapter 2 has been published as *"A search for radio afterglows from gamma-ray bursts with the Australian Square Kilometre Array Pathfinder"* in Leung J. K., et al., 2021a, MNRAS, 503, 1847
>
> Chapter 3 has been published as *"A matched-filter approach to radio variability and transients: searching for orphan afterglows in the VAST Pilot Survey"* in Leung J. K., et al., 2023a, MNRAS, 523, 4029
>
> Chapter 4 currently prepared under the working title *"The radio afterglow of ultra-long gamma-ray burst GRB 220627A"* is planned to be submitted to the Monthly Notices of the Royal Astronomical Society

In addition to these thesis chapters, I also list here 15 peer-reviewed publications from other work that I had completed as part of this thesis as a coauthor. The following publications relate to work done as part of the RACS commissioning team:

> McConnell D., et al., 2020, *"The Rapid ASKAP Continuum Survey I: Design and first results"*, PASA, 37, e048
>
> Hale C. L., et al., 2021, *"The Rapid ASKAP Continuum Survey Paper II: First Stokes I Source Catalogue Data Release"*, PASA, 38, e058
>
> Duchesne S. W., et al., 2023, *"The Rapid ASKAP Continuum Survey IV: continuum imaging at 1367.5 MHz and the first data release of RACS-mid"*, PASA, 40, e034

The following publications relate to work done on the study of high-redshift radio galaxies, which was an extension arising from the RACS work:

> Ighina L., et al., 2022, *"Constraining the radio properties of the $z = 6.44$ QSO VIK J2318−3113"*, A&A, 663, A73
>
> Ighina L., et al., 2023, *"New radio-loud QSOs at the end of the Reionization epoch"*, MNRAS, 519, 2060

The following publications relate to work done on the study of variables and transients, including but not limited to the study of gamma-ray bursts, radio stars, pulsars and classical novae:

> Pritchard J., et al., 2021, *"A circular polarization survey for radio stars with the Australian SKA Pathfinder"*, MNRAS, 502, 5438
>
> Wang Z., et al., 2021, *"Discovery of ASKAP J173608.2-321635 as a Highly Polarized Transient Point Source with the Australian SKA Pathfinder"*, ApJ, 920, 45
>
> Murphy T., et al., 2021, *"The ASKAP Variables and Slow Transients (VAST) Pilot Survey"*, PASA, 38, e054

Dobie D., et al., 2022, *"A comprehensive search for the radio counterpart of GW190814 with the Australian Square Kilometre Array Pathfinder"*, MNRAS, 510, 3794

Wang Z., et al., 2022, *"A pilot ASKAP survey for radio transients towards the Galactic Centre"*, MNRAS, 516, 5972

Dobie D., et al., 2023, *"Radio transients and variables in the tenth Deeper, Wider, Faster observing run"*, MNRAS, 519, 4684

Bright J. S., et al., 2023, *"Precise Measurements of Self-absorbed Rising Reverse Shock Emission from Gamma-ray Burst 221009A"*, accepted for publication in Nat. Astron.

Gulati A., et al., 2023, *"Classical novae in the ASKAP pilot surveys"*, PASA, 40, e025

Driessen L. N., et al., 2023, *"Detection of radio emission from stars via proper-motion searches"*, PASA, 40, e036

Duchesne A., et al., 2023, *"Characterizing Pulsars Detected in the Rapid ASKAP Continuum Survey"*, accepted for publication in ApJ

I also include in Appendices A and B notices I had submitted to the General Coordinates Network[1] (GCN) and The Astronomer's Telegram (ATel), respectively. These submissions were the result of work I had completed as part of this thesis.

[1] Previously known as the Gamma-ray Coordinates Network

Acknowledgements

Many incredible people have supported me throughout my candidature and I am very thankful for each and every one who did. They nurtured me into the scientist I am today, and without them, this thesis would not exist.

My biggest supporters are my supervisors, Tara Murphy and Emil Lenc, and I am not sure I know how to sufficiently express my deep gratitude for both of them over the years. Tara, thank you for believing that I'd be capable of doing great science when I had my own doubts, for supporting every one of my wild ideas or travel plans, for connecting me with wonderful people near and far, but most importantly, for providing a stable environment for me to establish my own scientific identity. You are and continue to be a great role model; you showed me how to conduct myself as a member of the scientific and broader community in a way that is consistent with my own values. Emil, you're an absolute data guru! You have taught me so much in the art of radio astronomy and in the philosophy of paronomasia (which is, of course, the more important of the two). Your humility is inspiring; your patience (even when I ask you how to sort things in alphabetical order) and approachability is why I feel confident in asking you every small question I can think of, and the subtlety to every answer you give has made me that much better of a scientist; I am very grateful. I consider myself extremely lucky to have had the privilege of being supervised by the both of you. I'm proud that we overcame many challenges together, not least a global pandemic and even a project derailed unexpectedly by a volcano! I hope both of you see that any successes I may have are yours too.

I also want to thank David Kaplan for always being readily available to support my scientific endeavours, being full of great advice, enthusiasm and energy.

To Giancarlo Ghirlanda, Om Sharan Salafia, Marcello Giroletti, Stefano Giarratana and Cristiana Spingola, thank you all for your kind hospitality during my research visit to Italy, I was extremely grateful for every moment I had spent there learning from you about science and your culture; you made me feel very welcome.

Giancarlo, in particular, I owe much of what I know about GRBs to you. I am constantly inspired by your never-ending curiosity, enthusiasm and patience — discussing science with you has given me much joy these few years. I particularly appreciate the many times you've gotten up (very) early to videocall to accommodate the timezone difference and I am very grateful for this. Thank you for showing me the *pizzocheri*, for the nice tour of the historical telescopes and sites at Merate, and of course, for demonstrating how to convert generous amounts of *caffè* into (equally generous amounts of) research output.

To all the PhD students and postdocs in the group, both previous and continuing, thank you for the office memories, the Slack memeries, and the Atom Thai celebratories; my PhD experience was enriched one way or another by each one of you. Andrew Zic, thank you for taking the time one sunny afternoon to go on a two hour rant to me about radio astronomy; I considered that discussion to have been quite formational to my understanding of radio astronomy when I was feeling quite confused. Kovi Rose, thank you for taking the time to proofread parts of this thesis, for sharing my avid fandom for hoops and JWST mirrors, and for the many Thursday night vegetarian dinners. Ziteng "Andy" Wang, thank you for sharing the entire journey with me, from the many research projects and discussions we have together, to the many classes we have taught together, and of course, to our shared obsession with SBIDs.

School teachers over the years often go underappreciated — I want to thank Mrs Moon, Ms Contos, Mr Hughes, Mr "Trev" Trotman — they inspired me to dream, to think, and equipped me with the skills I needed for success in research.

Most importantly, I want to thank my family, who I love unconditionally — it's only with their love and support any of this was possible... still, who would have thought I'd end up with a PhD in astronomy?

This thesis is dedicated to my two late grandmothers, who both passed as I was completing this work. *Mama* always gave me her time and energy, even when she had none left. *Popo* taught me how to care deeply, how to smile even when the clouds are grey, and always encouraged me to live my best life. I will never forget how loved I am, and that motivates me to push forward every day, to be the best and truest version of myself. I would like to think this thesis would have made both of you proud. And yes, I will live my best life.

All that is gold does not glitter,
Not all those who wander are lost;
The old that is strong does not wither,
Deep roots are not reached by the frost.
From the ashes a fire shall be woken,
A light from the shadows shall spring;
Renewed shall be blade that was broken,
The crowless again shall be king.

— J. R. R. Tolkien

Contents

List of Figures

List of Tables

Chapter 1

Introduction

Most astrophysical systems and processes occurring in the Universe — from planetary formation to galaxy evolution — evolve on timescales much longer than the human lifetime. However, a small subset of these astrophysical systems known as variables or transients evolve on much shorter timescales — from milliseconds to years. The real-time study of astrophysical processes from these dynamic systems constitutes the field known as time-domain astronomy.

Variable and transient astrophysical phenomena have been observed and studied since antiquity. Records of supernova observations date back to Ancient China, with the observation of SN 185, listed in the *Houhanshu* (後漢書) historical records as a "guest star" or 客星 (Zhao et al., 2006). Observations of variability in stellar systems, supernovae, comets and meteors are also evidenced in many ancient civilisations, including in Indigenous Australian knowledge systems passed down through art, ceremony and oral traditions (Norris, 2016). The naked eye, however, can only see so far: until the recent development of the telescope during the height of the Scientific Revolution, our study of astrophysical objects has mostly been limited to those located within our own Solar System or Galaxy.

In the modern era of time-domain astronomy, extragalactic astrophysical phenomena can be studied with powerful telescopes across the entire electromagnetic spectrum — for example, from X–ray with the *Fermi* Gamma-ray Space Telescope (Atwood et al., 2009; Meegan et al., 2009), optical with the Zwicky Transient Facility (Bellm et al., 2019), to radio frequencies with the Australian SKA Pathfinder (ASKAP; Johnston et al., 2007). Among the most energetic and luminous of these extragalactic classes of transients are gamma-ray bursts (GRBs); the products of core-collapse in massive stars (Hjorth et al., 2003; Stanek et al., 2003) and mergers of compact binaries (Abbott et al., 2017b). The extraordinary properties of GRBs make them important for not only understanding the evolution of these progenitor systems, but they also provide a cosmic laboratory for studying relativistic shocks (Sari et al., 1998), providing tests of general relativity (Abbott et al., 2017b), undertaking cosmological studies (Amati et al., 2008), probing the epoch of reionisation (Kistler et al., 2009), and for many other applications.

In this thesis, I demonstrate how modern radio interferometry on different angular scales — from wide-field surveys conducted with ASKAP to high-resolution observations performed through Very Long Baseline Interferometry (VLBI) — can help answer some of the important open questions about GRBs and their afterglows. In this chapter, I give a brief introduction to GRBs and radio interferometry to place the work of this thesis into context.

In Section 1.1, I provide a brief history of GRBs starting from its serendipitous discovery to the detection of the first afterglows. In Section 1.2, I discuss how the observed phenomenological divide between short-hard and long-soft bursts has led to our current understanding of which progenitor systems produce GRBs. In Section 1.3, I explain the physics of the GRB and its afterglow under the standard relativistic blast-wave model, discussing in particular how observations can be mapped to the physical properties of the GRB systems through broadband modelling. In Section 1.4, I give a brief overview of how different radio interferometry techniques, probing different angular scales, are able to provide complementary insights into the nature of the GRB systems, their environments and their wider population(s). I conclude this chapter with an overview of my thesis in Section 1.5, summarising the scientific questions each chapter attempts to answer.

1.1 A Brief History of Gamma-ray Bursts

After signing the *Nuclear Test Ban Treaty* in 1963, the United States launched the *Vela* gamma-ray satellites into orbit to ensure nuclear tests were not being conducted anywhere on Earth or in space. The serendipitous discovery of GRBs occurred in 1967 when these satellites detected a short burst of gamma-ray photons, with a temporal structure that was not consistent with radiation from nuclear testing. This result was published six years later by Klebesadel et al. (1973) alongside the reports of sixteen new bursts, which confirmed the cosmic origin of the GRBs and marked the beginning of a new field of astrophysics. An example of a light curve for one of these bursts is shown in Figure 1.1.

Progress on understanding the origins of GRBs was hindered for the two subsequent decades, primarily because both the detection rate and the ability to localise GRBs were still poor. This changed with the start of the Burst And Transient Source Experiment (BATSE; Fishman et al., 1992) in 1991, which detected $\sim$1 GRB per day and was capable of localising them to $\sim$10 degrees. The improved localisation and larger sample size immediately provided strong evidence to resolve the question of whether GRBs were Galactic or extragalactic. Early data from BATSE from a sample of 153 GRBs (Meegan et al., 1992) showed that: (a) the angular distribution of GRB events in the sky was isotropic (see Figure 1.2, *panel a.*), and (b) the cumulative measured intensity distribution of GRBs deviated away from a $-3/2$ power law, which is the value expected for a source population uniformly distributed in Euclidean space (see Figure 1.2, *panel b.*). Together, these provided the first convincing evidence that GRBs have a cosmological origin. Still, this had not completely ruled out models suggesting that GRBs originate from the Galactic halo (e.g., Podsiadlowski et al., 1995).

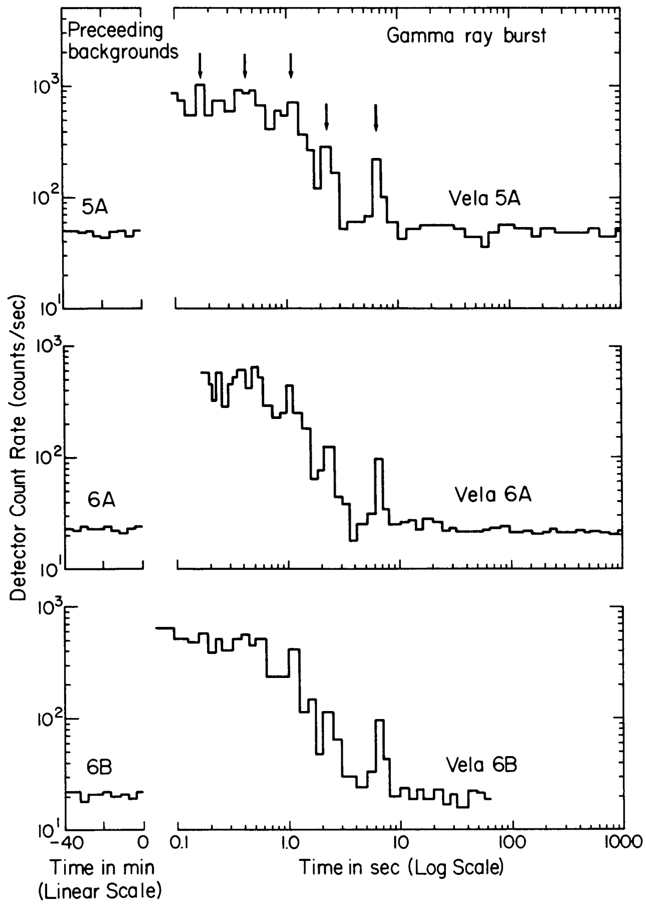

Figure 1.1: The light curve of a GRB occurring on 1970 August 22 as measured by three *Vela* satellites. This was the first GRB light curve published. Reproduced from Klebesadel et al. (1973).

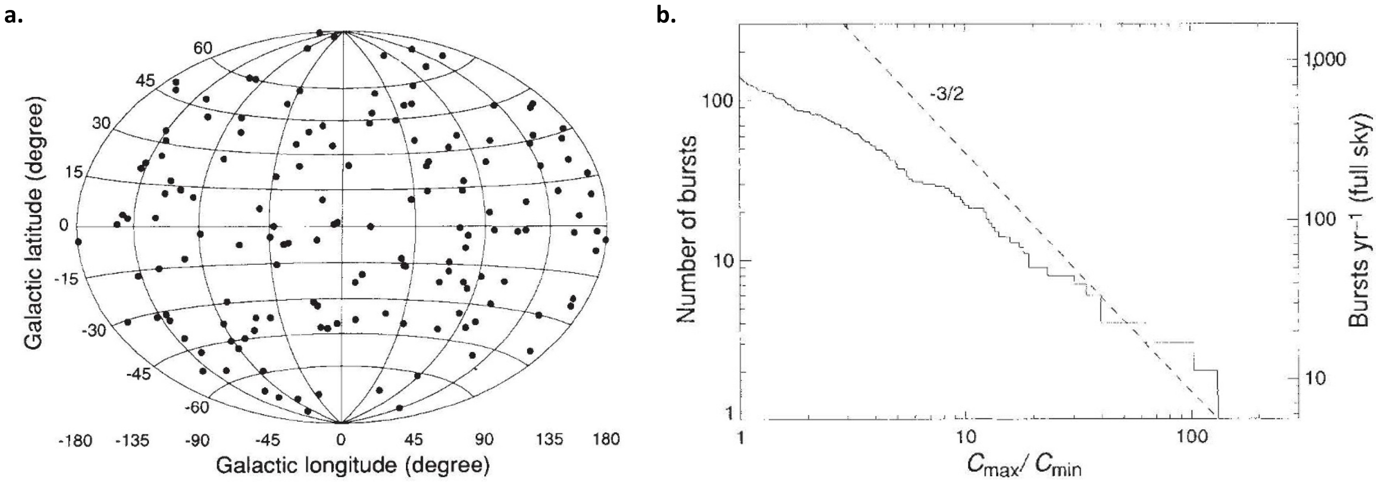

Figure 1.2: *Panel a.* — the sky distribution of 153 BATSE GRBs (displayed here in Galactic coordinates) was shown to be statistically consistent with an isotropic distribution. *Panel b.* — the cumulative distribution of the measured intensity (the peak count rate normalised by the trigger threshold count rate) for 140 BATSE GRBs was shown to have deviated from a $-3/2$ power law, which was expected for a source distribution uniformly distributed in Euclidean space. These data provided strong evidence supporting a cosmological origin for GRBs. Reproduced from Meegan et al. (1992).

The launch of the ***S**atellite per **A**stronomia a raggi **X*** (*BeppoSAX*; Boella et al., 1997) in 1996 — an Italian-Dutch X–ray satellite — was the breakthrough that settled this distance debate and ushered in the afterglow era of GRB astronomy. The ability of *BeppoSAX* to localise GRBs to a few arcminutes was instrumental to the discovery of the first afterglow. The afterglow is the emission following the initial burst of gamma-rays visible at lower energy wavelengths across the entire electromagnetic spectrum, lasting from hours to years post-burst. On 1997 Feb

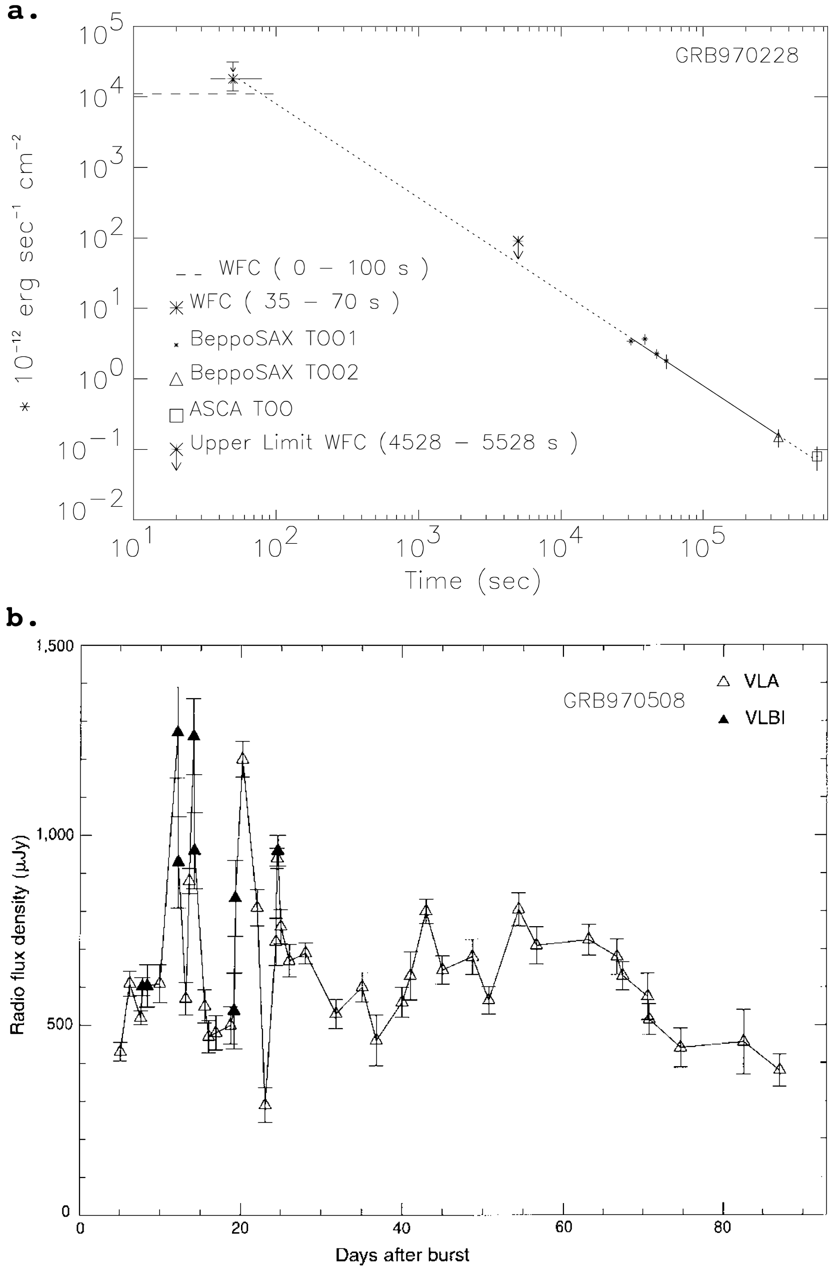

Figure 1.3: *Panel a.* — X–ray light curve for GRB 970228 taken by *BeppoSAX*, showing a power-law decay; reproduced from Costa et al. (1997a). *Panel b.* — radio light curve for GRB 970508 taken with the Very Large Array and the Very Long Baseline Array at 8.46 GHz, showing fluctuations resulting from interstellar scintillation, inconsistent with a power-law decay; reproduced from Frail et al. (1997).

28, *BeppoSAX* triggered on GRB 970228[1] and detected the first X–ray afterglow, showing for the first time an afterglow with a light curve (see Figure 1.3, *panel a.*) as a power law over a span of a few days (Costa et al., 1997a). *BeppoSAX* localised the afterglow to an error radius of $\sim 3'$ with its Wide Field Cameras (WFC), and subsequently to $\sim 1'$ with its Narrow Field Instruments (NFI), allowing for follow-up with optical telescopes. This allowed follow-up efforts to detect the optical afterglow, for the first time ever, with the William Herschel Telescope and Isaac Newton Telescope on La Palma, although a radio counterpart remained elusive (van Paradijs et al., 1997). With an optical localisation, it became apparent the GRB may have been associated with a faint host galaxy, adding further credence towards a cosmological origin for GRBs.

The next X–ray afterglow localised by *BeppoSAX* was GRB 970508 (Costa et al., 1997b). Optical spectra obtained from the Keck II 10-m telescope revealed the GRB had a redshift of $z = 0.835$, conclusively establishing GRBs as a cosmological source population (Metzger et al., 1997). A key implication of this result is that GRBs had become the brightest known class of objects in the Universe, releasing over 10^{51} erg of energy on the order of seconds (Paczynski, 1986). Aided by an enhanced *BeppoSAX* position of the X–ray afterglow (Heise et al., 1997), the Very Large Array (VLA) detected the radio counterpart to GRB 970508, which was the first detection of a GRB radio afterglow (Frail et al., 1997). This radio afterglow did not follow a simple power-law decay as was seen at shorter wavelengths; instead, it showed rapid fluctuations, which were signatures of interstellar scintillation (see Figure 1.3, *panel b.*). The dampening of these fluctuations over time pointed to rapid source size expansion and provided early evidence for relativistic outflows.

Localising and discovering the afterglow across the entire electromagnetic spectrum was therefore a key milestone leading to many breakthroughs in GRB physics. Both BATSE and *BeppoSAX* have since been superseded by the ongoing *Fermi* (Atwood et al., 2009; Meegan et al., 2009) and *Swift* (Gehrels et al., 2004) missions. I discuss our current understanding as well as ongoing research on the GRB progenitors in Section 1.2 and the physics of GRBs in Section 1.3.

1.2 The Phenomenological Divide

Another key result of the BATSE mission was the identification of two separate classes of GRBs based on their event duration and spectral hardness ratio — long and short GRBs — as shown in Figure 1.4 (Kouveliotou et al., 1993). Specifically, the event duration was defined by T_{90}, which is the time interval encompassing 90% of all GRB photon counts above the background, and the spectral hardness ratio by HR32, which is the ratio between the total counts in the 100–300 keV energy range to that in the 50–100 keV energy range. Long GRBs ($T_{90} > 2$ s) were found to have a softer spectrum, while short GRBs ($T_{90} < 2$ s) were found

[1]The GRB name reflects the date of detection in the format GRB YYMMDD. After 2010 Jan 01, due to the large volume of detections following the launch of *Fermi*, an alphabetical suffix would be appended to the string to distinguish between bursts occurring on the same day, where the first GRB of a given day would be assigned the suffix ’A’ (GRB YYMMDDA).

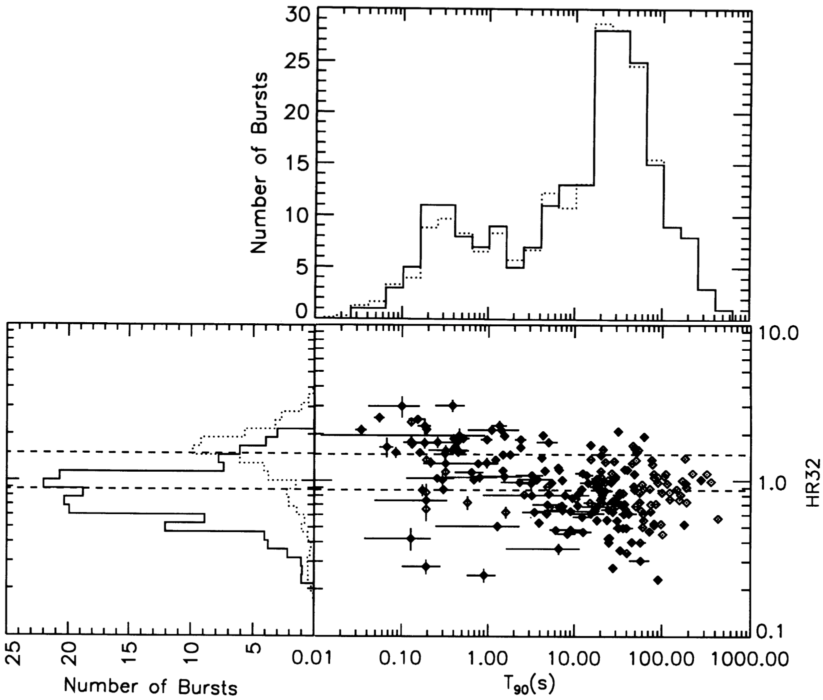

Figure 1.4: The distribution of T_{90} (event duration) and HR32 (spectral hardness ratio) for 222 BATSE GRBs. The GRBs are classified into two classes of GRBs based on their phenomenology: a long duration class ($T_{90} > 2$ s), which tends to have a softer spectrum, and a short duration class ($T_{90} < 2$ s), which tends to have a harder spectrum. For the T_{90} histogram, the solid lines represent the distribution based on the raw data, while the dotted lines represent the distribution after accounting for time errors in each bin. For the HR32 histogram, the solid lines represent the distribution for long duration GRBs, while the dotted lines represent the distribution of short duration GRBs. Reproduced from Kouveliotou et al. (1993).

to have a harder spectrum. The phenomenological distinction between these two classes suggest different underlying physical processes and origins associated with each sub-population, leading to investigations to uncover the possible progenitors for each sub-population of GRBs. It should be noted that this phenomenological divide is detector dependent; for example, while the $T_{90} = 2$ s split between the long and short GRB classification is appropriate for BATSE bursts, the divide is closer to $T_{90} = 0.8$ s for *Swift* bursts (Bromberg et al., 2013). As seen in Figure 1.4, there is also significant overlap between the measured durations of the two populations, which may point to a population of short GRBs with similar properties to typical long GRBs, and vice versa; this is discussed in more detail in Subsection 1.2.3.

1.2.1 Long Gamma-ray Bursts & Collapsars

One of the early models explaining the origin of long GRBs was the collapsar model. Proposed by Woosley (1993) and refined by MacFadyen & Woosley (1999), the model invokes a massive, rapidly-rotating, stripped-envelope Wolf-Rayet star collapsing into an accreting black hole to explain how long GRBs are produced. Under this model, the accretion disk resulting from the massive star collapse provides the energy reservoir to launch highly-relativistic and narrow jets in the polar regions of the dying star. When the jet emerges from the remaining[2] stellar material, it produces a GRB via physical processes described in Section 1.3. This model also predicts an additional observable counterpart to the GRB: an accompanying type Ic supernova. The required energy and ^{56}Ni abundance for the supernova would be provided by the jet as it pushes through the remaining stellar material, coupling to the matter at the jet boundaries, in addition to the wind from the accretion disk. The direct observable predictions that follow from this model was therefore GRBs exploding in star-forming regions (where massive stars are found) and evidence for accompanying Type Ic supernovae.

[2]Even prior to the massive star collapse, the progenitor star had lost a significant proportion of its mass through stellar winds, making it easier for the jet to penetrate.

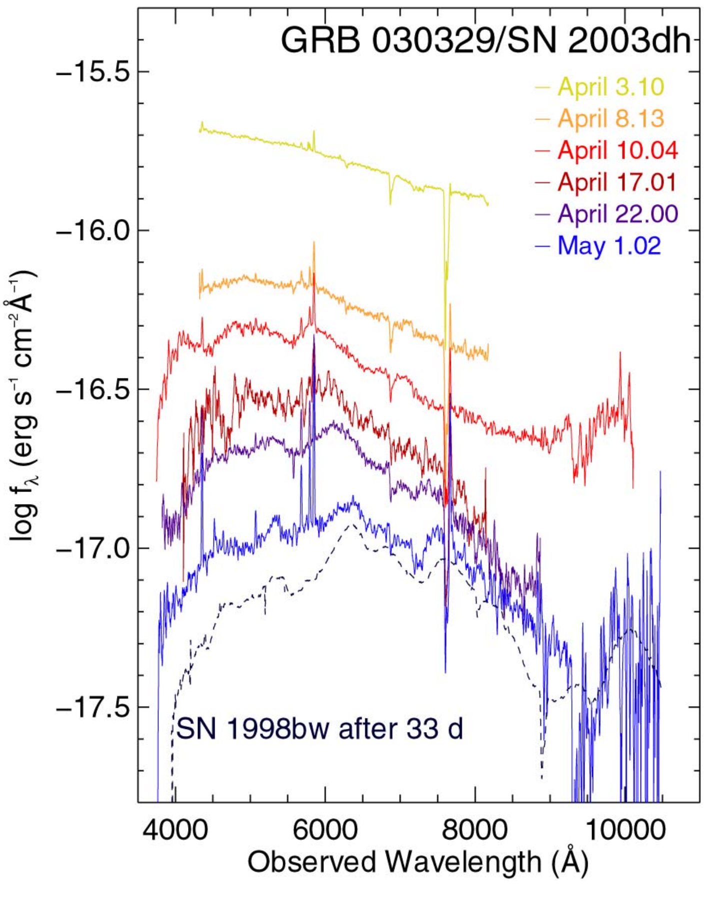

Figure 1.5: Spectral evolution of GRB 030329/SN 2003dh and its host galaxy over the span of a month, showing the optical flux density as a function of observed wavelength as taken by the Very Large Telescope FOcal Reducer/low dispersion Spectrographs. The initial spectrum was well-described by a power law, which was expected for an afterglow spectrum. Subsequent spectra started to reveal the imprints of type Ic supernova-like features and a deviation away from the power law. In particular, the broad peaks in the spectra, which suggested mildly-relativistic expansion velocities in the photosphere, were similar to those observed for SN 1998bw, whose spectrum after one month is also shown above with dashed lines. This provided spectroscopic confirmation of the GRB-SN connection, supporting the collapsar model for long GRBs. Reproduced from Hjorth et al. (2003).

The improved localisation of GRBs by *BeppoSAX* provided the early evidence supporting the collapsar model. For example, Paczyński (1998) showed that long GRBs 970228, 970508 and 970828 likely exploded in star-forming regions of host galaxies, while Bloom et al. (2002) showed with a sample of 20 long GRBs that they exploded very close (median offset of 1.3 kpc) to the centre of young host galaxies, where the star formation activity is high. More convincing evidence for the collapsar model came when the type Ic supernova SN 1998bw, located at redshift $z = 0.0085$, was observed to be located within the *BeppoSAX*-WFC localisation error box for GRB 980425 (Galama et al., 1998). However, doubt remained over the GRB-SN connection for two reasons: (a) there was lack of consensus over whether any of the *candidate* X–ray sources detected by *BeppoSAX*-NFI (no afterglow was claimed to be detected at other wavelengths) were indeed the afterglow of GRB 980425, especially since the initial reports (although subsequently revised) suggested none of the sources had coordinates consistent with the supernova position (Pian et al., 2000); and (b) its total energy released in gamma-rays was measured to be $(8.5 \pm 1.0) \times 10^{47}$ erg (Galama et al., 1998), which was at least 4 orders of magnitude lower than the sample of others GRBs known at the time, casting doubt over whether supernovae are also associated with more typical GRBs.

The unequivocal evidence for the GRB-SN connection as predicted by the collapsar model came when the spectroscopic observations of the GRB 030329 optical afterglow, located at redshift $z = 0.1685$, also revealed the imprints of a type Ic supernova, SN 2003dh, as shown in Figure 1.5 (Hjorth et al., 2003; Stanek et al., 2003). The early spectra taken for the event (e.g., April 3.10 in Figure 1.5) was consistent with a power law, which was expected from an afterglow (see Section 1.3). As the spectra evolved with time, the deviations away from the power-law spectral structure became apparent and instead started to reveal type Ic supernova-like features that was previously seen in SN 1998bw. The spectrum taken one month post-burst reveals a clear type Ic supernova spectral signature with broad peaks, suggesting high expansion velocities in the photosphere reaching 30 000 km s^{-1} or $(0.12 \pm 0.01)c$, where c is the speed of light. With a more typical gamma-ray luminosity than GRB 980425, this event confirmed the GRB-SN connection, and suggested the possibility that the low luminosity measured for GRB 980425 may have been due to viewing angle effects, i.e., observer angle from the jet axis (Waxman, 2004). The GRB-SN connection has since been well-established with numerous subsequent events, providing strong evidence supporting the massive star collapse origin for long GRBs; for a recent review, see Cano et al. (2017).

1.2.2 Short Gamma-ray Bursts & Compact Mergers

While the evidence was mounting in support of the collapsar model explaining the origin of long GRBs, the physical processes described in the collapsar model were unable to produce the shorter timescales of variability observed in short GRBs. An alternative model capable of producing the much shorter timescales of variability involved the merger of compact objects (e.g., binary neutron star merger or black hole-neutron star merger). The model was recognised as a viable option for producing GRBs (Paczynski, 1986) after it was shown by Taylor & Weisberg (1982) that the Hulse-Taylor binary pulsar, PSR 1913+16, had a decaying orbital period (and therefore will eventually produce a compact merger) due to energy loss from gravitational radiation.

In this model (Eichler et al., 1989; Narayan et al., 1992), the compact objects that make up the binary system are expected to be displaced far from their birthsites since the supernovae that produce these compact objects will impart natal kick velocities to the system[3]. Similar to the long GRB scenario, the eventual merger of the compact objects will produce an accretion disk that is able to power the narrow and highly-relativistic jet, which produces the GRB in a comparatively shorter timescale, leaving behind a black hole or a short-lived magnetar remnant. The model also predicted an additional emission component: the *kilonova* (for a review, see Metzger, 2019). The faint kilonova component, predicted to be observable at near-infrared/optical wavelengths (initially modelled in Li & Paczyński, 1998), is the result of *r*-process (rapid neutron capture) nucleosynthesis of heavy elements and the subsequent radioactive decay of unstable isotopes. Since the sources of neutron-rich material in which these processes are expected to occur are in the dynamical ejecta (e.g., material ejected due to tidal forces at the interface between the merger) and the accretion disk wind, the model predicts the kilonova emission to be un-beamed, unlike the jets. All these features provided testable predictions for the model, but the key prediction that was considered the "smoking gun" for this model was the detection of gravitational radiation from a compact merger associated with a short GRB event.

For many years, these predictions were difficult to test because the short GRBs and their afterglows were difficult to localise. This was partly because short GRBs have lower typical energies compared to long GRBs and also tend to occur in lower density environments than long GRBs (e.g., Fong et al., 2015). The launch of a more sensitive generation of satellites in the mid-2000s, in particular the Neil Gehrels *Swift* Observatory, led to immediate breakthroughs: GRB 050509B ($T_{90} = 40 \pm 4$ ms) became the first short GRB to be localised by *Swift* X–ray Telescope (XRT) to an elliptical galaxy (Gehrels et al., 2005); short GRB 050709 ($T_{90} = 70$ ms) provided the first optical afterglow detection (Hjorth et al., 2005) and was localised to a star-forming galaxy with no evidence of an accompanying supernova (Fox et al., 2005); and short GRB 050724 ($T_{90} = 3 \pm 1$ s) provided the first radio afterglow, allowing the burst to be localised to an elliptical galaxy (Berger et al., 2005). The lack of supernova association and diversity in galaxy types for this early sample of short GRBs provided evidence consistent with a compact merger origin and against the collapsar origin. Larger sample studies conducted in later years (e.g., Fong & Berger, 2013) showed that short GRBs had a median physical projected offset from their host galaxies that was significantly greater than that for long GRBs and also had the tendency to occur in regions of the host galaxy with no star formation. These findings were consistent with expectations for a compact merger origin for

[3]Recently, it has also been shown that large displacements of binary systems from their birthsites could also be explained naturally by the observation of highly-extended (but faint) underlying stellar populations in early-type galaxy halos, without the need of invoking substantial natal kick velocities (Perets & Beniamini, 2021).

short GRBs, but an unambiguous confirmation of this model required more direct evidence.

The first direct evidence of the compact merger model came with the detection of a kilonova associated with short GRB 130603B (Tanvir et al., 2013; Berger et al., 2013). As shown in Figure 1.6, the near-infrared (and not the optical) light curve at ∼10 days post-burst shows a late-time excess relative to the power-law decay expected from the afterglow emission only. This observation was consistent with a kilonova, a key prediction of the compact merger model, since the radiation was expected to emerge primarily at the near-infrared rather than optical wavelengths due to the high optical opacity caused by line blanketing (e.g., Barnes & Kasen, 2013). However, it was the multi-messenger GW170817/GRB 170817A event that led to the "smoking gun" confirmation for the compact merger model (e.g., Abbott et al., 2017b). On 2017 August 17, the Laser Interferometer Gravitational-Wave Observatory (LIGO) detected the binary neutron star gravitational wave event GW170817; after a short delay of 1.74 ± 0.05 s, both the *Fermi* and *INTEGRAL* satellites detected a temporally and spatially coincident electromagnetic counterpart, i.e., short GRB 170817A (see Figure 1.7). The joint detection of a binary neutron star gravitational wave event coincident with a short GRB event confirmed that at least a subset of short GRBs come from the merger of two neutron stars. The scientific implications of this multi-messenger event was broad: providing new tests of general relativity (e.g., Abbott et al., 2019), independent estimates of the Hubble parameter

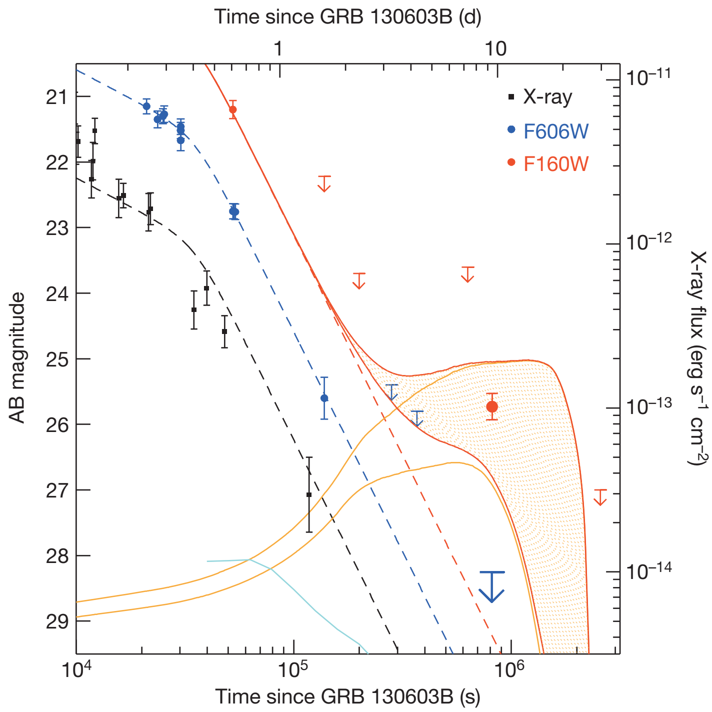

Figure 1.6: Light curve of GRB 130603B at X–ray (black), optical (blue) and near-infrared (red) wavelengths. The late-time excess at near-infrared wavelengths around ∼10 days post-burst relative to the power-law decay expected from afterglow emission only suggests the presence of an underlying kilonova. Reproduced from Tanvir et al. (2013).

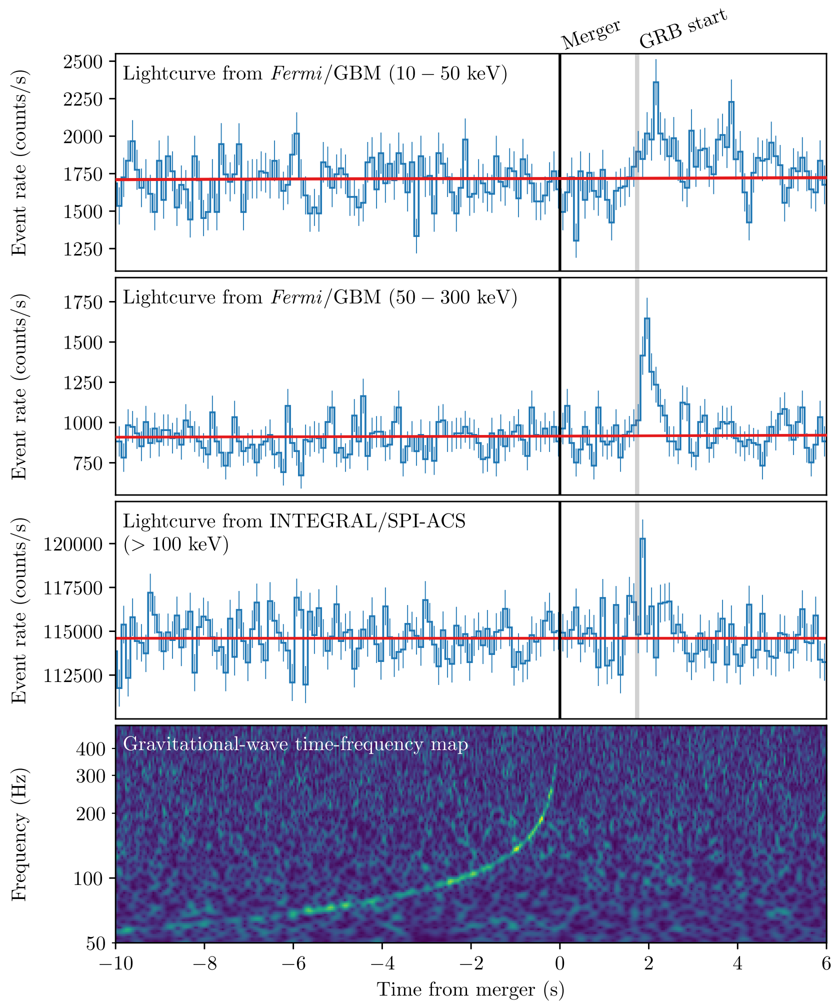

Figure 1.7: Joint detection of the GW170817/GRB 170817A multi-messenger event. The top three panels show the light curve of GRB 170817A as recorded by *Fermi* and *INTEGRAL*. The bottom panel shows the time-frequency plot of GW170817, comprising of data from both LIGO-Hanford and LIGO-Livingston. The reference time shown here is the time of the GW170817 trigger. This event provided the "smoking gun" confirmation that at least some fraction of short GRBs are produced in the aftermath of binary neutron star mergers. Reproduced from Abbott et al. (2017b).

(e.g., Abbott et al., 2017a), rich datasets to improve kilonova models (for a recent, comprehensive review, see Metzger, 2019), and much more.

1.2.3 Challenges to the Short/Long Dischotomy

While most GRBs follow this short and long dichotomy, there have been a few exceptions that challenge this classification system and are not yet fully understood.

Short GRBs with supernova signatures — supernova signatures were identified in the light curve of GRB 200826A, a short GRB with a duration of ∼1 s (Ahumada et al., 2021; Zhang et al., 2021; Rossi et al., 2022). This result suggested that at least some short GRBs form from collapsar channels, challenging the standard dichotomy of short and long GRBs. A possible idea that explains the short duration of the collapsar event was for the event to be on the brink of a successful and failed GRB, i.e. the central engine lasts *just* long enough for the jet to break out of the stellar envelope (see Bromberg et al., 2012, and references therein).

Long GRBs with kilonova signatures (and without supernova signatures) — on the other hand, kilonova signatures were identified in the light curve of long GRB 211211A, with a duration of ∼1 min (Rastinejad et al., 2022; Troja et al., 2022; Mei et al., 2022). This result suggested that at least some long GRBs form from compact merger channels, once again challenging the standard dichotomy of short and long GRBs. It also provides a plausible, retrospective explanation for a set of long GRBs (including a population of short GRBs with softer "extended emission") that were previously observed to stringent limits to not have any signatures of an accompanying supernova; for example, GRB 060614 (Gehrels et al., 2006; Fynbo et al., 2006). Possible progenitor channels that have been proposed to explain the extended emission of compact merger events include, for example, invoking relativistic winds from the spin-down of the protomagnetar (e.g., Metzger et al., 2008), tidal disruption of a neutron star in a black hole-neutron star merger event (e.g., Metzger et al., 2010; Desai et al., 2019), and compact binaries formed via dynamical interactions in dense environments (e.g., Levan et al., 2023).

Low-luminosity GRBs — a subset of long GRBs have a much lower luminosity than the wider population, for example, GRB 980425 as discussed in Subsection 1.2.1. It has been proposed that this subset of low-luminosity GRBs (gamma-ray luminosity $L_\gamma < 10^{49}\,\mathrm{erg\,s^{-1}}$) may come from a sub-population distinct from high-luminosity GRBs ($L_\gamma > 10^{49}\,\mathrm{erg\,s^{-1}}$), with a higher local rate and a significantly wider jet opening angle (Liang et al., 2007). One model explaining explaining low-luminosity GRBs invokes the presence of an extended stellar envelope (not present in the high-luminosity GRB scenario), which engulfs the jet (Nakar, 2015). As the jet deposits all its energy into the envelope, it leads to a mildly relativistic shock breakout, which in turns produces the low-luminosity GRB. Other studies (e.g., Salafia et al., 2016) have instead argued that low-luminosity and high-luminosity GRBs belong to the same population of bursts, suggesting that their differences are only due to viewing angle effects (with their different event rates being explained by selection effects). Recently, the confirmation of GRB 170817A — a low-luminosity *short* GRB — as a structured jet viewed off-axis (Mooley et al., 2018; Ghirlanda et al., 2019) suggests both the jet structure and viewing angle could explain the luminosity of any observed GRB event. However, the generalisation of this explanation to the wider sample of low-luminosity GRBs is still an open question: Beniamini & Nakar (2019) have found that the 11-hour X–ray luminosity to gamma-ray energy ratio in low-luminosity GRBs is comparable to that of the standard long GRB population, which should not be the case if low-luminosity GRBs were standard GRBs seen off-axis. A larger sample size of low-luminosity GRBs is still required to arrive at clearer conclusions about its origins.

Ultra-long GRBs — a subpopulation of GRBs with extremely long durations ($>$ 1 000 s) has been recently proposed, sparking a debate as to whether they represent the tail of the standard long GRB duration distribution (Virgili et al., 2013) or whether they represent a new sub-class of GRBs with fundamentally different properties (Boër et al., 2015). Evidence of properties for this subpopulation differing from standard long GRBs have started to emerge over the years. For example, supernova SN 2011kl, associated with ultra-long GRB 111209A, was found to be three times more luminous compared to type Ic supernovae associated with standard long GRBs, while also possessing a very distinct spectrum (Greiner et al., 2015). Radio observations of GRB 130925A revealed a sharp spectral cut off above 10 GHz, suggesting either a mono-energetic electron distribution or very steep electron spectral index ($p \approx 4$, where the electron power law energy distribution is defined as $dN/dE \propto E^{-p}$), which is inconsistent with previously observed properties for standard long GRBs and their radio afterglows (Horesh et al., 2015). To explain the long central engine activity required for ultra-long GRBs, it has been proposed that ultra-long GRB progenitors may involve the core-collapse of low-metallicity blue supergiants (Gendre et al., 2013), with much larger radii than the Wolf-Rayet progenitors of standard long GRBs, or the tidal disruption of compact stars by massive black holes (Levan et al., 2014).

1.3 Afterglow Physics in the Blast-wave Model

The similarity in the observed signatures of both short and long GRBs (albeit on different energy and time scales) motivated the search for a unifying physical model that could explain the observations from both classes of GRBs.

1.3.1 Relativistic Blast-wave Model

The properties of GRBs inferred from early observations under the assumption of an extragalactic origin led to the so called *compactness problem* (Ruderman, 1975): the high amount of energy released and short variability timescales should imply a high optical opacity from pair production leading to a thermal spectrum, but this was inconsistent with the non-thermal spectra observed in GRBs. One of the solutions proposed to address this problem was for the emitting region, or outflow, to expand relativistically with bulk Lorentz factors $\Gamma \gtrapprox 100$ (e.g., Goodman, 1986; Paczynski, 1986; Rees & Mészáros, 1992; Mészáros & Rees, 1997). In this standard “fireball” model explaining GRBs and afterglows, the relativistic outflow could be produced if a large amount of energy was deposited into a small region, provided the initial fireball has a relatively low baryon fraction. The energy reservoir for this is thought to be the accretion disks formed in the collapse of massive stars or compact binary coalescence as discussed in Section 1.2, with the energy being extracted from the disk via processes such as the Blandford-Znajek mechanism (Blandford & Znajek, 1977, this is just one of many proposed energy extraction mechanisms). In this scenario, the fireball can expand under its own pressure, increasing to relativistic speeds, and becomes matter-dominated (i.e., the radiation energy is mostly transferred to kinetic energy) by the time it becomes optically thin.

Under this model, the fireball ejecta produces both the “prompt” GRB emission as well as the afterglow. The collision of shells travelling at different speeds within the fireball produces *internal* shocks, which are thought to give rise to the prompt emission[4]. The afterglow is then produced by a pair of *external* shocks that arise when the shells of the fireball interact with and expands into the circumburst medium with a constant Lorentz factor. A *forward* shock forms at the interface of the ejecta and the circumburst medium, propagating in the direction towards the medium. After the ejecta has swept up a sufficient amount of the circumburst medium, a secondary *reverse* shock forms, propagating backwards in the direction of the ejecta. Once the reverse shock has crossed the ejecta, the ejecta enters its relativistic *blast wave* stage, where its dynamics can be described by the self-similar Blandford-McKee solution (Blandford & McKee, 1976) as it decelerates into the circumburst medium. At each of these stages, electrons are accelerated in the magnetic fields at the forward and reverse shock fronts (electron acceleration may occur in the reverse shock only while the reverse shock is crossing the ejecta), producing the synchrotron emission (and consequently the synchrotron self-Compton emission) that gives rise to a panchromatic afterglow[5].

1.3.2 Broadband Modelling of the Blast Wave

The synchrotron spectra predicted by analytical synchrotron external shock models generally consists of multiple power-law segments, separated by various break frequencies (e.g., Sari et al., 1998); this is consistent with afterglow observations (e.g., the initial spectrum of GRB 030329 as discussed in Subsection 1.2.1 and shown in Figure 1.5). A self-consistent model would need to include the effects of synchrotron self-Compton scattering, whereby the synchrotron photons scatter off the relativistic electrons that initially produced them (e.g., Sari et al., 1996). The predicted light curves and spectra of observed afterglow can then be used in broadband modelling via a set of *closure relations* to deduce the physical parameters of the relativistic blast wave and the circumburst environment. The Granot & Sari (2002) model, for example, is one such model that produces the synchrotron light curves and spectra based on the Blandford-McKee self-similar solution, describing the dynamics of a spherical relativistic blast wave with bulk Lorentz factor Γ (with modifications taking into account radiative effects as introduced by Sari, 1997 and Cohen et al., 1998). This model assumes a fixed fraction of the shock energy, $\epsilon_{\rm B}$, is in the magnetic field and a fixed fraction, $\epsilon_{\rm e}$, is in the accelerated electrons behind the shock[6]. These electrons are assumed to have a power-law distribution of energies, such that $N(\gamma) \propto \gamma^{-p}$ above a minimum Lorentz factor $\gamma \geq \gamma_{\rm min}$, where p is the electron spectral index. While the model assumes a spherical relativistic blast wave, it is also valid for jetted outflows at early times provided that the outflows are still highly

[4]This is just one of the energy dissipation mechanisms proposed to explain the prompt emission. The nature of the energy dissipation mechanism, the nature of the jet (whether it is Poynting flux or matter dominated), and the jet launching mechanisms are not very well understood, and are still topics of active investigation.

[5]Additional thermal and non-thermal components may also be produced from the dynamical ejecta in compact object coalescences. I do not discuss these components in detail here as the contents of this thesis primarily concerns emission pertaining to the external forward shock only.

[6]The fraction of electrons accelerated in the shock is another parameter of the model (Eichler & Waxman, 2005). However, in practice, it is not frequently used in fitting GRB data since it is difficult to constrain with current observations.

relativistic, such that $\Gamma \gg \theta_{\rm j}^{-1}$, where $\theta_{\rm j}$ is the *initial* jet opening angle (which can be determined from the jet break time, see Subsection 1.3.3).

The structure of the circumburst medium considered in the model is often parameterised by its circumburst density, $n(r) \propto r^{-k}$, where r is the distance from the explosion site and k is the power-law index of the density distribution. From this parameterisation, two standard scenarios ($k = 0$ and $k = 2$) are often studied: the first assumes a homogeneous interstellar medium (ISM) environment with constant density n_0 (i.e., $k = 0$), while the second assumes an environment structure shaped by pre-explosion stellar winds (see Chevalier & Li, 2000), such that the density falls off with the distance squared (i.e., $k = 2$), with $n(r) = Ar^{-2}$ (where A is a proportionality factor related to the mass-loss rate $\dot{M}_w$ and stellar wind velocity v_w of the progenitor star by $A = \dot{M}_w/4\pi v_w = 5 \times 10^{11} A_* \,{\rm g\,cm^{-1}}$). The break frequencies in the wind scenario — $\nu_{\rm sa}$ the self-absorption frequency below which synchrotron self absorption is significant, $\nu_{\rm m}$ the synchrotron peak frequency corresponding to the lowest electron energy in the power-law distribution with $\gamma = \gamma_{\rm min}$, and $\nu_{\rm c}$ the cooling frequency above which the synchrotron cooling time for the electrons is shorter than the hydrodynamic timescale of the source — relate to the properties of the relativistic blast wave as follows:

$$\nu_{\rm sa} = 8.31 \,\frac{(p-1)^{3/5}}{(3p+2)^{3/5}}\, 10^9\,(1+z)^{-2/5}\,\bar{\epsilon}_{\rm e}^{-1}\,\epsilon_{\rm B}^{1/5}\,A_*^{6/5}\,E_{\rm iso,kin,52}^{-2/5}\,t_{\rm days}^{-3/5}\,{\rm Hz}, \tag{1.1}$$

$$\nu_{\rm m} = 4.02\,(p-0.69)\,10^{15}\,(1+z)^{1/2}\,E_{\rm iso,kin,52}^{1/2}\,\bar{\epsilon}_{\rm e}^{2}\,\epsilon_{\rm B}^{1/2}\,t_{\rm days}^{-3/2}\,{\rm Hz}, \tag{1.2}$$

$$\nu_{\rm c} = 4.40\,(3.45-p)\,10^{10}\,e^{0.45p}\,(1+z)^{-3/2}\,\epsilon_{\rm B}^{-3/2}\,A_*^{-2}\,E_{\rm iso,kin,52}^{1/2}\,t_{\rm days}^{1/2}\,{\rm Hz}, \tag{1.3}$$

where $t_{\rm days}$ is the number of days elapsed since the burst event, $\bar{\epsilon}_{\rm e}$ is related to the fractional shock energy in the electrons by $\bar{\epsilon}_{\rm e} = \epsilon_{\rm e}(p-2)/(p-1)$, $E_{\rm iso,kin} = 10^{53} E_{\rm iso,kin,53}$ erg is the total isotropic equivalent kinetic energy of the blast wave, z is the redshift to the source, and e is the energy density of the electrons. A similar set of relations exist for the ISM scenario, but I do not list this here since most of the events discussed in this thesis fit the wind scenario more favourably than the ISM scenario (which may be expected for long GRB events given that the progenitors are likely related to Wolf-Rayet stars with high mass loss from stellar winds). The relations for the ISM scenario can be found in table 2 of Granot & Sari (2002).

The location of these frequencies assumes the blast wave is in the slow-cooling regime, with the break frequencies ordered as $\nu_{\rm sa} < \nu_{\rm m} < \nu_{\rm c}$, which is most commonly observed at radio frequencies. With typical values for the microphysical parameters of the blast wave, $\nu_{\rm sa}$ and $\nu_{\rm m}$ can often be traced in the radio frequencies, while $\nu_{\rm c}$ is often at higher energies in the X–ray to gamma-ray range. These break frequencies separate the synchrotron spectrum into multiple power-law segments; their temporal and spectral scalings in both the ISM and wind scenarios are summarised in Figure 1.8 and are related to the blast wave microphysical parameters in table 2 of Granot & Sari (2002). Therefore, by identifying (or constraining) the location of these break frequencies at any given point in time and by tracing the evolution of the spectra over time, we can infer the properties of the relativistic blast wave — e.g., the energy in the blast wave, power-law index of the electron energy distribution, fraction of the shock energy in the magnetic fields and electrons — and the

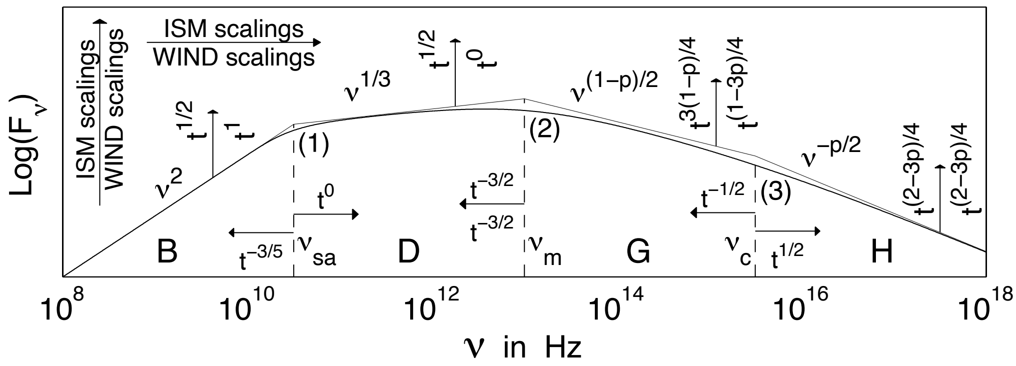

Figure 1.8: Model of the synchrotron spectrum from a spherical, relativistic blast wave expanding into an ISM and wind circumburst medium, in the slow-cooling regime with break frequencies ordered as $\nu_{\rm sa} < \nu_{\rm m} < \nu_{\rm c}$ (which is most commonly observed at radio frequencies). The arrows indicate the expected spectral and temporal scalings for each power-law spectral segment as well as the expected evolution of the break frequencies over time for both the ISM and wind scenario. Adapted from Granot & Sari (2002).

structure of the circumburst environment (which may reveal valuable information about the progenitor of the system).

At later times, modifications to the model need to be made when the assumption of a spherical relativistic blast wave no longer holds. As the blast wave slows down to $\Gamma \approx \theta_{\rm j}^{-1}$, the collimated nature of the jet needs to be factored into the model as (a) the region of the source outside the initial jet opening angle now becomes visible to the on-axis observer and (b) the jet starts to spread laterally, leading to a steepening of the light curve at all wavelengths (e.g., Sari et al., 1999). At even later times when the blast wave becomes non-relativistic, it can be treated as a quasi-spherical non-relativistic blast wave described by the self-similar Sedov-von Neumann-Taylor solution, leading to a general flattening in the light curve (e.g., Frail et al., 2000); in the later stage where the majority of the shock-accelerated electrons have become non-relativistic, the blast wave is said to have entered the *deep Newtonian* phase (e.g., Sironi & Giannios, 2013). Many further modifications to the models have also been implemented to explain the plethora of observed afterglow behaviours, such as invoking continuous energy injection into the blast wave (e.g., Dai & Lu, 1998; Rees & Mészáros, 1998) and joint modelling of reverse and forward shock components (e.g., van der Horst et al., 2014; Laskar et al., 2019). A comprehensive review of analytical synchrotron external shock models can be found in the work by Gao et al. (2013).

1.3.3 Collimated Jets in Gamma-ray Bursts

Since GRBs come from an extragalactic source population, the implied isotropic energy release in gamma-rays from these events was unreasonably large ($\sim 10^{53} - 10^{54}$ erg; e.g., Odewahn et al., 1998; Cenko et al., 2011) and could not be explained by the energy reservoirs available from their progenitors; a proposed solution was for the GRB outflows to be collimated as jets (Rhoads, 1999; Sari et al., 1999). This was confirmed with the detection of jet breaks in GRB afterglows (e.g., GRB

990510; Harrison et al., 1999), where the light curve steepens as the region of the source outside the initial jet opening angle becomes visible to the on-axis observer and the jet starts to spread laterally. Typically, a temporal steepening is identified as a jet break (as opposed to the passage of a characteristic frequency, for example) if the break is achromatic. The time at which the jet break occurs can then be used to estimate the opening angle of the jet θ_j (Sari et al., 1999). The geometry and the structure of the jet will affect the dynamics of the outflow, which in turn impacts the broadband modelling used for inferring the physical properties of these systems as previously discussed in Subsection 1.3.2, and also impact our understanding of the wider GRB population.

Assuming a uniform top-hat jet, the beaming fraction, i.e., ratio of bursts along our line-of-sights to all bursts, is given by $f_\mathrm{b} = 1 - \cos\theta_\mathrm{j}$ (Frail et al., 2001). The implications of jet collimation are twofold: (1) the true luminosity of the GRB corrected for collimation is smaller than the isotropic luminosity by a factor of f_b, and (2) the true event rate of GRBs is larger than the observed (on-axis) rate by a factor of f_b^{-1}. Studies have since estimated the typical jet opening angle for LGRBs to be $\theta_\mathrm{j} \sim 6°$ (Guetta et al., 2005; Goldstein et al., 2016; Ghirlanda & Salvaterra, 2022), corresponding to a distribution of true collimation-corrected gamma-ray luminosity clustered around $L_\gamma \sim 5 \times 10^{50}$ erg and a factor of $f_b^{-1} \sim 200$ more off-axis GRBs (or "orphan afterglows" without high-energy triggers) contributing to the total event rate. For short GRBs, the jet opening angle was estimated in a recent large-sample study by (Fong et al., 2015) to be $\theta_\mathrm{j} \sim 16°$, corresponding to $L_\gamma \sim 1.6 \times 10^{50}$ erg and $f_b^{-1} \sim 25$; however, I caution that the sample of short GRBs may be biased due to their significantly dimmer afterglows, leading to a jet opening angle measurement that is not representative of the wider population.

The preceding discussion mainly concerns a top-hat jet structure featuring a constant distribution of energy within the jet opening cone; specifically, the energy per unit of solid angle, $dE/d\Omega$, is constant within the jet opening cone. Recent afterglow observations, however, have demonstrated the need to account for jet *structure*, such that the distribution of kinetic energy across the jet outflow has an angular dependence (usually modelled as a power-law or Gaussian dependence), i.e. $dE/d\Omega(\theta, t)$, where θ is the angle from the jet axis[7]. While this idea has been explored for many years (e.g., Rossi et al., 2002), recently renewed interest came with the rich dataset accumulated for the multi-messenger event GW 170817/GRB 170817A, where the observations were only compatible with an off-axis structured jet interpretation (e.g., Mooley et al., 2018; Ghirlanda et al., 2019). Similarly, the observed cocoon signatures in the spectra of the GRB 171205A/SN 2017iuk event also pointed to the importance of considering jet structure in the long GRB scenario (Izzo et al., 2019). A schematic outlining the formation and early evolution of a structured jet in both the short and long GRB scenario is shown in Figure 1.9.

[7]An important distinction is the angular structure of the kinetic energy of the outflow and the angular structure of the gamma-ray energy released. The discussion here is related to the former. The latter is expected to fall more steeply as a function of angle from the jet axis than the former (as the energy density and Lorentz factors are much lower at high latitudes from the jet compared to the jet core).

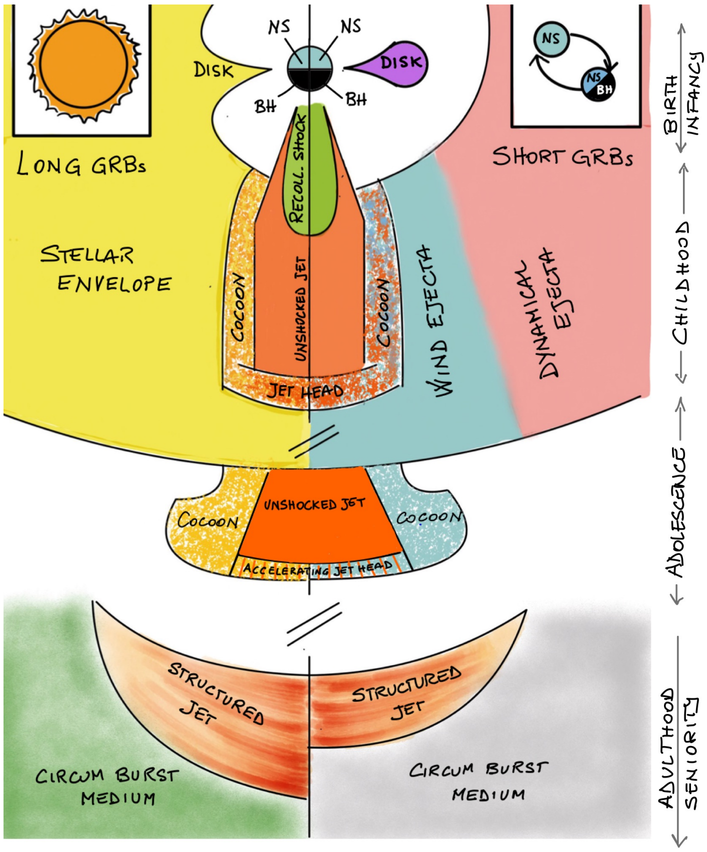

Figure 1.9: A schematic outlining the formation and early evolution of a structured jet in both the short and long GRB scenarios. See the relevant text in Subsection 1.3.3 for a description of the process. Reproduced from Salafia & Ghirlanda (2022).

As shown in this schematic, the energy injection from the initial GRB jet launching into the stellar layers (disk winds / merger ejecta) in the long (short) GRB scenario gives rise to a cocoon, which expands laterally to the jet itself. The jet is collimated by the inwards pressure from the cocoon, and provided the central engine lasts sufficiently long, will break out of the cocoon at relativistic speeds to produce the GRB and afterglow as discussed in Subsection 1.3.1. With the cocoon still expanding at mildly relativistic velocities as it breaks out from the progenitor photosphere, the mature jet and the emission components it produces can then be aptly described by a structured jet model. Please refer to Salafia & Ghirlanda (2022) for a recent review on jet structure.

1.4 A Multi-scale Radio Study of the Afterglow

Radio interferometry is a powerful technique that can be exploited on multiple angular scales to study the behaviour of afterglows at longer wavelengths, and by extension, the physical properties of the outflow. Considering the angular resolution of a telescope — $\theta_\mathrm{A} \propto \lambda/D$, where λ is the observing wavelength and D is the diameter of the aperture — a larger aperture is required to improve the resolving power at longer wavelengths. Instead of using one large dish to achieve a larger aperture, radio interferometry synthesises an array of smaller antennas separated by large distances to attain the required resolving power, i.e., D becomes the *baselines* separating the antennas rather than the size of a single dish. For a detailed historical overview and discussion of radio interferometry principles, refer to the standard texts Taylor et al. (1999) and Thompson et al. (2017). In this section, I summarise the basic concepts of radio interferometry and discuss its applications in standard observations, wide-field surveys and high-resolution imaging for studying the nature of GRBs and their afterglows.

1.4.1 Radio Interferometry and Aperture Synthesis

The electric field from a distribution of sources in the sky induces a complex voltage at each antenna of the radio interferometer. The radio interferometer can be treated as an ensemble of antenna pairs, where the voltages at each antenna pair can be correlated to obtain the *complex visibilities*, a quantity whose real components (amplitudes) are related to brightness of the sources in the sky and whose imaginary components (phases) are related to the position of the sources in the sky. These complex visibilities, V, can be represented in a special (u, v, w) coordinate system and related to the radio sky brightness distribution, $I(l, m)$, for Fourier synthesis imaging as follows:

$$V(u, v, w) = \int \int I(l, m)\, e^{-2\pi i[ul+vm+w(\sqrt{1-l^2-m^2}-1)]} \frac{dl\, dm}{\sqrt{1 - l^2 - m^2}}. \tag{1.4}$$

In this coordinate system, the w-axis is in the reference of interest or the *phase tracking centre* (often the direction of the target source), while the u- and v-axes represent the directions East and North, respectively, in the plane orthogonal to w-axis. The baseline vector separating each antenna pair can be projected onto these axes, giving u, v and w components expressed in units of wavelength at the central frequency. At any given point in time, an antenna pair (or baseline) will sample two unique points in the (u, v, w) parameter space, but as the Earth rotates, the projection of the baseline on the u-, v- and w-axes changes, allowing for more points to be sampled. Correspondingly, a given position in the sky can be expressed using the unit vector whose components are $(l, m, n = \sqrt{1 - l^2 - m^2})$, which are the direction cosines of u, v and w, respectively.

In two special cases — (1) when the baselines are coplanar, e.g., in a East-West array like the Australia Telescope Compact Array (ATCA); or (2) where l and m are small, e.g., in narrow-field imaging where the source of interest is located at the phase tracking centre — Equation 1.4 can be reduced to:

$$V(u, v) = \int \int I(l, m)\, e^{-2\pi i(ul+vm)}\, dl\, dm, \tag{1.5}$$

which is a two dimensional Fourier transform[8]. In principle, this allows us to invert

[8] For two dimensional arrays, for example, ASKAP and VLA, and large values of l and m (wide-field scenario), the assumptions for reducing the visibility equation to a two dimensional Fourier transform in Equation 1.5 breaks down. In this case, a more careful treatment of the w term is required; various standard techniques and algorithms solve this problem (see, for example, Lecture 14 of Taylor et al., 1999).

the visibilities to obtain the radio sky brightness distribution, $I(l, m)$, or the *true* image. However, due to a finite number of baselines in a given synthesis array, it is impossible to sample the entire (u, v)-plane, so the inverted visibilities yield instead the *dirty* image. The *sampling function* is defined by the points in the (u, v)-plane that have been sampled (1 where it is sampled, 0 elsewhere): sampling points at regions further out in the (u, v)-space corresponds to higher sensitivity to structure on smaller angular scales, and vice versa. The aforementioned dirty image is the convolution of the true image with the *dirty beam*, which is the inverse Fourier transform of the sampling function. Therefore, deconvolution algorithms, such as CLEAN (Högbom, 1974; Clark, 1980), need to be applied as an intermediate step after the inversion of the visibilities to obtain the true image, from which we can examine source structure and flux densities.

In practice, the observed visibilities from the radio telescope need to be calibrated to obtain the true visibilities before inversion; this is to correct for errors relating to, but not limited to, the instrumental bandpass, flux-density scale, and complex gains (e.g., from atmospheric phase variations). In addition to this, the recovered image after deconvolution requires an extra correction accounting for the primary beam attenuation — i.e., the direction-dependent sensitivity of the interferometer to incoming radio waves — before we can arrive at the true image. The basic techniques of radio interferometry I have outlined above provide the foundation for us to study GRB afterglows at radio frequencies across multiple different angular scales.

1.4.2 Radio Monitoring of Afterglows

Standard targeted radio observations of GRBs with angular resolution (synthesised beam size) on the order of arcseconds can contribute to monitoring the evolution of the afterglow from the early-time, when the reverse shock component is dominant, to late-time, when the blast wave is expected to have entered the deep Newtonian regime. Large sample studies have shown the detection rate of radio emission from GRB events to be $\sim$30% (Chandra & Frail, 2012), but can be up to 56% with a rapid-response strategy that follows the GRB on timescales of hours to days post-burst (Anderson et al., 2018).

These standard radio observations provide vital information about GRB properties: (i) accurate calorimetry of a GRB event can be performed when the ejecta has transitioned into the Newtonian, non-relativistic regime (i.e., when the ejecta has become quasi-spherical), allowing for the energetics of the blast wave to be measured without assumptions on the jet geometry and structure (Frail et al., 2005), which may in turn help constrain the possibility that a neutron star remnant was left behind after the explosion (e.g., Ricci et al., 2021); (ii) "dark GRBs" may be obscured by dust at optical wavelengths, but not at radio frequencies (e.g., Djorgovski et al., 2001); (iii) scintillation patterns observed in early radio observations as shown in Figure 1.3 (*panel b.*) can provide source size constraints that contribute to revealing the underlying microphysics of the burst (Frail et al., 1997); (iv) the evolution of the self-absorption and synchrotron peak frequencies through the radio bands are necessary for complete broadband modelling of a GRB as discussed in Subsection

1.3.2 and also for independent studies of specific microphysical parameters (e.g., Beniamini & van der Horst, 2017); (v) as discussed in Subsection 1.3.3, the radio light curve could also provide important signatures to constrain the jet break, important for understanding the geometry and structure of the GRB event, especially if the emission at shorter wavelengths is no longer detectable at the jet break time.

1.4.3 Afterglow Studies in the Wide-field Survey Era

Multi-epoch wide-field radio surveys covering a significant fraction of the sky with regular cadence are now sensitive enough to contribute to the study of the GRB population. The ASKAP telescope (Hotan et al., 2021), for example, conducts many of these wide-field radio surveys that span multiple epochs, including the Rapid ASKAP Continuum Survey (RACS; McConnell et al., 2020) and the ASKAP survey for Variables and Slow Transients (VAST; Murphy et al., 2013). ASKAP uses phased array feed technology[9] to attain the sensitivity and speed required to carry out these surveys efficiently. In 1 min of integration time, the telescope is capable of reaching an rms of $\sim$1 mJy beam^{-1} across a $\sim$30 square degree nominal field-of-view. Joining these ASKAP surveys are the MeerKAT ThunderKAT program (Woudt et al., 2018), a commensal survey for radio transients, and the VLA Sky Survey (VLASS; Lacy et al., 2020), a multi-epoch radio survey covering the entire radio sky above a Declination of $-40°$, all of which serve as pathfinders to more potent Square Kilometre Array (SKA; Dewdney et al., 2009) surveys for the study of GRB radio afterglows (and transients in general).

Wide-field radio surveys complement standard radio observations in the study of GRBs by contributing the following: (i) they are able to find orphan afterglows, particularly from GRBs beamed far off-axis from the observer, that do not have observable signatures at shorter wavelengths (e.g., Levinson et al., 2002; Ghirlanda et al., 2014; Law et al., 2018); (ii) they provide an untargeted follow-up of *every* GRB in the field-of-view, which is effective in discovering unexpected radio emission, such as from late-time supernova-powered rebrightening events (e.g., Barniol Duran & Giannios, 2015) or kilonova afterglows (e.g., Nakar & Piran, 2011); (iii) they can help localise events with a poor localisation, such as for those expected from gravitational wave events (e.g., Dobie et al., 2019); and (iv) they can help constrain the fraction of GRB systems that may lead to the formation of a superamassive neutron star (e.g., Beniamini & Lu, 2021).

1.4.4 High-resolution VLBI Imaging of Afterglows

VLBI can contribute valuable information in the study of GRBs by providing high-resolution images of the source, which may reveal information about the source structure and motion. In VLBI observations, elements of the array can be separated by distances up to thousands of kilometres (even larger in global or space VLBI experiments), corresponding to large projected baselines in (u, v)-space, which allows

[9] The phased array feed used in the ASKAP telescope is made up of 188 individual receivers, or "elements", which are capable of being digitally weighted to form up to 36 beams, covering a nominal field-of-view of $\sim$30 square degrees.

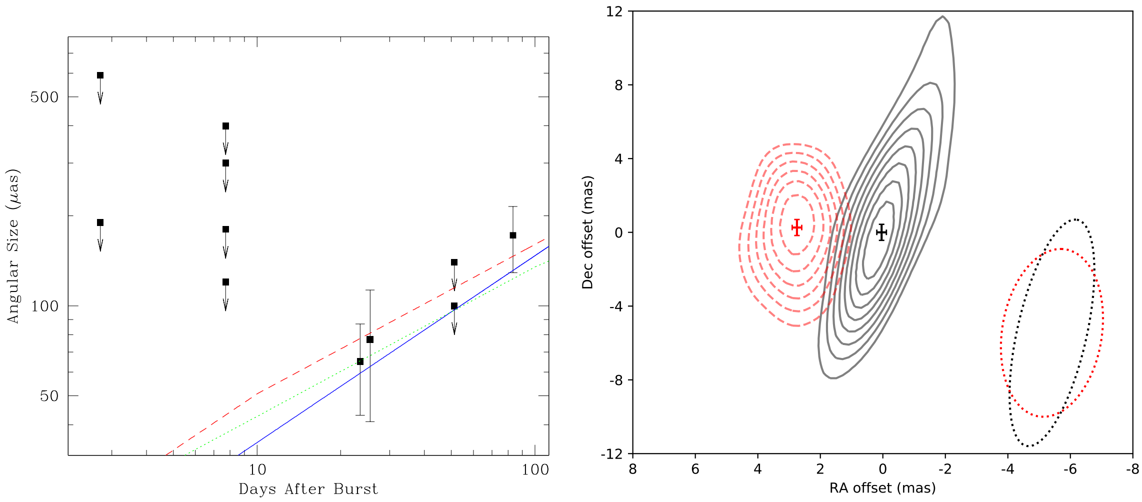

(a) GRB 030329 **(b)** GW170817/GRB 170817A

Figure 1.10: *Panel (a)* — the angular size measurements and limits for the radio afterglow of GRB 030329 using VLBI provided evidence for relativistic source expansion. The different lines represent expectations from 3 different models for the outflow (all of which assuming a constant density circumburst medium): a spherical fireball (blue solid line), a jet model with an early jet break $t_j = 0.5\,\mathrm{d}$ (green dotted line) and a jet model with a late jet break $t_j = 10\,\mathrm{d}$ (red dashed line). Reproduced from Taylor et al. (2004). *Panel (b)* — VLBI observations of the GRB 170817A afterglow taken 75 (black solid lines) and 230 (red dashed lines) days post-burst. The measured $2.7 \pm 0.3\,\mathrm{mas}$ proper motion supported the interpretation of the event as a structured jet viewed off-axis. Reproduced from Mooley et al. (2018).

the array to reveal small scale structure on the order of milliarcseconds. In the past, VLBI observations of GRB 030329 have allowed astronomers to measure the source expansion of the event, providing the first direct evidence confirming the relativistic nature of GRB outflows (Figure 1.10, *panel a.*; Taylor et al., 2004). The ability to measure the source size, and in particular the expansion (i.e., the size in two or more epochs), provide extra constraints on the microphysical parameters of the relativistic blast wave, complementary to the constraints obtained in multi-wavelength broadband modelling discussed in Subsection 1.3.2; for example, the source size, $R_{\perp,\mathrm{wind}}$, in the wind scenario is related to the microphysical blast wave parameters governing the energetics and circumburst medium density by (Galama et al., 2003; Taylor et al., 2004):

$$R_{\perp,\mathrm{wind}} = 2.4 \times 10^{16} \left(\frac{E_{52}}{A_*}\right)^{1/4} \left(\frac{t_{\mathrm{days}}}{1+z}\right)^{3/4} \mathrm{cm}. \tag{1.6}$$

More recently, VLBI was critical in revealing the superluminal motion of the radio emitting region for the afterglow of GRB 170817A, confirming the interpretation of the event as a structured jet viewed off-axis (Figure 1.10, *panel b.*; Mooley et al., 2018; Ghirlanda et al., 2019). This measurement was able to place stringent constraints on the viewing angle, which in turn contributed to reducing the uncertainty on Hubble parameter measurements using the redshift and distance information of this multi-messenger event (e.g., Hotokezaka et al., 2019). Beyond these applications, it has been proposed that VLBI can provide yet another measurement of the

Hubble parameter through time-delay cosmography applied to lensed GRB events (Refsdal, 1964). In such a scenario, the time delay between the lensed GRB images is dependent on the mass distribution of the lens, which can be modelled from the morphology and distribution of detected components in high-resolution VLBI images, as well as geometric effects from different paths in space-time, which is determined by the Hubble parameter.

1.5 Thesis Overview

Our understanding of GRBs and their afterglows can benefit from radio interferometric techniques applied across various different angular scales, ranging from wide-field sky surveys down to narrow-field high-resolution VLBI observations. The next generation of radio telescopes, such as the SKA and the Next Generation Very Large Array (ngVLA; Murphy et al., 2018), promise orders of magnitude improvement in both sensitivity and survey speed. Some of these improvements have already made their way into the current generation of radio telescopes, including SKA precursors like ASKAP and MeerKAT (Jonas & MeerKAT Team, 2016; Camilo et al., 2018). These improvements will advance modern radio interferometry on all angular scales, but will also come with its own set of challenges.

In this thesis, I will highlight some of the key opportunities and challenges that these advances will bring for answering important open questions about GRBs and their afterglows, revealed primarily by data taken using (but not limited to) the ASKAP telescope. I provide an overview of the thesis below.

In Chapter 2, I answer the question: *are the current generation of radio surveys sensitive enough to contribute to the study of GRBs and their afterglows?* I describe a targeted search I conducted for all long GRB afterglows located within the RACS footprint. I present the resulting detection of late-time radio emission from the low-luminosity GRB 171205A, the first confirmed detection of a radio afterglow in a wide-field radio survey. With the knowledge that the GRB was still radio bright more than 2 years post-burst, I show how new multi-frequency radio monitoring observations of the source at late-times helped to reveal the microphysical parameters of the GRB and the nature of the circumburst environment in which the GRB exploded in.

In Chapter 3, I answer the question: *what constraints on the beaming fraction and jet opening angle can we achieve with multi-epoch variability surveys today?* I showcase a novel matched-filter approach to finding orphan afterglows in the multi-epoch VAST Pilot Survey (Murphy et al., 2021). I describe the five candidates I had recovered from my search using this matched-filter approach, including one synchrotron transient candidate that was interpreted as either a likely off-axis GRB or tidal disruption event (TDE), as well as the implications of these results on the GRB beaming fraction and on future radio transient search strategies.

In Chapter 4, I answer the question: *can we use lensed GRB events for estimating the Hubble parameter (via time-delay cosmography) or for probing the existence of intermediate mass black holes?* I describe my joint radio monitoring and VLBI program that aims to confirm lensed GRB events, infer the properties of the lens, and estimate the Hubble parameter using time-delay cosmography (Refsdal, 1964). In particular, I outline the results from my program's first observing campaign conducted for GRB 220627A, which was initially proposed to be either a lensed GRB candidate or an ultra-long GRB (Roberts et al., 2022). A radio afterglow was detected in the observing campaign, but the VLBI confirmation of the lensed event was inconclusive, partly due to insufficient sensitivity. I discuss the unusual properties of the radio afterglow, the implications of our outcomes on the observing strategy for future events, and the opportunities that the next generation of radio telescopes could bring for this science.

Finally, I conclude this thesis in Chapter 5. I summarise the body of work in this thesis and describe avenues of future research that has been enabled by the work in this thesis. I also outline the broader scientific implications of this thesis for future studies of GRBs (and other transients) at radio frequencies in the SKA era.

Chapter 2

A search for radio afterglows from gamma-ray bursts with the Australian Square Kilometre Array Pathfinder

James K. Leung,[1,2,3] Tara Murphy,[1,3] Giancarlo Ghirlanda,[4] David L. Kaplan,[5] Emil Lenc,[2] Dougal Dobie,[1,2,3,6] Julie Banfield,[2] Catherine Hale,[7] Aidan Hotan,[7] David McConnell,[2] Vanessa A. Moss,[2,1] Joshua Pritchard,[1,2,3] Wasim Raja,[2] Adam J. Stewart,[1] and Matthew Whiting[2]

[1]Sydney Institute for Astronomy, School of Physics, The University of Sydney, NSW 2006, Australia
[2]CSIRO Astronomy and Space Science, PO Box 76, Epping, NSW 1710, Australia
[3]ARC Centre of Excellence for Gravitational Wave Discovery (OzGrav), Hawthorn, VIC 3122, Australia
[4]INAF – Osservatorio Astronomico di Brera, via E. Bianchi 46, I–23807 Merate, Italy
[5]Department of Physics, University of Wisconsin-Milwaukee, P.O. Box 413, Milwaukee, WI 53201, USA
[6]Centre for Astrophysics and Supercomputing, Swinburne University of Technology, Hawthorn, VIC 3122, Australia
[7]CSIRO Astronomy and Space Science, PO Box 1130, Bentley, WA 6102, Australia

This chapter is reproduced from Leung et al. (2021a), published in Monthly Notices of the Royal Astronomical Society as "A search for radio afterglows from gamma-ray bursts with the Australian Square Kilometre Array Pathfinder". The observations, reduction and the processing of the RACS data (described in Subsection 2.2.1) was done by the RACS team, of which I am a part of. The observations, reduction and the processing of the ATCA data taken on 2017 December 12, 2018 January 10 and 2018 February 19 (described in Subsection 2.6.3) was done by Dougal Dobie. The analysis of the X-ray data from Swift/XRT (described in Subsection 2.6.4) was done by Giancarlo Ghirlanda. All other work in this chapter was done by myself.

Abstract

We present a search for radio afterglows from long gamma-ray bursts using the Australian Square Kilometre Array Pathfinder (ASKAP). Our search used the Rapid ASKAP Continuum Survey, covering the entire celestial sphere south of declination $+41^{\circ}$, and three epochs of the Variables and Slow Transients Pilot Survey (Phase 1), covering $\sim 5,000$ square degrees per epoch. The observations we used from these surveys spanned a nine-month period from 2019 April 21 to 2020 January 11. We crossmatched radio sources found in these surveys with 779 well-localised (to $\leq 15''$) long gamma-ray bursts occurring after 2004 and determined whether the associations were more likely afterglow- or host-related through the analysis of optical images. In our search, we detected one radio afterglow candidate associated with GRB 171205A, a local low-luminosity gamma-ray burst with a supernova counterpart SN 2017iuk, in an ASKAP observation 511 days post-burst. We confirmed this detection with further observations of the radio afterglow using the Australia Telescope Compact Array at 859 and 884 days post-burst. Combining this data with archival data from early-time radio observations, we showed the evolution of the radio spectral energy distribution alone could reveal clear signatures of a wind-like circumburst medium for the burst. Finally, we derived semi-analytical estimates for the microphysical shock parameters of the burst: electron power-law index $p = 2.84$, normalised wind-density parameter $A_* = 3$, fractional energy in electrons $\epsilon_e = 0.3$, and fractional energy in magnetic fields $\epsilon_B = 0.0002$.

2.1 Introduction

Long gamma-ray bursts (lGRBs) are produced by ultra-relativistic, narrowly collimated jets, originating from the core collapse of massive stars (Woosley, 1993; MacFadyen & Woosley, 1999). Previous observations of core-collapse supernovae accompanying lGRBs have provided substantial evidence supporting this progenitor model; for example, GRB 980425/SN 1998bw (Galama et al., 1998) and GRB 030329/SN 2003dh (Stanek et al., 2003). In the standard fireball model, Fermi acceleration of electrons in the shock front resulting from jet interaction with the circumburst medium produces an afterglow visible across the entire electromagnetic spectrum (Sari et al., 1998). In many cases, radio afterglow emission is detectable at late-time on the order of months to years post-burst, even when the jet has decelerated into the non-relativistic regime and its expansion has become quasi-spherical (Frail et al. 2000; Chandra & Frail 2012, hereafter CF12).

The study of radio afterglows helps to constrain the microphysics and energetics (calorimetry) of burst events (Frail et al., 2000; van der Horst et al., 2008; Granot & van der Horst, 2014) and enables the reverse shock to be studied with greater observational latency compared with shorter wavelengths; for example, unlike the optical flash that occurs on the timescale of tens of seconds post-burst (Akerlof et al., 1999; Sari & Piran, 1999), the radio emission from the reverse shock persists for a few hours to a few days post-burst (Kulkarni et al., 1999; Anderson et al., 2018). Radio afterglows observed with diffractive scintillation (Goodman, 1997; Waxman et al., 1998) or Very Long Baseline Interferometry (VLBI; Granot et al., 1999; Taylor et al., 2004) techniques also provide measurements of the source size and jet expansion of burst events. However, due to the limited availability of observing time, follow-up observations for radio afterglows have been biased towards known bursts that meet a specific set of selection criteria: for example, bursts with strong X–ray, optical (CF12; Ghirlanda et al., 2013) or gravitational wave counterparts (Nakar & Piran, 2011; Hallinan et al., 2017); suspected dark bursts with optical counterparts obscured by dust that could still be detectable at radio wavelengths (Djorgovski et al., 2001); ultra-long GRBs with prompt emission lasting $\geq 1,000$ seconds (Levan et al., 2014; Horesh et al., 2015); and bursts at high redshifts that could probe Population-III stars (Toma et al., 2011; Burlon et al., 2016).

Unbiased radio transient surveys enable us to probe all events in the survey footprints for unusual or unexpected afterglow emission, which may otherwise be missed if not prioritised in traditional follow-up campaigns. For instance, using surveys to follow-up events could further our understanding of radio-quiet and -loud GRBs (Hancock et al., 2013; Lloyd-Ronning & Fryer, 2017; Lloyd-Ronning et al., 2019) as well as test for hypothesised GRB/supernova (GRB/SN) afterglow rebrightening effects, which are expected to occur on the order of decades post-burst when the supernova ejecta enters the Sedov-Taylor phase (Barniol Duran & Giannios, 2015; Peters et al., 2019). They could also enable us to monitor the late-time behaviour of well studied bursts with greater cadence, allowing for their burst parameters to be constrained independent of the burst geometry as the fireball transitions into the non-relativistic regime (e.g. Frail et al., 2000). Unlike studies using unbiased radio transient surveys for orphan afterglow searches, for example, Levinson et al. (2002) and Ghirlanda et al. (2014), we limited our use of such surveys to the follow-up of on-axis bursts with a high-energy trigger.

The Australian Square Kilometre Array Pathfinder (ASKAP; Hotan et al. *in press*) radio telescope operates at observing frequencies ranging from 700 to 1,800 MHz. It has a ∼30 square degrees field of view and is capable of reaching ∼1 mJy beam^{-1} RMS in 1 min of integration time. These capabilities facilitate observations for multi-epoch unbiased radio surveys, including the Rapid ASKAP Continuum Survey (RACS; McConnell et al., 2020) and the first phase of the pilot program for an ASKAP survey for Variables and Slow Transients (VAST; Murphy et al., 2013). We conducted a search for lGRB radio afterglows using RACS and three epochs of the VAST Pilot Survey (Phase 1; VAST-P1), with observations spanning a nine-month period from 2019 April 21 to 2020 January 11.

The structure of our paper is as follows. We outline the observations and data quality for RACS and each epoch of VAST-P1 used in our search in Section 2.2. In Section 2.3, we outline the expected detection rates of radio afterglows in our search. In Section 2.4, we explore the impact of host galaxy contamination on the detectability of radio afterglows in our search (and more generally, in a search for explosive transients). In Section 2.5, we describe our search methodology and how we distinguished host galaxy emission from afterglow emission. In Section 2.6, we describe our detection and follow-up of GRB 171205A, an interesting source we identified in Section 2.5. In Section 2.7, we discuss the physical interpretation of our GRB 171205A radio observations, the consideration of alternative search strategies, and the expected GRB yields for comparison surveys (both current and future). Finally, we summarise the conclusions from our radio afterglow search in Section 2.8.

We adopt a flat Λ-CDM cosmology with $H_0 = 67.8\,\mathrm{km\,s^{-1}\,Mpc^{-1}}$, $\Omega_\mathrm{M} = 0.308$ and $\Omega_\Lambda = 0.692$ throughout this paper (Planck Collaboration et al., 2016).

2.2 Observations and Data Analysis

The observations and quality metrics associated with the two ASKAP surveys used in our search are described in this section. Observations in both surveys were conducted at a central frequency of 887.5 MHz with a bandwidth of 288 MHz and a typical angular resolution of ∼15″.

2.2.1 Rapid ASKAP Continuum Survey

RACS is a large-area survey consisting of 903 tiles covering the entire radio sky south of declination +41°. Each tile had an integration time of ∼15 min and the resulting images had a median RMS noise of ∼0.29 mJy beam^{-1}. The RACS observations used for our search were conducted between 2019 April 21 and 2019 November 22. The full set of RACS observations include some tiles that were reobserved, with the

Table 2.1: Epochs from the ASKAP surveys, RACS and VAST-P1, were used in our GRB radio afterglow search. Columns 1 through 8 show the epoch number, radio survey used for each epoch, start date of each epoch, solid angle and number of tiles covered by each epoch, median RMS noise of observations in each epoch, median right ascension offset from ICRF2 source positions for observations in each epoch, median declination offset from ICRF2 source positions for observations in each epoch, and the flux-density ratio of sources in each epoch compared against sources in SUMSS. Observations for all epochs were conducted at the central frequency of 887.5 MHz with a bandwidth of 288 MHz and an angular resolution of $\sim 15''$.

Epoch #	Survey	Start Date (UT)	Sky Coverage	RMS (mJy beam^{-1})	RA Offset (arcsec)	Dec Offset (arcsec)	$S_{\mathrm{ASKAP}}/S_{\mathrm{SUMSS}}$
0	RACS	2019 Apr 21	$-90^\circ \leq \delta < +41^\circ$, 903 tiles	0.29	-0.6 ± 0.8	$+0.2 \pm 0.8$	1.03 ± 0.29
1	VAST-P1	2019 Aug 27	$\sim$4,980 sq. deg, 113 tiles	0.29	-0.1 ± 0.6	$+0.5 \pm 0.9$	1.01 ± 0.25
2	VAST-P1	2019 Oct 28	$\sim$4,760 sq. deg, 108 tiles	0.28	$+0.2 \pm 0.6$	$+0.2 \pm 1.0$	1.05 ± 0.30
8	VAST-P1	2020 Jan 11	$\sim$4,940 sq. deg, 112 tiles	0.26	-0.4 ± 0.6	$+1.0 \pm 1.2$	1.06 ± 0.19

Note – Epoch 8 is the third full epoch of the VAST-P1 survey. Several partial epochs between Epoch 2 and 8 were observed, but not used in our search. See O'Brien et al. (*in prep.*) for more details.

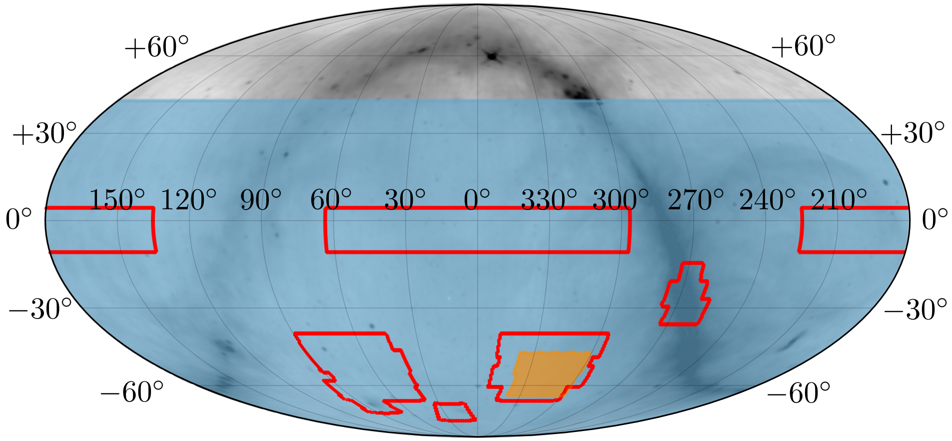

Figure 2.1: The VAST-P1 footprint is outlined in red and consists of 113 tiles. The RACS footprint shaded in blue extends between $-90^\circ \leq \delta < +41^\circ$. The EMU Pilot Survey shaded in orange consists of 10 tiles overlapping with the VAST-P1 and RACS surveys. The sky map is plotted with J2000 equatorial coordinates in the Mollweide projection and the background diffuse Galactic emission at 887.5 MHz (gray) is modelled from Zheng et al. (2017).

final observations occurring on 2020 June 21. These subsequent observations were not used in our search, but were used in a candidate radio afterglow follow-up discussed in Section 2.6. In this paper, RACSe1 refers to the initial observation of a tile and RACSe2 refers to any subsequent observation of the same tile.

We used a pre-release version of the RACS data for our radio afterglow search. As a result, this version of the RACS data did not implement some of the improvements to the data quality featured in the published data products. These improvements included, for example, holography corrections for the direction dependent flux-density scale and techniques to account for variations of the point-spread-function (PSF) size and shape across the ASKAP field of view. A more detailed discussion of these issues and their corresponding improvements are found in McConnell et al. (2020) and Hale et al. (*in prep.*). Please refer to these two papers for comprehensive details on the survey design, calibration process, data reduction strategy as well as the data products associated with the published images and source catalogues.

We performed an independent quality control check on the astrometric accuracy and flux-density scale to the aforementioned papers since the version of the data used for our search differs from the published data products. For our quality control analysis specifically, we used the Selavy (Whiting & Humphreys, 2012) source finder with default settings to extract sources from the RACS images and filtered for sources that were (a) isolated ($\geq 150''$ from nearest neighbour), (b) with non-extended PSF (major axis length $\leq 50''$ with a major-to-minor axis ratio ≤ 2), and (c) had a signal-to-noise ratio ≥ 10. The reason we chose a non-extended PSF criterion over a conventional point-source criterion (e.g. peak-to-integrated flux-density ratio) was due to aforementioned PSF variations affecting measurements of the integrated flux-density. This set of criteria ensured only isolated sources with reasonably compact PSFs and high signal-to-noise were used for the quality control analysis in this section; we did not apply these criteria to filter sources for our radio afterglow searches in subsequent sections of this paper.

Using this subset of sources, we determined the astrometric offset of RACS sources from the position of sources from the second realisation of the International Celestial Reference Frame (ICRF2; Fey et al., 2015); the offset is $-0\rlap{.}''6 \pm 0\rlap{.}''8$ in right ascension and $+0\rlap{.}''2 \pm 0\rlap{.}''8$ in declination. We calibrated the flux-density scale using the same subset of sources against the Sydney University Molonglo Sky Survey (SUMSS; Mauch et al., 2003), which was conducted at a comparable observing frequency of 843 MHz. This yielded a median flux-density ratio of $S_{\rm RACS}/S_{\rm SUMSS} = 1.03 \pm 0.29$, assuming a spectral index α of -0.8 (Condon, 1992), defined as $S_\nu \propto \nu^\alpha$. We have thus independently verified the reliability of the astrometry and flux-density scale for our early data products used in our scientific analysis.

2.2.2 VAST Pilot Survey (Phase 1)

Table 2.1 summarises the datasets from the three VAST-P1 epochs used in our search. VAST-P1 covers 113 tiles using the same tiling footprint as RACS; see Figure 2.1 for the sky coverage of both surveys. The integration time per tile per epoch was $\sim$12 min and the resulting images for each epoch had a median RMS noise varying from 0.26 to 0.29 mJy beam^{-1}. Some epochs have a few (≤ 5) tiles missing due to various issues (e.g. solar interference, observation failures, etc.) discussed in O'Brien et al. (*in prep.*). All observations were processed using standard procedures in the ASKAPsoft package (Cornwell et al., 2011; Guzman et al., 2019) and sources were extracted with the Selavy (Whiting & Humphreys, 2012) source finder. The full details of the observing strategy as well as the calibration, reduction and source extraction procedures are described in O'Brien et al. (*in prep.*).

Similar to before, we used a pre-release version of the VAST-P1 data, and hence, performed an independent quality control check. Applying the same procedure from the RACS quality control analysis, we found the astrometry of each VAST-P1 epoch to be typically accurate to $< 1''$ in both right ascension and declination, while the flux-density scale was typically calibrated to within 6 per cent from that of SUMSS with a RMS scatter $\leq$ 30 per cent. The astrometric accuracy and flux-density scale for each epoch are listed in Table 2.1. We have thus demonstrated that the data quality for VAST-P1 early data products was comparable to the RACS early data products; both were sufficient for the analysis described in subsequent sections, involving analyses of positional offsets and source variability.

2.3 Expected Afterglow Detection Rate

We constrained the expected afterglow detection rate for on-axis afterglows in our search using archival data of previous observations. In this work, we only consider the lGRB afterglow detections as short gamma-ray burst (sGRB) afterglow detections require flux-density sensitivities well below the thresholds of the surveys we use in this work (e.g. Fong et al., 2015). To determine the expected lGRB afterglow detection rate, we used the CF12 catalogue, consisting of 304 on-axis lGRB afterglows observed by radio telescopes over a 14 year span from 1997 to 2011. Radio emission was detected from 95 of these lGRBs, and of these, only 64 had known redshifts and fitted maximum flux-density measurements. In this paper, 'maximum flux density' refers to the flux density of a radio afterglow at the light-curve peak for the observing frequency of interest. Some other papers in the literature (e.g. CF12) refer to this as the 'peak flux density,' but we choose to use different terminology in our paper to avoid any confusion with standard radio astronomy terminology.

Figure 2.2 shows the scaled maximum flux densities against redshift and luminosity distance for radio-detected afterglows from the sample as well as the 5σ flux-density threshold for various surveys considered in this work. Note that while the threshold of the Evolutionary Map of the Universe (EMU; Norris et al., 2011) Pilot Survey is lower than the RACS/VAST-P1 threshold, it was unsuitable for our search due to the limited sky coverage (see Figure 2.1). We scaled the fitted maximum flux density of the lowest frequency observation for each GRB in CF12 to 887.5 MHz, which is the central frequency of RACS and VAST-P1 observations. Two different spectral indices were applied for the scaling, $\alpha = 1/3$ and $\alpha = 2$, corresponding to different scenarios for the self-absorption frequency, $\nu_{\rm sa}$. In both these scenarios, we considered the typical afterglow spectrum in the slow cooling regime as described in Granot & Sari (2002, hereafter GS02). In the $\alpha = 1/3$ scenario, our observing

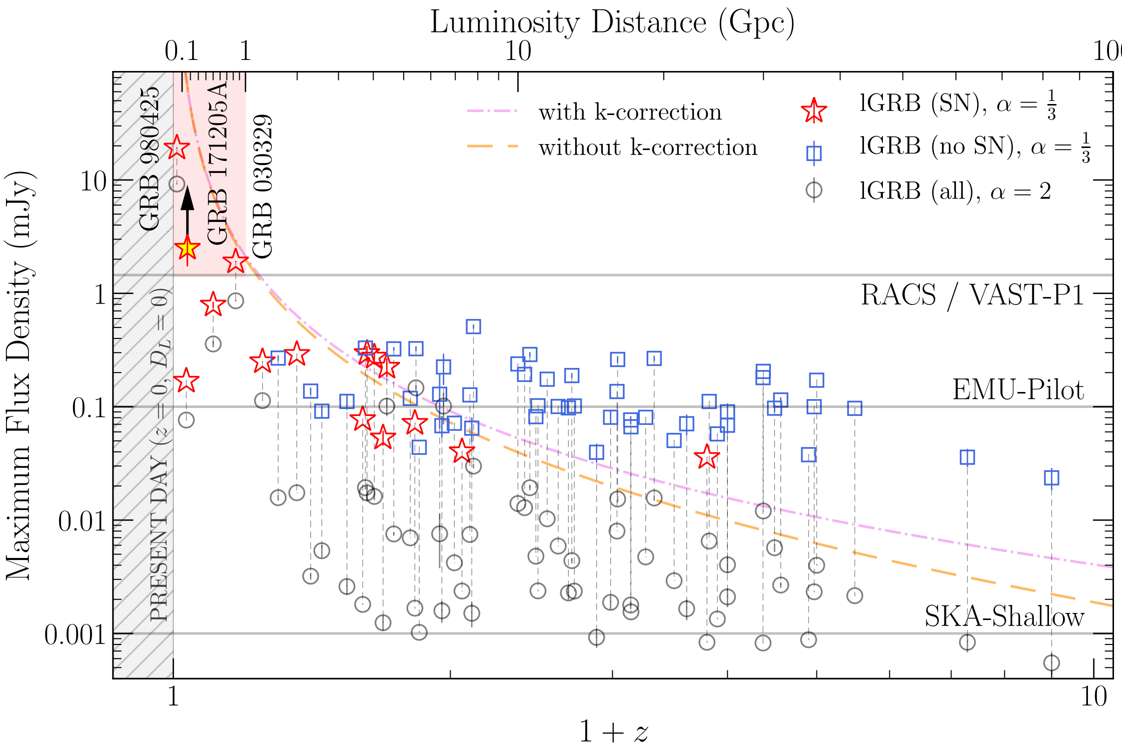

Figure 2.2: The fitted maximum flux density scaled to 887.5 MHz as a function of $1+z$ (bottom axis) and luminosity distance D_L (top axis) for 64 radio afterglows featured in CF12. The maximum flux density refers to the flux density of a radio afterglow at the light curve peak. Each burst is scaled with two different spectral indices, $\alpha = \frac{1}{3}$ (self-absorption is not significant) and $\alpha = 2$ (self-absorption is significant), providing upper and lower bounds, respectively. For the $\alpha = \frac{1}{3}$ scenario, the 14 afterglows with supernova association are plotted with red star markers, while those without are plotted with blue square markers. For the $\alpha = 2$ scenario, all afterglows are plotted with gray circular markers. For each burst, the scaled data points using the two different spectral indices are joined by gray dashed lines. The error bars represent uncertainties in fitting for the maximum flux density, not measurement uncertainties; data points without error bars are measured values, not fitted values; see CF12 for details. The expected relations between the maximum flux density and redshift, assuming a typical spectral luminosity of $L_\nu = 2 \times 10^{30}\,\mathrm{erg\,s^{-1}\,Hz^{-1}}$, are shown for two separate cases: (i) the relation governed by the typical inverse square decrease of the maximum flux density with luminosity distance is shown with the orange dashed line, (ii) the relation accounting for negative k-correction effects leading to the plateauing effect at cosmological distances is shown with the purple dash-dotted line. For a more detailed discussion of the scaling and the dependence of maximum flux density on redshift, see Section 2.3. The gray horizontal lines show the 5σ-limit of different radio surveys considered in this work. The region shaded in red above 1.50 mJy and below $z = 0.2$ ($D_L = 1$ Gpc) represents the parameter space our search is most sensitive to. The lower limit for the maximum flux density of our GRB 171205A afterglow candidate (yellow star marker) is given by its flux density as measured from RACS.

frequency is assumed to be above $\nu_{\rm sa}$ and below the synchrotron frequency corresponding to the peak, $\nu_{\rm m}$, from which we scaled; this corresponds to power-law segment D in GS02. In the $\alpha = 2$ scenario, our observing frequency is assumed to be below $\nu_{\rm sa}$, corresponding to power-law segment B in GS02. In this scenario, the maximum flux density at the frequency we scaled from could either be due to the passage of $\nu_{\rm m}$ (in an ISM environment) or $\nu_{\rm sa}$ (in a wind environment); in both cases, the appropriate spectral scaling is still $\alpha = 2$. Predicting the temporal evolution of the flux density at $\nu_{\rm m}$ as it moves towards our observing frequency requires further modelling for each burst; we consider this beyond the scope of our work and argue that the small difference between the frequency we scaled from (typically 1.43 or 8.46 GHz) and our observing frequency would not result in substantial changes to the flux density at $\nu_{\rm m}$ as it moves towards our observing frequency. We therefore only used the two spectral indices to provide a range on the expected maximum flux density for each burst when scaled to 887.5 MHz and noted that this range should be shifted upwards slightly if the temporal evolution of the synchrotron peak was also factored in.

Considering the $\alpha = 1/3$ spectral scaling, only afterglows from GRB 980425 and GRB 030329 would be detectable in RACS and VAST-P1 at the 5σ-level during the 14 year span covered by CF12. From archival data, the duration, or length of time the radio afterglow would be detectable, for GRB 980425 and GRB 030329, would be approximately 250 (Li & Chevalier, 1999) and 150 days (Frail et al., 2005), respectively. The implied fractional time a radio afterglow from a known GRB is detectable in the sky at the RACS/VAST-P1 flux-density sensitivity is 7.8 per cent. We calculated the probability of detecting a radio afterglow in our search to be 7.2 per cent after factoring in the sky coverage of RACS and VAST-P1 as well as the cadence of our observations. These calculations should be considered as lower limits since less than 20 per cent of known GRBs have been observed at radio frequencies and early-time radio detections from the reverse shock mechanism were not considered in CF12. Considering the $\alpha = 2$ spectral scaling, only GRB 980425 would be detectable in RACS and VAST-P1, implying a probability for detecting a radio afterglow in our search to be 3.7 per cent. For comparison, the number of on-axis radio afterglow detections predicted in Ghirlanda et al. (2013) and Metzger et al. (2015) is of order unity when their predictions for similar surveys are scaled to our search parameters.

Despite the low probability of detecting a typical radio afterglow, the detections of GRB 980425 and GRB 030329 implied that finding a subset of local, radio-bright afterglows in our search was possible. These two GRBs, associated with SN 1998bw (Galama et al., 1998; Kulkarni et al., 1998) and SN 2003dh (Hjorth et al., 2003; Stanek et al., 2003) respectively, suggest this subset of GRBs at redshifts $z < 0.2$ (or luminosity distances $D_L < 1$ Gpc) are often sufficiently local for accompanying broad-lined Type Ic (Ic-BL) supernovae to also be detected. This is a class of supernovae with spectral lines broadened from quasi-relativistic photospheric velocities reaching $\sim$30,000 km s^{-1} (Modjaz et al., 2016) and with kinetic energies reaching $\sim 10^{52}$ erg when accompanied by lGRBs (Mazzali et al., 2014). At more cosmological distances probed by deeper searches, the identification of accompanying supernovae becomes more difficult, but the dependence of the afterglow maximum flux density on redshift becomes weaker due to the negative k-correction effect (Ciardi & Loeb, 2000; Frail et al., 2006). This is represented in Figure 2.2: the conventional inverse square luminosity distance decrease (orange dashed line) follows the relation $L_\nu = 4\pi S_\nu D_L^2/(1+z)$, where L_ν is the spectral luminosity at the observing frequency, S_ν is the flux density, D_L is the luminosity distance and z is the redshift; the negative k-correction factor $(1+z)^{\beta-\alpha}$ multiplied to the aforementioned relation results in a flatter flux-density dependence on redshift (purple dash-dotted line); these lines assume a typical spectral luminosity of $L_\nu = 2\times10^{30}\,\mathrm{erg\,s^{-1}\,Hz^{-1}}$ (CF12) and a post jet break light curve that is optically thin and flat (i.e. spectral index $\alpha = 1/3$, temporal index $\beta = 0$, where $S \propto \nu^\alpha t^\beta$; Frail et al., 2006)[1]. Therefore, the redshift limitations impacting our search would be less severe at the flux-density sensitivities achieved by the deeper EMU survey, and to a larger extent, the Square Kilometre Array Shallow (SKA-Shallow; e.g. Fender et al., 2015) survey in the future.

2.4 Detectability of Afterglows

The detectability of afterglows in our search depended on the flux-density sensitivity of our surveys and the degree of host galaxy contamination present. Only radio afterglows that reached our 5σ-sensitivity threshold of $\sim$1.50 mJy beam^{-1} during our observations could be detectable in our search. We expected our detections to be close to this 5σ-threshold since the majority of previous radio afterglow detections peaked below this threshold level (see Section 2.3).

A radio afterglow emitting above the threshold still needed to be distinguishable from its host galaxy. The radio emission of local galaxies at redshifts $z \ll 1$ follow the relationship:

$$S_{\nu,\,\mathrm{gal}} = 0.3\,\mathrm{mJy}\left(\frac{\mathrm{SFR}}{M_\odot\ \mathrm{yr}^{-1}}\right)\nu_{\mathrm{GHz}}^{-0.8}\,D_{L,27}^{-2}\,, \tag{2.1}$$

where SFR is the star formation rate in units of $M_\odot$ yr^{-1}, ν_{GHz} is the observing frequency in GHz, $D_L = 10^{27} D_{L,27}$ cm is the luminosity distance to the host galaxy and the applied spectral index of -0.8 characterises the synchrotron emission of radio galaxies at gigahertz frequencies (Condon, 1992; Carilli & Yun, 1999; Metzger et al., 2015). The problem of host galaxy contamination was considered for each of the four scenarios below, depending on the radio afterglow localisation with respect to its host galaxy. The four scenarios we discuss are illustrated in Figure 2.3.

1. *The afterglow is offset and resolvable from its host galaxy.* Host galaxies in this scenario are compact and have angular separations from their afterglows that are at least as large as the angular resolution of our observations ($\geq 15''$ for RACS/VAST-P1). Afterglows in this scenario would be

[1] The assumption of $\alpha = 1/3$ holds only for the blue/red (not gray) points in Figure 2.2 while the $\beta = 0$ (flat light curve) carries the assumption of a wind-like circumburst medium. Assuming $\alpha = 2$ (e.g. gray points) and/or an ISM-like circumburst medium with different temporal scalings will therefore result in a different k-correction factor (and associated lines).

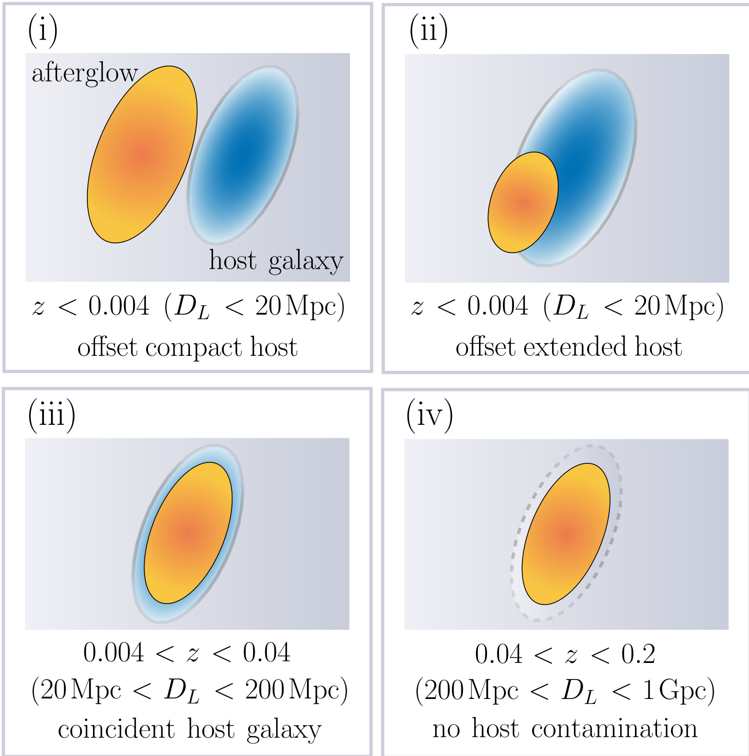

Figure 2.3: Four different scenarios showing how the detectability of radio afterglows may be contaminated by the radio emission of the host galaxies. The typical redshift (and luminosity distance) range for each scenario is given assuming: (a) the typical physical offset of an lGRB afterglow from its host to be $\sim 1.3\,$kpc, (b) the typical star formation rate of a host galaxy to be $1\,M_\odot\,\mathrm{yr}^{-1}$, and (c) the observations are made using a radio telescope with $\sim 15''$ angular resolution. A detailed discussion of these assumptions can be found in Section 2.4.

detectable if their peak flux densities are above our 5σ-sensitivity threshold of $\sim 1.50\,\mathrm{mJy\,beam}^{-1}$.

2. *The afterglow is offset but not clearly resolved from its host galaxy.* Host galaxies that are very local (e.g. $z < 0.03$ for radio galaxy samples in van Velzen et al., 2012) may have extended emission at gigahertz frequencies. An afterglow offset from its host galaxy centre, even by more than $15''$, may be contaminated by this emission and our 5σ-sensitivity threshold criteria would not be enough to determine the detectability of the afterglow. With a RMS scatter in the flux-density scale of ~ 0.3 in RACS/VAST-P1 (see Table 2.1), a 5σ-detection requires the afterglow to reach flux densities ≥ 2.5 times the underlying host emission as measured from previous epochs. If there exists a reference epoch prior to the afterglow detection, the host emission could be modelled and subtracted to varying degrees of fidelity; in this case, the detectability would only depend on the 5σ-sensitivity threshold criteria.

3. *The afterglow is spatially coincident with its host galaxy.* Host galaxies in this scenario are compact and have angular separations from their afterglows that are smaller than half the angular resolution of our observations ($\leq 8''$

for RACS/VAST-P1). Similar to scenario (ii), any afterglow that is spatially coincident with its host galaxy would only be detectable in our search with 5σ-confidence if it reaches flux densities ≥ 2.5 times the flux density of its host galaxy in the epochs prior to detection unless its host emission could be modelled from a reference epoch and subtracted.

4. *The afterglow is found without any detectable host galaxy emission associated with it.* Host galaxies of afterglows in this scenario are too faint to be detected in any epochs of our observations. These afterglows will not be contaminated by host galaxy emission and would be detectable if their peak flux densities are above our 5σ-sensitivity threshold of $\sim$1.50 mJy beam^{-1}.

Physical offsets for lGRBs from their host galaxies range from 0.075 to 14 kpc with a median offset of $\sim$1.3 kpc (Bloom et al., 2002; Blanchard et al., 2016). Assuming the median (maximum) lGRB physical offset, an afterglow would be detected with a $15''$ angular offset from its host galaxy if it is at a redshift of 0.004 (0.046), or equivalently, a luminosity distance of 20 Mpc (200 Mpc). This implies that finding afterglows in scenarios (i) and (ii) with appreciable offsets from their hosts using ASKAP surveys is unlikely since all GRBs found in our sample in Section 2.3 were located at $z > 0.004$ ($D_L > 20$ Mpc). For instance, our lowest redshift sample, GRB 980425, at $z = 0.008$ ($D_L = 40$ Mpc) had a measured angular offset of $12''\!.55 \pm 0''\!.052$ (Bloom et al., 2002), which is below the angular resolution of our observations. This suggests radio afterglows found appreciably offset from their hosts would likely be associated with an extremely local burst $z < 0.004$ ($D_L < 20$ Mpc).

The star formation rate of lGRB host galaxies range from 0.2 to 50 $M_\odot$ yr^{-1} (Berger, 2009) with a median of about 2 $M_\odot$ yr^{-1} (Christensen et al., 2004). Assuming a host galaxy star formation rate of 1 $M_\odot$ yr^{-1}, we argue using Equation 2.1 that host galaxy contamination only becomes significant, i.e. $S_{\nu,\mathrm{gal}} \geq 1$ mJy ($\sim 3\sigma$), at $z < 0.04$ ($D_L < 200$ Mpc). For galaxies with a more active star formation rate of 10 $M_\odot$ yr^{-1}, the host galaxy contamination would be significant for bursts detected at $z < 0.12$ ($D_L < 580$ Mpc). Since we expected the brightest radio afterglows to be detectable at flux densities ≥ 1.50 mJy up to $z = 0.2$ ($D_L = 1$ Gpc), we expected more afterglow detections to fall under scenario (iv) than (iii) as host galaxy contamination was more likely to not be significant.

Consideration of other transients with different offset and luminosity distributions could have different conclusions. For example, typical radio supernovae would be more likely found in scenarios (i) or (ii) because they have larger typical offsets and are detected more abundantly at luminosity distances $D_L < 20$ Mpc due to their lower typical luminosities (Wang et al., 1997). Likewise, radio telescopes with higher angular resolution are also more likely to result in detections corresponding to scenarios (i) or (ii). Radio afterglows detectable in our search needed to be distinguishable from other transient phenomena or disentangled from any coincident background sources. This required further multi-wavelength analysis and telescope time as demonstrated later in Section 2.6.

2.5 Search Methodology

We compiled a comprehensive catalogue of lGRBs detected in the post-*Swift* era, specifically between 2004 December and 2020 January (inclusive). This consisted of $3,005$ bursts primarily detected by the International Gamma-Ray Astrophysics Laboratory (INTEGRAL; Mereghetti et al., 2003), the *Swift* Burst Alert Telescope (BAT; Lien et al., 2016) and the *Fermi* Large Area Telescope (LAT; Ajello et al., 2019) and Gamma-ray Burst Monitor (GBM; von Kienlin et al., 2020). These missions typically localised the bursts to a few arcminutes, with the exception of the *Fermi*-GBM, which had a cruder typical localisation radius of a few degrees. A better localisation to a few arcseconds is often achieved with the automatic search for X–ray and optical afterglows following a trigger from the aforementioned missions with the *Swift* X–ray Telescope (XRT; Evans et al., 2009) and *Swift* Ultraviolet/Optical Telescope (UVOT; Roming et al., 2017), respectively. For our search method and analysis, we required localisation to the level of arcseconds so we only considered lGRBs detected by *Swift*; the wider catalogue we compiled consisting of bursts from other missions was then used as a reference catalogue to assess our search strategy and completeness against in Subsection 2.7.2.

We selected from the $1,225$ lGRBs detected by *Swift* up until 2020 January (inclusive) 779 lGRBs, representing 63.6 per cent of the full *Swift* sample, which were localised in the RACS footprint by *Swift*-XRT/UVOT to $< 15''$. The primary goal of our search was to find and study bright late-time radio emission from this subset of well-localised GRBs. We crossmatched our catalogue of well-localised GRBs against sources extracted from each epoch of RACS and VAST-P1 using an association radius of $15''$, which is the angular resolution for the observations. For all source associations, we used information on the positions of host galaxies and optical data (a demonstration is given in Section 2.6) as well as the detectability criteria discussed in Section 2.4 to determine whether the emission was likely host or afterglow related. For any afterglow candidate(s) found in our search, we searched archival data to determine whether any further follow-up observations were required to confirm and/or characterise the physics of the emission.

There is a possibility that some of these candidates were due to chance spatial coincidence with a background source. We estimated the number of chance coincidence sources $\mathcal{N}_{\rm cc}$ in our search with:

$$\mathcal{N}_{\rm cc} \approx \mathcal{N}_{\rm GRB} \times A_{\rm ar} \times \rho_{\rm vp} \,, \tag{2.2}$$

where $\mathcal{N}_{\rm GRB}$ was the number of well-localised GRBs that were searched for in the RACS and VAST-P1 footprints, $A_{\rm ar}$ was the area on a celestial sphere corresponding to the association radius of the targeted search, and $\rho_{\rm vp}$ was the source density in the VAST-P1 data. Since the measured flux density for most candidates are close to the detection threshold, we used the source density at the detection threshold $\rho_{\rm vp}\,(S \geq 1.50\,{\rm mJy}) \approx 80$ sources per square degree along with our search parameters as inputs for Equation 2.2 and estimated $\mathcal{N}_{\rm cc}$ to be 3.45. We also estimated $\mathcal{N}_{\rm cc}$ numerically by repeating the crossmatch 100 times using simulated GRB positions, with right ascension and cosine of the declination (up to declination $+41^\circ$) generated from a random uniform distribution. The numerical method estimates $\mathcal{N}_{\rm cc} = 4.32 \pm 1.85$, which is in agreement with our analytical estimate.

2.6 Results and Further Analysis

We found four radio source associations in our search. Using the numerical estimate of the expected number of chance coincidence sources, we calculated the probability of all four candidates, at least one candidate and no candidates being afterglow related (rather than chance coincidence sources) to be 2.4, 65.9 and 34.1 per cent, respectively. Three (GRBs 080905B, 110312A and 160216A) were ruled out as imaging artefacts, host galaxy or background emission as expected from our chance coincidence calculations. The radio source associated with GRB 171205A was the remaining afterglow candidate. In this section, we discuss its late-time detection, our follow-up observations with the Australia Telescope Compact Array (ATCA) radio telescope, our reduction of archival early-time radio data and our compilation of multi-wavelength data on this afterglow. More comprehensive explanations on the vetting of other candidates are provided in Section 2.9.

2.6.1 Late-time emission from GRB 171205A/SN 2017iuk

GRB 171205A was detected by the Burst Alert Telescope aboard *Swift* on 2019 December 5 at 07:20:43 UT (D'Elia et al., 2017) and an associated Type Ic-BL supernova SN 2017iuk was detected two days later (de Ugarte Postigo et al., 2017b; Wang et al., 2018). Localised to the galaxy 2MASX J11093966−1235116 at $z = 0.0368$ (Izzo et al., 2017), the burst thus belongs to the subclass of local, low-luminosity GRBs with Type Ic-BL supernova association (D'Elia et al., 2018). Detections of the radio afterglow prior to this work were from early-time observations as summarised in Table 2.2 (above the divider). These include reported detections from the literature, early-time ATCA observations described in Subsection 2.6.3 and a detection from an untargeted Very Large Array (VLA) Sky Survey (VLASS; Lacy et al., 2020) observation. Any detections of the radio afterglow in our search and subsequent follow-up were considered late-time observations; unlike the early-time observations, these probed the behaviour of the afterglow after the synchrotron peak had passed through the radio frequencies and possibly after the blast wave had entered into the sub-relativistic phase.

In our search results, the candidate radio source associated with GRB 171205A was observed only in RACS as it was not in the VAST-P1 footprint. In the follow-up analysis of this radio source, we used the release version of the RACS data products, with improved properties as described in McConnell et al. (2020) and Hale et al. (*in prep.*), for accurate flux-density measurements, instead of the pre-release version used for our search. The RACS tile containing the radio source was reobserved 11 months after the initial observation. While we also provide the flux-density measurements from the reobservation in our paper, we note that at the time of our search, the tile had not been reobserved. The flux-density measurements from both the initial and subsequent observations were low signal-to-noise detections at 6σ to

Table 2.2: Radio observations of the GRB 171205A afterglow. Column 1 shows the start date of the observations or the mean epoch of the observations for those spanning more than two days; Column 2 shows the time of the observations in days post-burst; Column 3 shows the radio telescope or survey used for the observations; Column 4 shows the central frequency of the observations; Column 5 shows the flux-density measurements for detections or the 3σ-limits for non-detections; Column 6 shows references to the initial reports of the observations. Observations above the dividing line are early time observations taken within 3 months of the event and observations below the dividing line are late time observations conducted during or after the epoch of our radio afterglow search.

Date (UT)	ΔT (days)	Telescope or Survey	ν (GHz)	S_ν † (mJy)	Reference
2017 Dec 09.58	4.31	VLA	5.0	2.41 ± 0.12	Laskar et al. (2017); Urata et al. (2019)
			7.1	4.32 ± 0.05	" "
			8.5	5.71 ± 0.05	" "
			11.0	8.42 ± 0.06	" "
			13.5	11.26 ± 0.09	" "
			16.0	14.01 ± 0.11	" "
2017 Dec 10.07	4.76	GMRT	1.4	< 0.180	Chandra et al. (2017a)
2017 Dec 12.00	6.70	ATCA	5.5	4.00 ± 0.18	This work
			9.0	5.98 ± 0.45	" "
			44.0	18.5 ± 2.1	" "
2017 Dec 12.61	7.30	RATAN-600	4.7	< 3	Trushkin et al. (2017)
			8.2	10 ± 3	" "
2017 Dec 15.53	10.22	VLBA	4.4	2.3	Perez-Torres et al. (2018a)
2017 Dec 19.07	13.76	GMRT	1.4	0.782 ± 0.057	Chandra et al. (2017b)
2017 Dec 20.06	14.75	eMERLIN	5.1	7.9 ± 0.4	Perez-Torres et al. (2018b)
2018 Jan 10.70	36.40	ATCA	4.7	7.48 ± 0.47	This work
			5.2	7.88 ± 0.12	" "
			5.5	8.07 ± 0.13	" "
			5.8	8.15 ± 0.14	" "
			6.3	8.47 ± 0.14	" "
			8.2	8.50 ± 0.15	" "
			8.7	8.61 ± 0.16	" "
			9.0	8.78 ± 0.16	" "
			9.3	8.69 ± 0.17	" "
			9.8	8.65 ± 0.16	" "
			44.0	15.4 ± 1.2	" "
2018 Feb 01.35	58.04	VLASS	3.0	5.80 ± 0.46	Lacy et al. (2020)
2018 Feb 19.61	76.00	ATCA	4.7	7.28 ± 0.27	This work
			5.2	7.54 ± 0.20	" "
			5.5	7.70 ± 0.21	" "
			5.8	8.21 ± 0.41	" "
			6.3	8.02 ± 0.32	" "
			8.2	8.63 ± 0.25	" "
			8.7	8.73 ± 0.28	" "
			9.0	8.90 ± 0.27	" "
			9.3	8.94 ± 0.29	" "
			9.8	9.15 ± 0.33	" "

continued on the following page

continued from the previous page

Date (UT)	ΔT (days)	Telescope or Survey	ν (GHz)	S_ν [†] (mJy)	Reference
2019 Apr 30.39[‡]	511.08	RACSe1	0.8875	2.51 ± 0.76	This work
2020 Mar 26.63[§]	842.31	RACSe2	0.8875	1.94 ± 0.70	This work
2020 Apr 12.46	859.15	ATCA	2.1	0.71 ± 0.25	This work
			5.5	0.41 ± 0.05	" "
			9.0	0.25 ± 0.03	" "
			16.7	0.11 ± 0.04	" "
			21.2	< 0.09	" "
2020 May 07.26	883.95	ATCA	2.1	0.82 ± 0.29	This work
			5.5	0.44 ± 0.05	" "
			9.0	0.24 ± 0.03	" "
			16.7	0.13 ± 0.05	" "
			21.2	< 0.12	" "

[†] Uncertainties for GCN Circulars are as reported. Uncertainties for VLASS and RACS measurements consist of a statistical and systematic component (∼8 per cent for VLASS and ∼30 per cent for RACS) added together in quadrature.
[‡] This is the observation of the afterglow initially detected in our search.
[§] Some tiles of RACS were reobserved. RACSe1 refers to the initial observation and RACSe2 refers to the subsequent observation. All mentions of RACS observations in the text refer to RACSe1 unless specified otherwise.

7σ; the integrated flux-density measurements were fitting into the noise and could be unreliable as a result, so we used the peak flux-density measurements instead assuming the radio source was unresolved.

With only one data point at the time of the search, the source variability could not be characterised and the host-afterglow degeneracy could not be broken. Using Equation 2.1, the range of possible SFR estimates for the host galaxy from $\sim 1\,M_\odot$ yr^{-1} (Wang et al., 2018) to $3 \pm 1 M_\odot$ yr^{-1} (Perley & Taggart, 2017) predicted host emission ranging from 1.2 to 4.9 mJy; while this is consistent with the measured flux density of the source, there is considerable uncertainty on the expected flux density of the host galaxy. To further verify whether the origin of the radio emission was related to afterglow and not host activity, we searched for evidence of positional offset between the fitted radio source position and the host galaxy. Since this offset was unlikely to be resolvable in the RACS data, we instead searched for this in a Panoramic Survey Telescope and Rapid Response System (Pan-STARRS; Chambers et al., 2016) g-band image with sub-arcsecond resolution as shown in Figure 2.4. This figure shows the positional offset of the radio source from the observed optical afterglow position (Izzo et al., 2017) is 1.″2 and the positional offset from the identified host galaxy, 2MASX J20065732−6233465, is 4.″7. The RACS tile for this source has an astrometric accuracy of $2.''1 \pm 3.''1$ in right ascension and $0.''3 \pm 2.''3$ in declination as defined by the median positional offset of sources in the tile with respect to their positions in the NRAO VLA Sky Survey (NVSS; Condon et al., 1998). These astrometric uncertainties imply that while the radio source position is more consistent with the afterglow than the host galaxy, further observations described in Subsection 2.6.2 were required to confirm this and to further characterise the properties of the late-time emission.

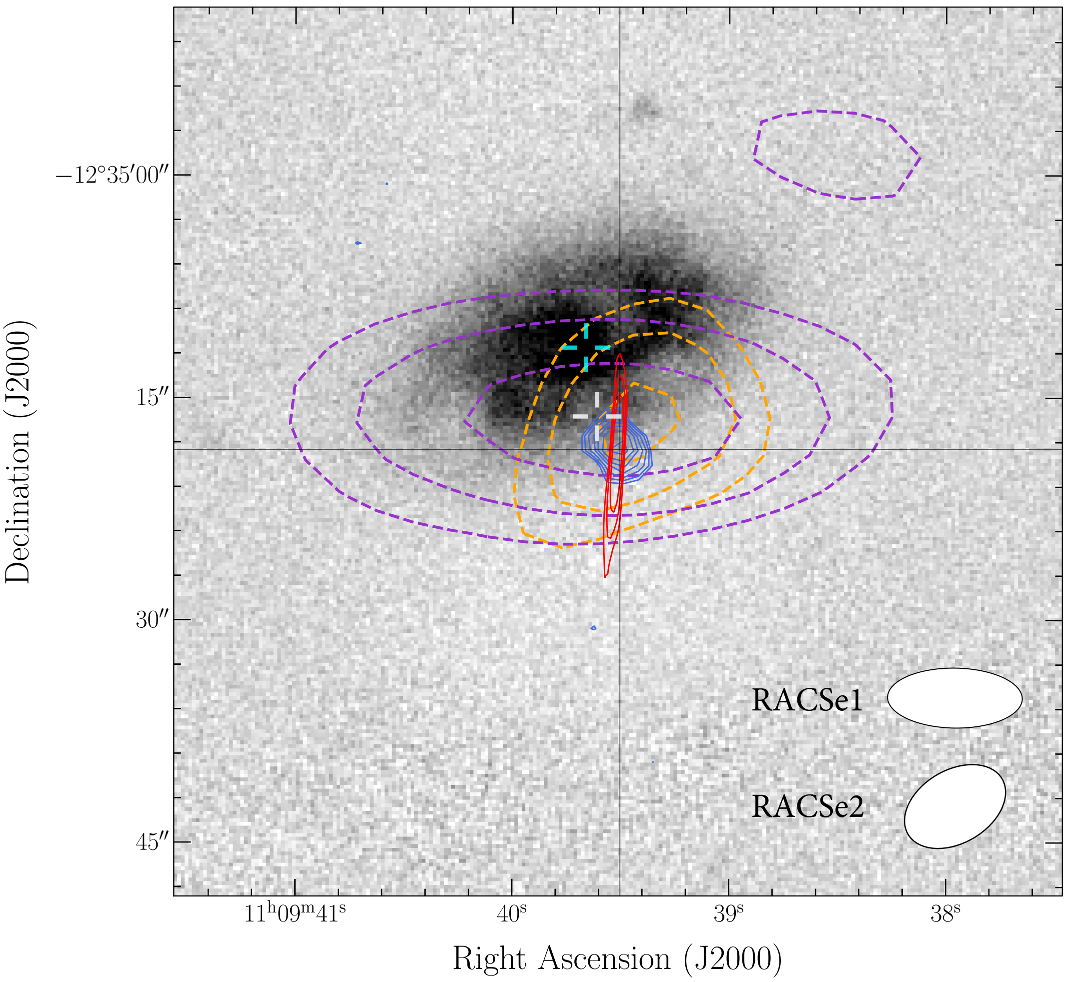

Figure 2.4: The Pan-STARRS g-band optical image of host galaxy 2MASX J11093966−1235116 is overlaid with radio contours from RACSe1 (purple, dashed), RACSe2 (orange, dashed), VLASS (blue, solid) and our 9.0 GHz ATCA observations taken on 2020 May 07 (red, solid). The lowest contours start at the 3σ-level and increase by a factor of $\sqrt{2}$ at each subsequent level. The PSF shapes corresponding to the RACSe1 and RACSe2 radio contours are shown on the bottom right. The two crosshairs represent the position of the host galaxy centre (cyan, upper) and the fitted position of the radio source in RACSe1 (white, lower). The size of the gap in each crosshair is approximately $1''$, indicative of the astrometric uncertainty of the radio source in RACSe1. The image is $1' \times 1'$, centred on the observed position of the GRB optical afterglow from Izzo et al. (2017), with North up and East to the left.

2.6.2 Late-time ATCA Observations and Data Reduction

We observed the radio source associated with GRB 171205A twice more, on 2020 April 12 UT and on 2020 May 7 UT, with ATCA under project C3363 (PI: T. Murphy). For both epochs, the array was in the 6A configuration with a maximum baseline of 6 km and the source was observed at multiple bands – centred on 2.1, 5.5, 9.0, 16.7 and 21.2 GHz – each with a bandwidth of 2, 048 MHz.

We reduced the visibility data using standard MIRIAD procedures (Sault et al., 1995). We used a combination of manual and automatic radio-frequency interference flagging before calibration, conducted with MIRIAD tasks UVFLAG and PGFLAG, respectively. In both epochs for all frequency bands, we used PKS B1934−638 to set the flux-density scale and PKS B1127−145 to calibrate the time-variable complex gains. We also used PKS B1934−638 to determine the bandpass response in both epochs for all frequency bands, except in the 16.7/21.2 GHz bands. For these two exceptions, we used 3C 279 (B1253−055) as the bandpass calibrator for the first epoch and PKS B0727−115 for the second epoch. We determined the flux-density model for these bandpass calibrators using MIRIAD task UVFMEAS. For the 2.1 GHz band, we flagged the data from short baselines ($< 2,800$ m) to reduce the amount of confusion from an extended, known NVSS source, J110939.0−123330, directly north of the afterglow candidate. This problem of flux contamination from a nearby source was only significant at 2.1 GHz due to the lower angular resolution of the telescope in this frequency band. After calibration, we inverted and applied the multi-frequency synthesis CLEAN algorithm (Högbom, 1974; Clark, 1980; Sault & Wieringa, 1994) to the target source field using standard MIRIAD tasks INVERT, MFCLEAN and RESTOR to obtain our final images.

We detected a clear point source at 5.5/9 GHz in both epochs, but it appeared slightly extended at 2.1 GHz due to the aforementioned source confusion and at 16.7 GHz due to low signal-to-noise. The source was not detected at 21.2 GHz in either epoch. The flux densities of the radio afterglow candidate extracted from the images using MIRIAD task IMFIT are reported in Table 2.2 (below the divider). For this task, we assumed a point-source model instead of a Gaussian model to avoid problems associated with fitting into the noise, especially for the 2.1- and 16.7-GHz observations. Our detections in all frequency bands in both epochs confirmed the radio emission to be spatially consistent with the GRB/SN position, but not the host galaxy position; for example, this is clear from the radio emission at 9 GHz from the second epoch with beam size $11\farcs67 \times 0\farcs83$ overlaid in red on top of the Pan-STARRS image in Figure 2.4. We used a least-squares fit to constrain the spectral index α of the radio source in both epochs; in the first epoch, $\alpha_1 = -0.89 \pm 0.09$, and in the second epoch, $\alpha_2 = -0.99 \pm 0.15$. With both the flux densities and spectral indices found to be consistent within their uncertainties between the two epochs, we used the data points across both epochs for a combined least-squares fit, constraining the spectral index further to $\alpha_{\rm combined} = -0.92 \pm 0.07$.

2.6.3 Early-time ATCA Observations and Data Reduction

We supplemented our late-time ASKAP and ATCA data with archival early-time ATCA data to provide a more complete physical interpretation for GRB 171205A in Subsection 2.7.1. This subsection describes these early-time ATCA observations and our data reduction process.

GRB 171205A was observed three times with ATCA between 2017 December 12 and 2018 February 19 (7 to 76 days post-burst) under target-of-opportunity program CX401 (PI: M. Michałowski). Observations were carried out using four 2, 048 MHz bands centred on 5.5, 9, 43 and 45 GHz for the first two epochs, while only the 5.5 and 9 GHz bands were used for the last epoch. We combined the 43/45 GHz data to form a single 4, 096 MHz band centred on 44 GHz and split the 5.5/9 GHz data into 512 MHz sub-bands after calibration to image separately.

We reduced the data using Miriad, with automated flagging applied and manual flagging where necessary, similar to our late-time ATCA data reduction in Subsection 2.6.2. We used PKS B1934−638 as the primary calibrator to set the flux-density scale for all observations. We also used PKS B1934−638 to calibrate the bandpass at 5.5/9 GHz, but not at 44 GHz. For the 44 GHz band, we used 3C 279 (B1253-055) and PKS B1124-186 to calibrate the bandpass in the first and second epochs, respectively. We used PKS B1127-145 and PKS B1124-186 to calibrate the time-variable complex gains at 5.5/9 and 44 GHz, respectively.

To correct for phase errors, we performed standard self-calibration using Miriad task gpscal, with a single iteration used at 5.5 GHz and two at 44 GHz. We detected a point source coincident with the position of GRB 171205A in each image at all three epochs. The source was marginally extended at 44 GHz due to scatter in the model image induced by phase errors, which could not be entirely mitigated with self-calibration. Full details of the flux-density measurements are reported in Table 2.2 (above the divider).

2.6.4 Multi-wavelength Observations

In Figure 2.5 and Figure 2.6, we show the multi-wavelength light curve and broadband spectral energy distribution (SED) evolution of the afterglow, respectively. These plots bring together all the multi-wavelength data in the literature on the burst, including radio (Table 2.2), millimetre/sub-millimetre (de Ugarte Postigo et al., 2017a; Perley et al., 2017; Smith & Tanvir, 2017; Urata et al., 2019), near-infrared/optical/ultraviolet (D'Elia et al., 2018; Izzo et al., 2019), and X–ray (flux density at 10 keV; Evans et al., 2010)[2] data points.

For the broadband SED in Figure 2.6, we analysed the X–ray spectra using data from the *Swift*-XRT, which started observing the burst 145 seconds after the trigger (D'Elia et al., 2017). We extracted the XRT spectra from the public *Swift* repository[3] and analysed them with Xspec (version 12.10.1f; Arnaud, 1996). We fitted

[2] https://www.swift.ac.uk/burst_analyser/00794972/

[3] https://www.swift.ac.uk/user_objects/

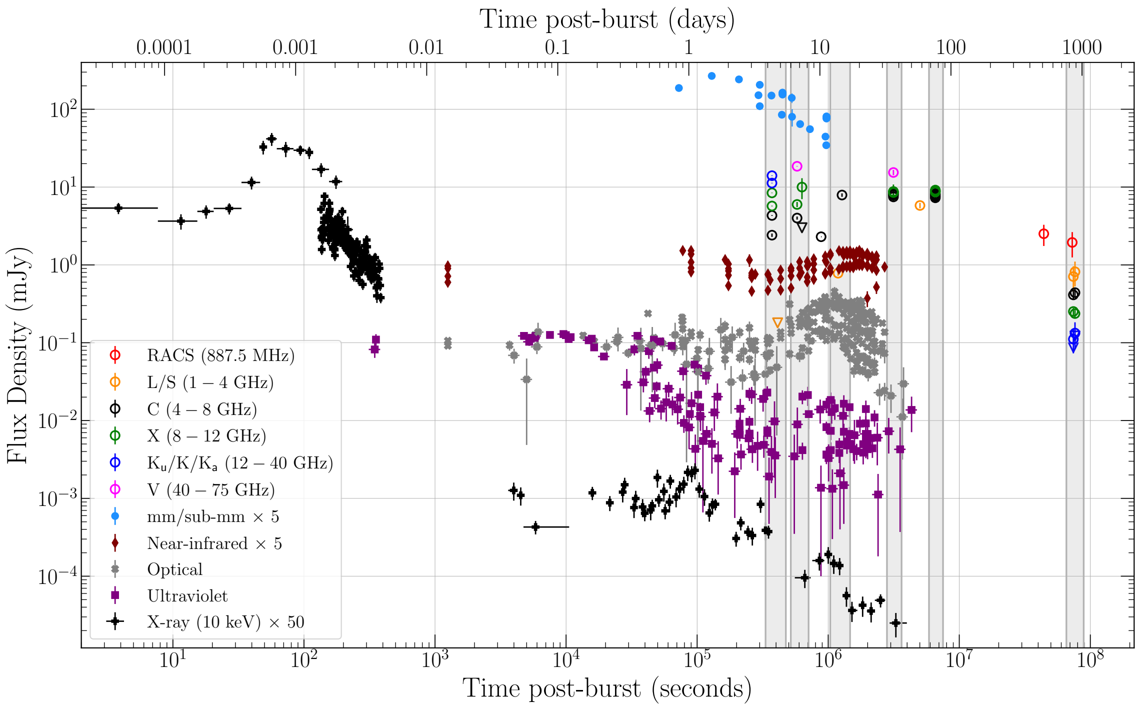

Figure 2.5: Multi-wavelength light curve for GRB 171205A/SN 2017iuk showing both the prompt, thermal and afterglow emission. The light curve shows data points for all observations of GRB 171205A/SN 2017iuk presented in this work and in the literature to date. Observations at radio frequencies probe the afterglow emission of the burst. They are represented by open circular markers (3σ-limits represented by open triangular markers) and are distinguished in colour by their radio band. The details of each radio data point are summarised in Table 2.2. Observations at other wavelengths may have additional contributions from prompt and thermal supernova emission (see Subsection 2.7.1 text for details). They are represented by solid markers and are distinguished in colour by their electromagnetic spectrum classification. For clarity, limits are omitted and data points in the millimetre/sub-millimetre, infrared, and X–ray (10 keV) bands have been scaled by a factor of 5, 5, and 50, respectively. The gray-shaded vertical stripes represent the gross epochs from which the SEDs shown in Figure 2.6 were constructed.

the extracted spectra with an absorbed power-law model, adopting the Tubingen-Boulder ISM absorption model (TBABS; Wilms et al., 2000)[4]. The X–ray spectrum obtained by accumulating all XRT observations starting from 4 days post-trigger (225.7 ksec exposure time) was best fitted by an absorbed power law with equivalent hydrogen column density $N_H = 1.22^{+0.13}_{-0.10} \times 10^{21}\,\mathrm{cm}^{-2}$ (90 per cent confidence), photon index $\Gamma = 1.70^{+0.36}_{-0.32}$ and de-absorbed flux integrated over the 0.3–10 keV energy range $F = 4.1 \pm 0.9 \times 10^{-14}\,\mathrm{erg\,cm^{-2}\,s^{-1}}$. This photon index, corresponding to a spectral index of $0.70^{+0.36}_{-0.32}$, is consistent with the spectral index derived from late-time radio observations in Subsection 2.6.2. In order to show the evolution of the broadband SED in Figure 2.6, we extracted two XRT spectra at 4.3–7.3 days (SP1 – 9 ksec exposure time) and 7.3–14.75 days (SP2 – 38.2 ksec exposure time). We fitted an absorbed power-law model with N_H fixed to the value reported above, which is consistent with that found from the analysis of the early-time XRT data by D'Elia et al. (2017). The photon spectral indices were $\Gamma_{\mathrm{SP1}} = 2.19^{+1.13}_{-0.98}$ and $\Gamma_{\mathrm{SP2}} = 1.6^{+1.36}_{-0.36}$,

[4] https://heasarc.gsfc.nasa.gov/xanadu/xspec/manual/node265.html

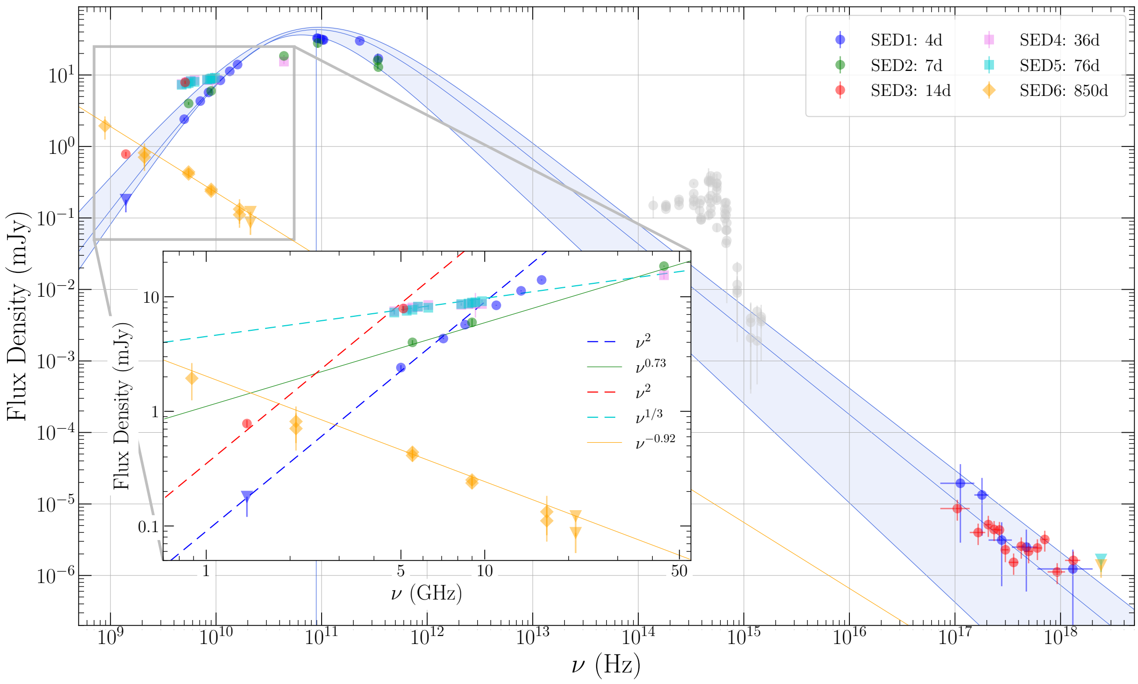

Figure 2.6: The broadband SED of the GRB 171205A afterglow taken at six epochs (approximately 4, 7, 14, 36, 76 and 850 days post-burst) from X–ray down to radio frequencies, with the inset zooming into the radio frequencies. Observations in the near-infrared to ultraviolet regime are shown in gray and are not included in any fits because they are contaminated by an additional thermal supernova component. Non-detections are given by their 3σ-limits (downward triangular markers). Spectral fits to data points are displayed as solid lines, while comparison lines representing typical spectral indices from segments of the standard afterglow spectrum are displayed as dashed lines. For SED1 (4 days post-burst), a smoothly broken power-law fit is applied (blue, with 1σ-uncertainty shaded in light blue) to show the injection frequency $\nu_{\rm m}$ located between the radio and millimetre/sub-millimetre frequencies. By analysing the evolution of the radio and broadband SED across the six epochs, we inferred the circumburst medium of the burst to be consistent with a stellar wind environment and the late-time radio emission (from RACS and ATCA observations) to be afterglow dominated (see Subsection 2.7.1 text for details).

i.e. consistent within their uncertainties. SP1 and SP2 are represented, respectively, in Figure 2.6 with blue and red markers, corresponding to SED1 and SED3, as described below.

The data points in Figure 2.5 (light curve) are grouped by their electromagnetic wavebands, represented by different marker shapes and colours. The radio data points are split into further sub-bands and are distinguished from other wavelengths by open markers. To highlight the spectral evolution of the afterglow, we grouped the observations into six gross epochs and show the SED at each of these epochs in Figure 2.6 (broadband SED). These epochs correspond to observations taken approximately 4 days (SED1: blue), 7 days (SED2: green), 14 days (SED3: red), 36 days (SED4: pink), 76 days (SED5: cyan), and 850 days (SED6: orange) post-burst. Data points within these epochs are not perfectly contemporaneous, but we argue this is acceptable for the subsequent analysis since the evolution of the afterglow on the timescale of days to tens of days is quite slow. The windows for each epoch are shown by the gray vertical stripes in Figure 2.5.

For each epoch in the radio inset of Figure 2.6, a spectral fit line (solid) or a comparison line corresponding to a standard afterglow spectral segment (dashed) is displayed on top of the data points. In the wider broadband SED plot, data from the first epoch are fit to a smoothly broken power law (blue line, with 1σ-uncertainty shaded in light blue):

$$S_\nu = S_{\text{peak}} \left[\left(\frac{\nu}{\nu_{\text{peak}}}\right)^{-s\delta_1} + \left(\frac{\nu}{\nu_{\text{peak}}}\right)^{-s\delta_2} \right]^{-1/s}, \tag{2.3}$$

where S_{peak} is the flux density at the peak, ν_{peak} is the frequency at which the turnover occurs, δ_1 is the slope of the spectral rise, δ_2 is the slope of the spectral decay, and s is the smoothing factor. The Markov chain Monte Carlo fit was performed using the EMCEE (Foreman-Mackey et al., 2013) PYTHON implementation with uniform priors on all parameters, yielding a fit with $S_{\text{peak}} = 39.40^{+4.86}_{-5.53}$ mJy, $\nu_{\text{peak}} = 54.69^{+8.93}_{-10.79}$ GHz, $\delta_1 = 1.95^{+0.30}_{-0.20}$, $\delta_2 = -1.19^{+0.05}_{-0.20}$, and $s = 0.32^{+0.10}_{-0.08}$. The value of the fitted peak parameters differ slightly to the true functional peak (of 43.18 mJy located at 89.00 GHz) due to the smoothing factor.

2.7 Discussion

2.7.1 GRB 171205A/SN 2017iuk Interpretation

The multi-wavelength light curve in Figure 2.5 highlights many features of the GRB 171205A/SN 2017iuk system discussed in the literature. The X–ray observations probed the prompt emission and revealed a possible thermal component in the very early phases of the X–ray light curve; the origin of which is still under debate (D'Elia et al., 2018). The near-infrared/optical/ultraviolet was dominated at early times (up to ∼3 days) by a thermal component (Izzo et al., 2019). The spectroscopic studies of this emission highlighted ultra-fast expansion velocities and element abundances, which favour its origin from a hot cocoon of material produced by the jet breaking out of the stellar envelope (Izzo et al., 2019). The optical/UV light curve shows the rise of the SN 2017iuk starting ∼3 days post-burst (de Ugarte Postigo et al., 2017b); spectroscopic observations confirmed this (Wang et al., 2018). The millimetre/submillimetre observations probed for radio linear polarisation from the afterglow; the detection of which is still under debate (Urata et al., 2019; Laskar et al., 2020). In this subsection, we extended the multi-wavelength analysis of this system into radio frequencies, using the data presented in Table 2.2 to conduct an empirical investigation into the afterglow properties.

We noted the radio 8–12 GHz light curve (green open markers in Figure 2.5) peaked around 50–70 days, i.e. after the supernova peak at ∼13 days. We ascribed this radio peak as due to the evolution of the characteristic frequencies of the afterglow synchrotron spectrum across the low-frequency bands.

The radio inset of Figure 2.6 details this spectral evolution through the six epochs described in Subsection 2.6.4. In the first SED (4 days post-burst), the radio spectrum featured a steep slope (with some curvature) consistent with a spectral index $\alpha = 2$ (fitted as $1.95^{+0.30}_{-0.20}$ by the smoothly broken power law), typical for the self-absorbed segment of the afterglow spectrum. By the second epoch (7 days post-burst), the spectrum exhibited a flatter slope fitted as 0.73 ± 0.01, which we interpreted to be in mid-transition towards the $\alpha = 1/3$ spectral slope, typical for the spectral segment between $\nu_{\rm sa} < \nu < \nu_{\rm m}$. The slope in the third SED (14 days post-burst) remained consistent with $\alpha = 2$ as it was sampled at lower frequencies. However, between the third and fourth epochs (14 and 36 days post-burst), a complete transition from the $\alpha = 2$ to $\alpha = 1/3$ spectral slope occurred. In particular, this transition indicates the passage of the self-absorption frequency through $\nu = 5\,{\rm GHz}$ at some time between 14 and 36 days post-burst. The flux density measurements remained similar from the fourth to fifth SED (36 and 76 days post-burst), both consistent with the typical spectral slope of $\alpha = 1/3$.

The observed SED evolution of GRB 171205A over these first five epochs provided us with clues on the properties of its circumburst medium (e.g. Chevalier & Li, 2000). The GRB jet expands into a medium whose particle density, varying as a function of distance r from the progenitor, is described as $n(r) = Ar^{-k}$. In the wind (homogeneous ISM) environment, the density drops (remains constant) with distance from the progenitor, i.e. $k = 2$ ($k = 0$). While the scaling constant A is just the particle density of the ISM in the homogeneous scenario, n_0, it is related to the mass-loss rate $\dot{M}_w$ and stellar wind velocity v_w of the progenitor star by $A = \dot{M}_w/4\pi v_w = 5 \times 10^{11} A_* \,{\rm g\,cm^{-1}}$ in the wind scenario. Here, A_* is a normalisation of A, such that $A_* = 1$ represents a typical Wolf-Rayet star with mass-loss rate $\dot{M}_w = 10^{-5}\,M_\odot\,{\rm yr^{-1}}$ and stellar wind velocity $v_w = 1,000\,{\rm km\,s^{-1}}$.

We argue the GRB 171205A/SN 2017iuk event occurred in a stellar wind environment induced by the progenitor prior to its core-collapse (see also Suzuki et al. 2019). The radio spectral evolution in the first five epochs, in particular, the emergence of the $\alpha = 1/3$ slope in the fourth and fifth SED, was due to the passage of the self-absorption frequency, $\nu_{\rm sa}$, across the gigahertz frequency range. According to standard afterglow theory (e.g. GS02), $\nu_{\rm sa}$ only evolves with time, shifting towards lower frequencies, in the wind scenario. The flux-density levels in the fourth and fifth SED, sampled after the passage of $\nu_{\rm sa}$ through the band, were also very similar; this is consistent with the wind scenario, where the flux density is predicted to remain constant in the $\nu_{\rm sa} < \nu < \nu_{\rm m}$ spectral segment (GS02). Our conclusion that the afterglow is produced by the relativistic outflow decelerating in a circumburst medium with a wind density profile is in agreement with the conclusion obtained by the independent analysis of Maity & Chandra (2021) using observations from the upgraded Giant Metrewave Radio Telescope.

The very late-time SED (850 days post-burst) enabled us to constrain the slope of the electron spectrum p, where the distribution of electron energies is $N(E) \propto E^{-p}$. According to Maity & Chandra (2021), even at $\sim$1,000 days post-burst, the blast wave had not transitioned to the non-relativistic (Newtonian) regime. A spectral inversion occurred between the fifth and sixth SED (76 and 850 days post-burst), where the spectral index transitioned from $\alpha = 1/3$ to $\alpha = -0.92$. This indicates that $\nu_{\rm m}$ had moved from between the millimetre and radio frequencies at 4 days post-burst and passed through the entire radio frequency band shown in the SED at some time between 76 and 850 days post-burst; by 850 days post-burst, $\nu_{\rm m}$ was located below the 887.5 MHz sampling band. This very late-time SED, as sampled by the radio data, is therefore located in the spectral segment $\nu_{\rm m} < \nu < \nu_{\rm c}$, where $\nu_{\rm c}$ is the frequency of the cooling break, with characteristic spectral index $\alpha = (1-p)/2$. Comparing this with the fitted spectral index of this SED attained in Subsection 2.6.2, $\alpha = -0.92 \pm 0.07$, we constrained the slope of the electron spectrum to $p = 2.84$. While this value deviates from the typical $p \sim 2.2$ expected from Fermi acceleration processes, it is consistent to within one standard deviation of the distribution of p-values obtained from afterglow modelling (Ryan et al., 2015; Wang et al., 2015; Ghisellini et al., 2009). Moreover, particle-in-cell simulations (e.g. Sironi & Spitkovsky, 2011) have shown that possible variations in the magnetic structure at the shock front could produce different values of p.

The fit of SED1 (blue points in Figure 2.6) with a single spectral component between the peak in the radio and the X–ray data points suggests that already at these early epochs the cooling frequency $\nu_{\rm c}$ lies above the X–ray energy range. This is consistent with the similar spectral slopes found in the two X–ray spectra we analysed since $\nu_{\rm c}$ should increase with time in the wind scenario.

The broadband SED corresponding to SED1–3 in Figure 2.6 shows that the radio/millimetre (above 89 GHz) through X–ray spectrum is consistent with a single non-thermal component, while the near-infrared/optical data points (gray markers) contaminated by thermal supernova emission are located above the corresponding empirical fit (blue line with shaded region). Moreover, the extrapolation of the very late-time $\alpha = -0.92$ spectral slope from the radio frequencies through to the X–rays is consistent with the very late-time upper limits derived from XRT observations. Along with the consistency of the X–ray spectral indices presented in Subsection 2.6.4 with the very late-time radio spectral index, these suggest the emission we sampled in the radio band starting from 4 days post-burst was dominated by the afterglow component.

As the radio SEDs are dominated by the afterglow component of the burst event, we used these observables to provide reasonable estimates for the microphysical shock parameters of the blast wave, including the normalised wind-density parameter A_*, the fractional energy in electrons ϵ_e, and the fractional energy in the magnetic field ϵ_B. These observables are related to the microphysical shock parameters by a set of analytical relations detailed in Panaitescu & Kumar (2000). For a stratified wind medium, the self-absorption frequency is:

$$\nu_{\rm sa} = 3.7 \times 10^9\, E_{53}^{-2/5}\, A_*^{6/5}\, \epsilon_{e,-1}^{-1}\, \epsilon_{B,-2}^{1/5}\, T_d^{-3/5}\, {\rm Hz}\,, \tag{2.4}$$

where $E = 10^{53} E_{53}$ erg is the kinetic energy of the blast wave and T_d is the time (in days) since the burst explosion[5]. The flux density at the self-absorption frequency,

[5]We note that times and frequencies should be converted from the source to the observer frame accounting for the source redshift. However, in this case, the $z = 0.0368$ would introduce corrections of the order unity.

$S_{\nu,\mathrm{sa}}$, is then related to ν_{sa} at time T_d by the relation:

$$S_{\nu,\mathrm{sa}} = 0.07\, D_{L,28}^{-2}\, E_{53}\, A_*^{-1}\, \epsilon_{e,-1}\, \nu_{\mathrm{sa},9.7}^{2}\, T_{d,-1}^{1}\, \mathrm{mJy}\,, \tag{2.5}$$

where $D_L = 10^{28} D_{L,28}$ cm is the luminosity distance of the source. A similar relation to Equation 2.4 providing the location of the injection frequency, ν_{m}, at time T_d is given by:

$$\nu_{\mathrm{m}} = 1.9 \times 10^{13}\, E_{53}^{1/2}\, \epsilon_{e,-1}^{2}\, \epsilon_{B,-2}^{1/2}\, T_d^{-3/2}\, \mathrm{Hz}\,. \tag{2.6}$$

To estimate the microphysical shock parameters using our observables and these relations, we fixed the luminosity distance parameter to $D_L = 5.17 \times 10^{26}$ cm corresponding to the afterglow redshift of $z = 0.0368$ (Izzo et al., 2017) and fixed the energy parameter to $E_{53} = 0.00218$ corresponding to the approximation of the blast-wave kinetic energy as ten times the energy released in the prompt emission $E_{\mathrm{prompt}} = 2.18 \times 10^{49}$ erg (D'Elia et al., 2018).

In Equations 2.4 and 2.5, we estimated the time T_d and flux density $S_{\nu,\mathrm{sa}}$ at which the self-absorption frequency ν_{sa} passed 5 GHz using SED3 and SED4 (14 and 36 days post-burst) in Figure 2.6. In the wind scenario, the flux density is expected to rise linearly with t in the self-absorbed spectral segment and stay constant in the spectral segment between ν_{sa} and ν_{m}. Given this, we argue, with the 5.1 GHz data point shown on SED3 lying on the $\alpha = 1/3$ line alongside SED4 data points, ν_{sa} was likely already at 5 GHz around 14 days post-burst. We thus used the self-absorption break at $\nu_{\mathrm{sa}} = 5$ GHz with $S_{\nu,\mathrm{sa}} = 7.9$ mJy and $T_d = 14$ days as our observables for Equations 2.4 and 2.5. These numbers are only estimates since we do not see a clear self-absorption break in any SED; ν_{sa} may have crossed 5 GHz at any time between 14 and 36 days. For Equation 2.6, while none of the radio SEDs in Figure 2.6 show a spectral break corresponding to the injection frequency ν_{m}, SED6 (850 days post-burst) provides an observable boundary condition; it suggests ν_{m} at $T_d = 850$ days post-burst lies below 887.5 MHz.

To estimate A_*, ϵ_e and ϵ_B, we solved the set of non-linear Equations 2.4–2.6 using a non-linear least-squares optimisation routine in the SciPy (Virtanen et al., 2020) Python library. We imposed the following constraints on the free parameters: $A_* > 0$, $0 < \epsilon_e, \epsilon_B < 1$ and $0 < \nu_{\mathrm{m}} < 887.5$ MHz; the last constraint implemented the boundary condition associated with SED6 and Equation 2.6. This yields us the following estimates for the microphysical shock parameters: $A_* = 3$, $\epsilon_e = 0.3$ and $\epsilon_B = 0.0002$, where the boundary-defining parameter takes the value $\nu_{\mathrm{m}} = 46$ MHz for this solution. The low value of ϵ_B we derived is consistent with the wide distributions of values estimated from the modelling of GRB afterglows (e.g. 10^{-10} to 10^{-3} in Barniol Duran 2014, 10^{-6} to 10^{-3} in Santana et al. 2014). These low values can explain the properties of the afterglow emission at very high energies as detected by *Fermi*-LAT (Beniamini et al., 2015) and have been interpreted to be due to the possible decay of the magnetic field in the downstream region behind the external shock (Lemoine et al., 2013). While we have shown plausible estimates of the microphysical parameters can be derived from our data, these estimates are very sensitive to our assumptions; more accurate estimates would require full afterglow modelling across relativistic and sub-relativistic regimes, which is beyond the scope of this paper.

2.7.2 Search Strategy Considerations

In this work, we limited our search to well-localised bursts to reduce the number of false, or coincident, associations. Since this localisation is often achieved by *Swift*-XRT/UVOT, we introduced a bias towards bursts with detectable afterglows at X–ray, UV and optical wavelengths. For example, bursts with detectable afterglows are more likely to be associated with certain physical properties, such as a higher circumburst density (e.g. Piran, 2004). If we removed this localisation requirement and searched for radio afterglow candidates within the GRB error radius, we would be able to provide follow-up observations for approximately three times as many, or $\sim$2,000 more, GRBs.

In this scenario, the problem of false associations becomes significant. Using a typical error radius of $5'$ in Equation 2.2, we find that the number of expected false associations would be 1,370. With poor localisation and large number of false associations, our method for distinguishing afterglow and host-related emission by analysing positional offsets in optical images would not be very effective. Instead, a search without the localisation criterion would need an additional variability requirement to reduce the number of false associations (the source density used in Equation 2.2 would then be the density of variable sources in VAST-P1). Since the VAST-P1 footprint is the only region with multiple epochs in our search, a search requiring variability analysis would reduce our sky coverage by a factor of $\sim$7 (when compared with including RACS), and correspondingly, the expected afterglow detection rates estimated in Section 2.3 would also decrease by a factor of $\sim$7. When a deep, single epoch sky map from EMU (see Subsection 2.7.3) is completed, it can be used as a reference epoch for this type of time-domain analysis; this will reduce the false association rate for searches in future surveys, regardless of whether these surveys are multi-epoch or not.

Due to these considerations, there were significant challenges in using previous generations of wide coverage radio surveys, in particular, NVSS and SUMSS, to conduct a similar search. These surveys conducted in the pre-*Swift* era would have significantly fewer well-localised bursts to follow-up and the lack of multi-epoch data hindered the ability to conduct further variability analysis for these bursts with larger error radius.

Given our choice to limit our search to well-localised bursts, we also did not consider any bursts occurring prior to 2004, the launch year of *Swift*. Due to this constraint, our search was unable to test late-time rebrightening theories for GRB/SN systems since this phenomenon is predicted to occur on the timescales of a few decades and usually at sub-mJy flux-density levels (e.g. Peters et al., 2019). Still, our search was sensitive to local, radio-bright GRB/SN afterglows as demonstrated by the detection of late-time emission from the GRB 171205A/SN 2017iuk system. This suggests orphan afterglow searches using the current generation of wide coverage radio surveys, such as RACS and VAST-P1, may also be sensitive enough to detect off-axis emission from these systems, providing an alternative to orphan afterglow searches guided by supernova association (e.g. off-axis GRB detection via association with Type Ic-BL SN 2020bvc; Izzo et al., 2020).

2.7.3 GRB Yields in Comparison Radio Surveys

Our ASKAP search for radio afterglows probed for radio emission from 587 GRBs that were not previously observed by the Arcminute Microkelvin Imager (AMI; Anderson et al., 2018), ATCA, or VLA, and resulted in one detection. With the sensitivity improvements expected in future radio surveys, for example, the SKA-Shallow survey targeting a 5σ-detection threshold of $1\,\mu$Jy beam^{-1}, similar searches will be able to study greater classes of GRB events, including sGRBs, useful for identifying electromagnetic counterparts to gravitational wave events, and high-redshift GRBs, useful for probing Population-III stars. These expected improvements to sensitivity in such searches will enable sufficient detections for population analyses of radio afterglows to be conducted, providing useful experiments to better understand the nature of radio-quiet and -loud GRBs, for example. In this subsection we compare the GRB yields of our search using RACS and VAST-P1 to various surveys, including the EMU Pilot Survey, commensal ASKAP surveys and the SKA-Shallow survey.

Our search covered $\sim 40,000$ square degrees and the detection of one low-luminosity GRB afterglow above our 5σ-sensitivity threshold of ~ 1.50 mJy beam^{-1} implies a transient surface density $\rho \gtrsim 1 \times 10^{-4}\,\text{deg}^{-2}$. This is consistent with the gigahertz frequency transient surface density prediction for low-luminosity GRBs in Figure 3 of Metzger et al. (2015) calculated to be $\rho \approx 5 \times 10^{-4}\,\text{deg}^{-2}$. Following our detection of the GRB 171205A radio afterglow up to 842 days post-burst in RACS, we extended the time baseline for our rates analysis in Section 2.3 from 2011 to 2020. We searched online databases[6,7] for radio afterglow detections up to 2020 January and manually searched the literature for radio flux-density measurements of each detection. We found that aside from GRB 171205A, no lGRB radio afterglows reached a peak flux density above the 5σ-sensitivity threshold of ~ 1.50 mJy beam^{-1} at 887.5 MHz. However, the radio afterglow from Very High Energy ($E > 100$ GeV) lGRB 190829A, occurring in the VAST-P1 footprint two days after our first epoch of observations, may have been marginally detectable, i.e. at 4σ-significance, with more favourable timing, having peaked at 1.52 ± 0.22 mJy beam^{-1} at an observing frequency of 1.3 GHz (Rhodes et al., 2020). The new information improves the probability of detecting a radio afterglow calculated in Section 2.3 to 13.3 per cent (11.3 per cent), assuming the $\alpha = 1/3$ (2) spectral scaling scenario. While this probability suggests the detection of GRB 171205A afterglow in our search was unlikely, its detection could be attributed to the extreme nature of the event, being the second brightest afterglow detected to date at radio frequencies.

Surveys reaching lower flux-density thresholds are required to probe for classes of GRBs beyond the subset of local, radio-bright GRB/SN systems. We consider the expected GRB yield of some of these surveys here, assuming a more conventional 1.4-GHz observing frequency, spectral scaling with $\alpha = 1/3$ where necessary and an optimistic one month afterglow duration (the typical duration differs significantly from the very local GRB/SN systems considered in Section 2.3 and would vary

[6] Jochen Greiner database: www.mpe.mpg.de/~jcg/grbgen.html
[7] *Swift* database: swift.gsfc.nasa.gov/archive/grb_table.html

depending on the flux-density threshold; see, for example, CF12 and Ghirlanda et al., 2013). The EMU Pilot Survey, conducted with the same amount of observation time as VAST-P1, reached a 5σ-sensitivity threshold of 100 µJy beam^{-1}, but covers $\sim$10 per cent ($\sim$2 per cent) of the VAST-P1 (RACS) sky regions as shown in Figure 2.1. This limited sky coverage produces a worse probability for radio afterglow detection of 0.3 per cent, after repeating the analysis in Section 2.3 for the EMU Pilot Survey. Unlike the subset of GRBs with supernovae association previously considered, radio follow-up of typical lGRBs at more cosmological distances is more sparse (only 18 per cent of lGRBs receive radio follow-up), meaning the use of the (CF12) sample alone underestimates the detection probability for the EMU Pilot Survey; yet, accounting for this only boosts the probability of detection up to 1.6 per cent.

Aside from the consideration of sky coverage, analysing positional offsets in optical images as demonstrated in this work will not be enough to distinguish afterglow from host emission for the EMU Pilot Survey and other deeper surveys. As shown in Figure 2.2, deeper surveys will detect afterglows up to a higher redshift, but the host-afterglow offset at higher redshifts will be too small. For example, GRB 171205A at $z = 0.0368$ had a noticeable angular offset of $5\farcs9$ from its host, translating to a physical offset of $\sim$4.4 kpc; but if it had a typical (median) lGRB physical offset of $\sim$1.3 kpc instead, the angular offset would be $< 2''$. Variability analysis over multiple epochs would be required and this is not possible with the single epoch EMU Pilot Survey.

The full ASKAP surveys (e.g. EMU and VAST) will be conducted with a commensal approach; depending on the cadence, multi-epoch deep surveys with large sky coverage may be available. For example, the full EMU survey aims to cover the entire RACS footprint at the EMU Pilot Survey sensitivity, requiring $\sim$10 hr of integration per tile. In the extreme cases, the 10 hr could be observed through 10 min pointings with 60 visits per tile over 5 years (i.e. 1 visit per month) or through two 5 hr pointings per tile separated by over a year; a hybrid between these two extremes is likely more realistic. The former will reach a 5σ-sensitivity threshold similar to our RACS/VAST-P1 search and has a 47.8 per cent probability (based of a similar analysis to that in Section 2.3) of detecting a radio afterglow from a known local radio-bright GRB/SN system, while the latter will reach a 5σ-sensitivity threshold of $\sim$150 µJy beam^{-1} and has a 62.4 per cent (16.2 per cent if we do not account for GRBs that do not receive radio follow-up) probability of detecting a radio afterglow from a broader class of known on-axis GRBs.

These ASKAP surveys, which are expected to yield a number of radio afterglow detections of order unity, are precursors to more potent SKA-era surveys. The proposed SKA-Shallow survey, for example, covering half the sky to sub-µJy sensitivity with daily cadence would provide radio follow-up to all bursts in the half-sky and deeper non-detection limits than any other radio telescope to date. While the ASKAP surveys used in our work still do not reach the flux-density sensitivity required for placing stringent tests on radio rebrightening theories and conjectures regarding distinct radio-quiet/loud GRB populations, applying a similar search methodology and analysis to SKA-era surveys will enable these experiments as well as further insights into the general radio afterglow population to be realised.

2.8 Conclusions

We have conducted a search for radio afterglows from 779 well-localised lGRBs occurring after 2004 by crossmatching their positions with radio sources in the RACS and VAST-P1 data. Analysing the positional offset of the radio source and host galaxy in optical images was the primary method we used to distinguish afterglow from background or host related emission for matched sources. Our search produced four candidates, three of which were ruled out as background source or host-galaxy related, while one was confirmed as a radio afterglow from GRB 171205A, a low-luminosity lGRB associated with SN 2017iuk.

We conducted further late-time observations of the GRB 171205A radio afterglow with ATCA at 859 and 884 days post-burst. Both the flux densities and spectral indices were measured to be consistent within their uncertainties between the two epochs. Our late-time radio observations provided a robust measurement of the electron spectral index and also provided the bounded constraint on the injection frequency (see Equation 2.6) required to solve for the other microphysical parameters. Using this late-time data alongside archival data from early-time radio observations, we showed the progenitor of this GRB-SN system originated in a stellar wind environment with microphysical shock parameters of the burst estimated as $p = 2.84$, $A_* = 3$, $\epsilon_e = 0.3$ and $\epsilon_B = 0.0002$.

While we estimated a probability of < 10 per cent for detecting any radio afterglows in our search, we were able to probe for a subset of radio-bright lGRBs in the local Universe at $z < 0.2$ (or $D_L < 1\,\mathrm{Gpc}$) that were often accompanied by supernova detections. In order to probe for other GRB classes through deeper surveys or to overcome biases from choosing to only follow-up well-localised lGRBs, multiple epochs of data will be required in addition to the analysis of positional offsets in optical images. The integration time and cadence of these epochs in full commensal ASKAP surveys will determine the classes of GRBs similar searches would be sensitive to in the future. Our method of analysing positional offsets in optical images will also be applied in ongoing searches in our RACS and VAST-P1 data for explosive transients expected to be offset from a host, including orphan afterglows, magnetars, fast radio burst afterglows, and more.

Acknowledgements

We thank the anonymous referee and Phil Edwards for useful comments that improved the quality of this manuscript. JL, DD and JP are supported by Australian Government Research Training Program Scholarships. TM acknowledges the support of the Australian Research Council through grants FT150100099 and DP190100561. DK is supported by National Science Foundation grant AST-1816492. Parts of this research were conducted by the Australian Research Council Centre of Excellence for Gravitational Wave Discovery (OzGrav), through project number CE170100004.

The Australian Square Kilometre Array Pathfinder is part of the Australia Telescope National Facility which is managed by CSIRO. Operation of ASKAP is funded by the Australian Government with support from the National Collaborative Research Infrastructure Strategy. ASKAP uses the resources of the Pawsey Supercomputing Centre. Establishment of ASKAP, the Murchison Radio-astronomy Observatory and the Pawsey Supercomputing Centre are initiatives of the Australian Government, with support from the Government of Western Australia and the Science and Industry Endowment Fund. We acknowledge the Wajarri Yamatji as the traditional owners of the Murchison Radio-astronomy Observatory site. The Australia Telescope Compact Array is part of the Australia Telescope National Facility which is funded by the Australian Government for operation as a National Facility managed by CSIRO. We acknowledge the Gomeroi people as the traditional owners of the Paul Wild Observatory site.

The Pan-STARRS1 Surveys (PS1) and the PS1 public science archive have been made possible through contributions by the Institute for Astronomy, the University of Hawaii, the Pan-STARRS Project Office, the Max-Planck Society and its participating institutes, the Max Planck Institute for Astronomy, Heidelberg and the Max Planck Institute for Extraterrestrial Physics, Garching, The Johns Hopkins University, Durham University, the University of Edinburgh, the Queen's University Belfast, the Harvard-Smithsonian Center for Astrophysics, the Las Cumbres Observatory Global Telescope Network Incorporated, the National Central University of Taiwan, the Space Telescope Science Institute, the National Aeronautics and Space Administration under Grant No. NNX08AR22G issued through the Planetary Science Division of the NASA Science Mission Directorate, the National Science Foundation Grant No. AST-1238877, the University of Maryland, Eotvos Lorand University (ELTE), the Los Alamos National Laboratory, and the Gordon and Betty Moore Foundation. The national facility capability for SkyMapper has been funded through ARC LIEF grant LE130100104 from the Australian Research Council, awarded to the University of Sydney, the Australian National University, Swinburne University of Technology, the University of Queensland, the University of Western Australia, the University of Melbourne, Curtin University of Technology, Monash University and the Australian Astronomical Observatory. SkyMapper is owned and operated by The Australian National University's Research School of Astronomy and Astrophysics. This work made use of data supplied by the UK Swift Science Data Centre at the University of Leicester.

Software: Astropy (Astropy Collaboration et al., 2013, 2018), emcee (Foreman-Mackey et al., 2013), Matplotlib (Hunter, 2007), NumPy (Harris et al., 2020), pandas (McKinney, 2010), SciPy (Virtanen et al., 2020), ASKAPsoft (Cornwell et al., 2011; Guzman et al., 2019), Selavy (Whiting & Humphreys, 2012), Miriad (Sault et al., 1995), and Xspec (Arnaud, 1996).

Data Availability

The ASKAP data used in this paper (RACS and VAST-P1) can be accessed through the CSIRO ASKAP Science Data Archive (CASDA[8]) under project codes AS110 and AS107. The ATCA data used in this paper can be accessed through the Australia Telescope Online Archive (ATOA[9]) under project codes CX401 and C3363. Other auxiliary datasets can be made available upon request via email to the corresponding author.

2.9 Appendix: Ruled-out Afterglow Candidates

In Section 2.6, we ruled out three of the four afterglow candidates in the vetting process. For each candidate, we provide an explanation and show in Figure 2.7 their corresponding radio and optical images.

Candidate 1 (GRB 080905B) – This matched radio source found in RACS is likely to be related to the host galaxy, 2MASX J20065732−6233465. The fitted radio source position is more spatially consistent with the host position ($0\farcs7$ offset) than with the GRB position ($4\farcs5$ offset).

Candidate 2 (GRB 110312A) – This matched radio source is the only candidate located within the VAST-P1 footprint and it was detected in all epochs of our search. The emission is either host galaxy related or from a coincident background source since the radio source is not spatially consistent with the GRB position ($14\farcs3$ offset).

Candidate 3 (GRB 160216A) – This matched radio source found in RACS is not spatially consistent with the GRB position ($5\farcs7$ offset) and is likely to be either host galaxy related or from a coincident background source. It is also possible this is an imaging artefact caused by a local noise peak close to the detection threshold.

Candidate 4 (GRB 171205A) – This matched radio source found in RACS is a confirmed afterglow candidate. The details are discussed in Section 2.6.

[8] https://data.csiro.au/dap/public/casda/casdaSearch.zul
[9] https://atoa.atnf.csiro.au/query.jsp

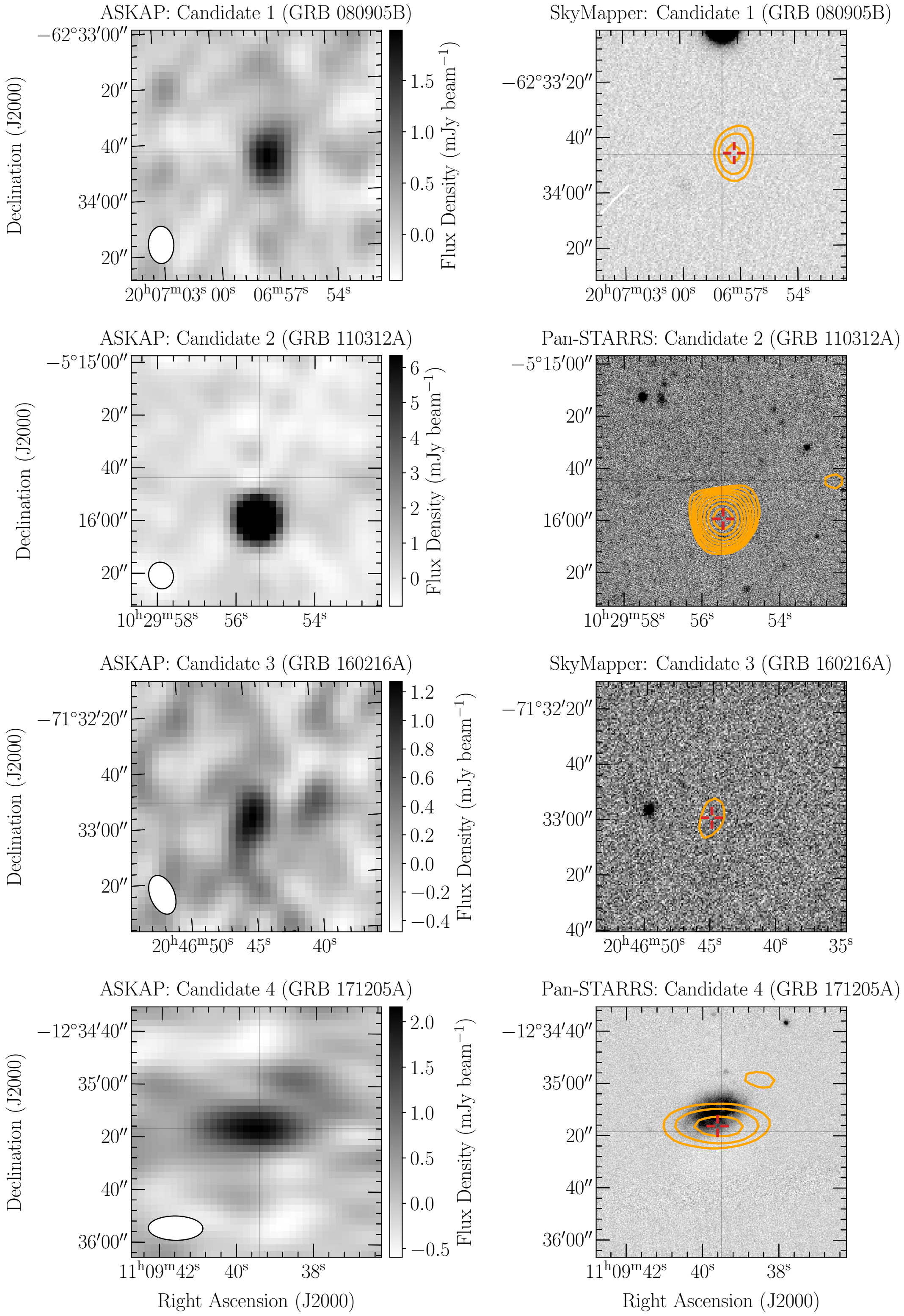

Figure 2.7: The ASKAP image (left) and optical image (right) for each afterglow candidate found in our search. All ASKAP images are from RACS, with the exception of the Candidate 2 (GRB 110312A) ASKAP image taken from epoch 8 of VAST-P1. The optical images shown are g-band images from either SkyMapper (Onken et al., 2019, Candidates 1 and 3) or Pan-STARRS (Candidates 2 and 4) with radio contours from their corresponding ASKAP images overlaid (orange). The lowest contours start at the 3σ-level and increase by a factor of $\sqrt{2}$ at each subsequent level. The red crosshair represents the fitted radio position of the afterglow candidate. All images are $1'.5 \times 1'.5$, centred on their corresponding *Swift*-XRT/UVOT localised afterglow positions, with typical localisation errors of a few arcseconds. North is up and East is to the left.

Chapter 3

A matched-filter approach to radio variability and transients: searching for orphan afterglows in the VAST Pilot Survey

James K. Leung[1,2,3] Tara Murphy,[1,3] Emil Lenc,[2] Philip G. Edwards,[2] Giancarlo Ghirlanda,[4,5] David L. Kaplan,[6] Andrew O'Brien,[6] and Ziteng Wang[1,2,3]

[1]Sydney Institute for Astronomy, School of Physics, The University of Sydney, NSW 2006, Australia
[2]CSIRO Space and Astronomy, PO Box 76, Epping, NSW 1710, Australia
[3]ARC Centre of Excellence for Gravitational Wave Discovery (OzGrav), Hawthorn, VIC 3122, Australia
[4]INAF – Osservatorio Astronomico di Brera, via E. Bianchi 46, I–23807 Merate (LC), Italy
[5]INFN – Sezione di Milano–Bicocca, Piazza della Scienza 3, 20126 Milano (MI), Italy
[6]Department of Physics, University of Wisconsin-Milwaukee, P.O. Box 413, Milwaukee, WI 53201, USA

This chapter is reproduced from Leung et al. (2023a), published in Monthly Notices of the Royal Astronomical Society as "A matched-filter approach to radio variability and transients: searching for orphan afterglows in the VAST Pilot Survey". The majority of the work in this chapter was done by myself. The co-authors contributed to the VAST Pilot Survey products used directly in this work (described in Section 3.1); provided general guidance on radio transients, AGN, and/or GRB science; and provided feedback on the manuscript drafts.

Abstract

Radio transient searches using traditional variability metrics struggle to recover sources whose evolution timescale is significantly longer than the survey cadence. Motivated by the recent observations of slowly evolving radio afterglows at gigahertz frequency, we present the results of a search for radio variables and transients using an alternative matched-filter approach. We designed our matched-filter to recover sources with radio light curves that have a high-significance fit to power-law and smoothly broken power-law functions; light curves following these functions are characteristic of synchrotron transients, including "orphan" gamma-ray burst afterglows, which were the primary targets of our search. Applying this matched-filter approach to data from Variables and Slow Transients Pilot Survey conducted using the Australian SKA Pathfinder, we produced five candidates in our search. Subsequent Australia Telescope Compact Array observations and analysis revealed that: one is likely a synchrotron transient; one is likely a flaring active galactic nucleus, exhibiting a flat-to-steep spectral transition over 4 months; one is associated with a starburst galaxy, with the radio emission originating from either star formation or an underlying slowly evolving transient; and the remaining two are likely extrinsic variables caused by interstellar scintillation. The synchrotron transient, VAST J175036.1−181454, has a multi-frequency light curve, peak spectral luminosity, and volumetric rate that is consistent with both an off-axis afterglow and an off-axis tidal disruption event; interpreted as an off-axis afterglow would imply an average inverse beaming factor $\langle f_{\rm b}^{-1} \rangle = 860^{+1980}_{-710}$, or equivalently, an average jet opening angle of $\langle \theta_{\rm j} \rangle = 3^{+4}_{-1}\,$deg.

3.1 Introduction

In the standard fireball model, a gamma-ray burst (GRB) produces a panchromatic afterglow when the ultra-relativistic jet decelerates into the circumburst medium (Mészáros & Rees, 1997). Owing to the relativistic beaming effect, the solid angle of the observable emitting region Ω increases over time as the bulk Lorentz factor Γ of the relativistic blast wave decreases: $\Omega(t) \propto 1/\Gamma(t)^2$.

Orphan afterglows refer to those unaccompanied by an early, high-energy, prompt counterpart, which is beamed within the initial jet opening angle $\theta_{\rm j}$. They could arise from two scenarios: a "dirty fireball" origin or an off-axis viewing angle (Rhoads, 2003). In the former scenario, a low initial bulk Lorentz factor Γ_0 (this is the Lorentz factor Γ before the jet decelerates, corresponding to the prompt emission phase of the GRB) may prevent the escape of photons during the prompt emission phase as a consequence of large pair production opacity; however, it would still produce afterglow emission observable at longer wavelengths (e.g., Dermer et al., 1999). In the latter scenario, the observer is viewing a classical afterglow off the jet axis, where the viewing angle $\theta_{\rm obs}$ is beyond the jet opening angle $\theta_{\rm j}$, i.e., $\theta_{\rm obs} \geq \theta_{\rm j} \gtrsim 1/\Gamma_0$ (Rhoads, 1997). Here, the off-axis observer would not see the GRB prompt emission, but as the jet expands and decelerates to $\Gamma \approx 1/\theta_{\rm obs}$, the panchromatic afterglow becomes visible from wider viewing angles.

Distinguishing these two scenarios remains an observational challenge, given the similarities in their expected light curves and spectral properties (e.g., Huang et al., 2002; Granot et al., 2018b). A well-sampled multi-wavelength light curve rise could provide the opportunity to distinguish these scenarios – the presence of a fast X–ray transient, a shorter optical flux peak time, and early-time radio scintillation, would all provide evidence favouring the dirty fireball over the off-axis scenario (e.g., Huang et al., 2002). These early-time light curves, however, are very difficult to obtain to the required sensitivity, especially when an orphan afterglow is discovered at longer wavelengths (since the emission may have already fallen below detectability thresholds at shorter wavelengths after its discovery).

Still, attempting to find orphan afterglows and subsequently distinguishing them between these two scenarios would provide useful insights into the properties of GRBs. Detecting a sample of dirty-fireball afterglows could reveal whether they lie on a continuum with classical GRBs with high-baryon purity or whether there is a parametric dichotomy between the two classes, enhancing our understanding of the underlying physics of the progenitors (e.g., Eichler, 2011). Studying off-axis afterglows could tighten constraints on the true rate of GRBs and the typical inverse beaming fraction, i.e., the ratio of all bursts to only those visible along the line-of-sight towards Earth, given as $\langle f_{\rm b}^{-1} \rangle \cong 2/\theta_{\rm j}^2$ (e.g., Frail et al., 2001). The population jet geometry could then be investigated by comparing empirical rates against predicted rates assuming different jet structures, e.g., top-hat jet (Ghirlanda et al., 2014), a universal structured jet (Rossi et al., 2008), or others.

Detections of any orphan afterglows in the past have been scarce owing to their faint flux levels. The confirmation of any candidates has also been challenging due to the difficulty in distinguishing them from other slow transients; for example, supernovae and active galactic nuclei (AGNs) can often be sources of transient confusion in radio survey searches. Despite these challenges, unconfirmed orphan afterglow candidates in radio survey searches (Levinson et al., 2002; Gal-Yam et al., 2006) and non-detections of GRB radio counterparts in late-time follow-up of type Ibc supernova systems (Soderberg et al., 2006) proved to be useful early on as they together allowed the typical inverse beaming fraction to be constrained to $60 < \langle f_{\rm b}^{-1} \rangle < 10^4$.

Recently, improvements in search methods, instrumentation, and modelling have led to the discovery of likely orphan afterglow candidates. Photometric and spectral observations of SN 2020bvc pointed to the presence of a jet-cocoon[1], while the X–ray observations were consistent with an afterglow component; the emission was therefore attributed to a GRB viewed off-axis by $\sim 23°$, making this the first putative orphan afterglow discovery through an association with type Ic broad-line supernovae (Ho et al., 2020b; Izzo et al., 2020). New unbiased optical surveys have yielded orphan afterglow candidates – e.g., the Palomar Transient Factory discovery of PTF11agg (Cenko et al., 2013), a likely dirty fireball, and the Zwicky Transient Facility discoveries of ZTF20aajnksq/AT2020blt, ZTF21aaeyldq/AT2021any, and ZTF21aayokph/AT2021lfa (Ho et al. 2022; see also Sarin et al. 2022, Gupta et al. 2022, Xu et al. 2023, and Lipunov et al. 2022), likely afterglows of on-axis GRBs missed by high-energy satellites. Modelling of X–ray transient CDF-S XT1 from the unbiased *Chandra* Deep-Field South Survey showed the transient could be possibly interpreted as a slightly off-axis ($\sim 10°$) short GRB orphan afterglow (Sarin et al., 2021). While these high-energy and optical transient surveys are more effective for finding on-axis GRBs and dirty fireballs, they are less sensitive than radio transient surveys to the off-axis orphan afterglows beamed away from the observer at larger angles (e.g., Frail et al., 2001; Chandra & Frail, 2012) and to events in dark dust-obscured regions (e.g., Djorgovski et al., 2001).

Previous wide-field radio surveys (e.g., Mooley et al., 2016, and references therein) lacked the sensitivity, sky coverage, and sampling cadence required to detect orphan afterglows and other extragalactic transients. To overcome these challenges, the current generation of telescopes and design of unbiased transient surveys (e.g., Murphy et al., 2013; Shimwell et al., 2017; Woudt et al., 2018; Lacy et al., 2020) have incorporated various improvements that boosted their sensitivity towards extragalactic transients. A comparison of sources in the first epoch of the VLA Sky Survey (VLASS; Lacy et al., 2020) with sources in the Faint Images of the Radio Sky at Twenty-cm (FIRST; Becker et al., 1995) survey has already led to the discovery of a decade-long extragalactic transient, FIRST J141918.9+394036 (Law et al., 2018). Follow-up observations, including Very Long Baseline Interferometry (VLBI) and optical spectroscopy of the host galaxy, support the interpretation that

[1]Signatures of a jet cocoon have previously been found in long GRB / supernova events (e.g., GRB 171205A/SN 2017iuk; Izzo et al., 2019). In this scenario, the GRB jet is launched into the progenitor's stellar layers. The energy injection provided by the jet will give rise to a hot cocoon, which expands laterally to the jet itself. When the relativistic jet successfully penetrates the circumstellar material, it will produce a GRB and the standard afterglow emission. Meanwhile, the cocoon will continue to expand at mildly-relativistic velocities as it breaks out of the progenitor photosphere and will contribute additional thermal and non-thermal emission components.

the transient is likely an off-axis afterglow at a low redshift $z = 0.01957$, although an alternative interpretation of the transient as a nebula of a newly born magnetar has not been ruled out (Marcote et al., 2019; Mooley et al., 2022).

The Australian SKA Pathfinder (ASKAP; Johnston et al., 2007; Hotan et al., 2021) is an array of thirty-six 12 m antennas located at Inyarrimanha Ilgari Bundara, the CSIRO Murchison Radio-astronomy Observatory, operating between 700 and 1 800 MHz. The ASKAP survey for Variables and Slow Transients (VAST; Murphy et al., 2013) is being conducted using this telescope, taking advantage of its large $\sim$30 deg^2 nominal field-of-view and capability of reaching 1 mJy beam^{-1} rms in 1 min of integration. Its ability to detect sources at the $\sim$1 mJy level over more than 10 000 deg^2 makes it sensitive to discovering orphan afterglows (Ghirlanda et al., 2014), along with other extragalactic synchrotron transients, e.g., tidal disruption events (TDEs), type Ibc supernovae, etc. (Metzger et al., 2015).

One difficulty in detecting orphan afterglows and other extragalactic transients in gigahertz-frequency surveys is the slow evolution of their light curves (see for example, the temporal decay of GRB 171205A as observed by ASKAP and uGMRT – Leung et al., 2021a; Maity & Chandra, 2021). This is because emission from relativistic cosmic explosions peak at the gigahertz-band only at late-time when the blast wave has decelerated to mildly- or sub-relativistic speeds (e.g., Chandra & Frail, 2012). Since traditional variability metrics, such as the reduced chi-square and modulation index (e.g., Kesteven et al., 1976; Mooley et al., 2013; Rowlinson et al., 2019; Murphy et al., 2021), are designed for finding variables or transients varying significantly on the timescales probed by the search, finding these slow transients in gigahertz variability surveys with observing cadence of a few months or shorter (which are the majority of such surveys) via a standard variability search will be challenging; this is discussed in more detail in Section 3.5. We have instead applied a matched-filter approach to finding slow transients in unbiased gigahertz surveys (also see Feng et al. 2017), which involves recovering sources with light curves having high-significance fits to smoothly broken power-law (SBPL) and power-law (PL) functions, characteristic of synchrotron transients, rather than just those with high epoch-to-epoch variability.

In this paper, we apply this method to search for orphan afterglows and other extragalactic synchrotron transients in the VAST Pilot Survey (VAST-P; Murphy et al., 2021), spanning a total of 28 months from 2019 April 25 to 2021 August 24. These observations and the pipeline we used for light-curve extraction are outlined in Section 3.1. We detail our matched-filter search methodology for finding orphan afterglows in Section 3.3 and the follow-up observations/interpretation of the resulting candidates in Section 3.4. Finally, we conclude with discussing the possible implications of our results on both transient and GRB rates as well as for future radio transient studies in Section 3.5.

In this paper, we assume a flat Λ-CDM cosmology with $H_0 = 67.8\,\mathrm{km\,s^{-1}\,Mpc^{-1}}$, $\Omega_\mathrm{M} = 0.308$, and $\Omega_\Lambda = 0.692$ (Planck Collaboration et al., 2016).

3.2 Observations & Light-curve Extraction Pipeline

We used data from the first (VAST-P1) and second (VAST-P2) phases of the VAST Pilot Survey in our search for orphan afterglows and the subsequent follow-up of candidates. Using the VAST pipeline (Pintaldi et al., 2022), we associated sources across epochs in the data to build the light curves, which were the primary inputs of our search detailed in Section 3.3.

Table 3.1: Table of VAST-P observations. Columns 1 through 5 show the epoch label, the number of fields in each epoch, the start and end dates for each epoch, and the total sky area covered for each epoch. Observations from VAST-P1 are given above the divider and observations from VAST-P2 are below the divider. Epochs 0 and 14 were conducted as part of RACS (only the subset of RACS observations overlapping with the VAST-P low- and mid-band footprints, respectively, are included), while epochs 15x and 16x were quality-gate observations conducted prior to the planned set of VAST-P2 observations. Epochs having labels suffixed with an 'x' only cover a subset of the full footprint and epoch having labels suffixed with an asterisk (*) were taken at the mid-band (1 367 MHz image central frequency) while the others were taken at the low-band (888 MHz image central frequency). Our slow-transients pipeline run and orphan afterglow search only used the low-band observations, with the mid-band observations being used only in our candidate follow-up process.

Epoch	No. of Fields	Start Date (UT)	End Date (UT)	Sky Area (deg^2)
0	113	2019 Apr 25	2020 May 3	5 006†
1	113	2019 Aug 27	2019 Aug 28	5 131
2	108	2019 Oct 28	2019 Oct 31	4 905
3x	43	2019 Oct 29	2019 Oct 29	2 168
4x	34	2019 Dec 19	2019 Dec 19	1 672
5x	81	2020 Jan 10	2020 Jan 11	3 818
6x	49	2020 Jan 11	2020 Jan 12	2 400
7x	33	2020 Jan 16	2020 Jan 16	1 666
8	112	2020 Jan 11	2020 Feb 1	5 097
9	112	2020 Jan 12	2020 Feb 2	5 097
10x	13	2020 Jan 17	2020 Feb 1	803
11x	11	2020 Jan 18	2020 Feb 2	695
12	112	2020 Jun 19	2020 Jun 21	5 100
13	104	2020 Aug 28	2020 Aug 30	4 884
14*	90	2020 Dec 24	2021 Aug 1	2 554
15x	1	2021 Apr 1	2021 Apr 1	66
16x*	2	2021 Apr 2	2021 Apr 2	67
17	113	2021 Jul 21	2021 Jul 24	5 515
18*	91	2021 Jul 28	2021 Aug 1	2 797
19	113	2021 Aug 20	2021 Aug 24	5 122
20*	91	2021 Sep 20	2021 Sep 25	2 604
21*	91	2021 Nov 18	2021 Nov 22	2 604

† n.b. the sky area for the reference epoch 0 differs from that presented in Murphy et al. (2021) as our work here uses the subsequently publicly released images that were masked with a higher noise threshold

3.2.1 VAST Pilot Survey Observations

Table 3.1 gives a detailed summary of the VAST-P observations across both Phase 1 and 2. VAST-P1 consisted of 13 epochs (six full and seven partial[2]) in addition to a reference epoch (0) conducted as part of the low-band Rapid ASKAP Continuum Survey (RACS-low; McConnell et al., 2020). Each field was observed at the 888 MHz low-band central frequency with an integration time of 12 min (with the exception of epoch 0 with 15 min integration time) and total bandwidth of 288 MHz, giving a typical rms sensitivity of 0.24 mJy beam^{-1}. The full footprint of VAST-P1 covers ∼5 100 deg^2 across 113 fields. For details on the RACS data calibration and reduction pipeline, refer to McConnell et al. (2020); Hale et al. (2021) for the RACS source catalogue and properties; and Murphy et al. (2021) for VAST-P data products and observing strategy.

VAST-P2 consisted of five full epochs (17-21), of which three were observed at the mid-band and the other two were at the low-band. Preceding the full epochs were two quality-gate epochs (15x and 16x) conducted as a test prior to the planned set of VAST-P2 observations and a reference epoch (14) for the mid-band conducted as part of the mid-band Rapid ASKAP Continuum Survey (RACS-mid; Duchesne et al., 2023). The low-band observations followed the same observational parameters as in VAST-P1, while the mid-band observations used a smaller footprint and were centred on a central frequency of 1 296 MHz with 12 min integration time per field (with the exception of epoch 14, which had a 15 min integration time). However, since the lower 144 MHz of the band is flagged due to radio frequency interference, the resulting images have a central frequency of 1 397 MHz and a bandwidth of 144 MHz. The full footprint of VAST-P2 mid-band covers ∼2 600 deg^2 across 91 fields. Please refer to the references above and references therein for details relating to the data processing and resulting data products for VAST-P2 as they use a similar data reduction pipeline to that used for VAST-P1.

Table 3.2: Summary of the astrometric accuracy and flux-density scale of the VAST-P dataset used in this work. Columns 1 through 4 show the survey observing band, median right ascension and declination offsets for VAST-P sources with respect to ICRF sources, and the flux-density ratio of VAST-P sources compared against sources in the reference RACS-low catalogue. We assumed a spectral scaling of $\alpha = -0.8$ to evaluate the flux-density ratio for mid-band data against the reference RACS-low catalogue.

VAST-P Band	RA Offset (arcsec)	Dec Offset (arcsec)	$S_{\mathrm{VAST\text{-}P}}/S_{\mathrm{RACS}}$
Low (888 MHz)	$+0.58 \pm 0.51$	-0.32 ± 0.55	1.04 ± 0.17
Mid (1 397 MHz)	$+0.28 \pm 0.88$	-0.33 ± 0.49	0.96 ± 0.28

Following the procedures in Murphy et al. (2021), we evaluated the astrometric

[2]Epochs with partial coverage contain fields from extra test observations and from duplicate observations arising from problems in the scheduling of the full epochs.

accuracy and flux-density scale of our dataset[3]; we provide a summary in Table 3.2. The VAST-P sources in the low-band data had an astrometric offset with respect to the positions of associated sources in the International Celestial Reference Frame (ICRF; Charlot et al., 2020) catalogue of $0\farcs58 \pm 0\farcs51$ in right ascension and $-0\farcs32 \pm 0\farcs55$ in declination, with a standard error of $0\farcs01$ in both coordinates (the standard error on the *median* offset is given by $1.253 \times \sigma_{\rm rms}/\sqrt{N}$, where $\sigma_{\rm rms}$ is the rms spread of the measured offsets and N is the total source count; e.g., Maindonald & Braun 2006). For the mid-band data, this was $0\farcs28 \pm 0\farcs88$ in right ascension and $-0\farcs33 \pm 0\farcs49$ in declination, with a standard error of $0\farcs05$ in both coordinates. The overall median VAST-P / RACS-low flux-density ratio for the low-band data was 1.04 ± 0.17, with all 16 epochs having a median flux-density ratio within 5 per cent of the overall median. For the mid-band data, this was 0.96 ± 0.28, with all 5 epochs having a median flux-density ratio within 1 per cent of the overall median. While RACS-low is at a lower frequency than the mid-band data, it was still used as the reference catalogue as its flux-density scale is well characterised in McConnell et al. (2020) and covers the entirety of the VAST-P mid-band footprint. We corrected for the frequency difference in our flux-density ratio calculations by scaling with an assumed spectral index α of -0.8 (Condon, 1992), defined as $S_\nu \propto \nu^\alpha$. The median astrometric offsets, each smaller than the size of an image pixel, were sufficient for robust cross-epoch source association for light-curve extraction, while the flux-density scale, consistent with all other epochs to within 5 per cent, was sufficient for the use of functional fits for our search method.

For our light-curve extraction and subsequent search for orphan afterglows, we used the low-band data (17 of the 22 epochs) only to minimise uncertainties associated with spectral scaling. We used the mid-band data only in the follow-up process to provide supplementary spectral information for characterising candidates in Section 3.4. This gives our search a temporal baseline of 28 months, spanning 2019 April 25 to 2021 August 24, with sampling cadences ranging from 1 day to 8 months.

3.2.2 VAST Pipeline Data Analysis

The VAST pipeline takes input images and source catalogues to produce light curves for every source that had a detection in one or more epochs. Sources were associated between epochs using the de Ruiter radius, which is a quantity representing the angular separation between two sources normalised by their positional errors (de Ruiter et al., 1977; Scheers, 2011), expressed as:

$$r_{ij} = \sqrt{\frac{(\Delta\alpha_{ij}\cos\bar{\delta}_{ij})^2}{\sigma^2_{\alpha,i} + \sigma^2_{\alpha,j}} + \frac{(\Delta\delta_{ij})^2}{\sigma^2_{\delta,i} + \sigma^2_{\delta,j}}}, \tag{3.1}$$

where $\Delta\alpha(\delta)_{ij}$ is the positional offset in right ascension (declination) between sources i and j, $\bar{\delta}_{ij}$ is the mean declination of sources i and j, and $\sigma_{\alpha(\delta),i}$ is the 1σ positional

[3] The only difference in procedure was the definition of compactness used for the mid-band data, which was defined in this work as $0.8 < S_I/S_P < 1.2$, since the fitted 'envelope' function from Hale et al. (2021) for characterising whether a source was unresolved is only applicable to low-band ASKAP data.

uncertainty for source i in right ascension (declination). The resulting light curves after source association consisted of flux-density measurements from source catalogues produced using SELAVY (Whiting & Humphreys, 2012) for detections and forced extractions[4] for non-detections. The pipeline performed these forced extractions for each source in every epoch where there was a non-detection to build a complete light curve. From these light curves, the pipeline calculated key variability metrics for each source – the modulation index, V; and the reduced χ^2 relative to a constant model, η (see also Swinbank et al., 2015; Rowlinson et al., 2019). They measure the degree and significance of variability, respectively, and are defined as:

$$V = \frac{1}{\overline{S}}\sqrt{\frac{N}{N-1}(\overline{S^2} - \overline{S}^2)}, \tag{3.2}$$

$$\eta = \frac{N}{N-1}\left(\overline{wS^2} - \frac{\overline{wS}^2}{\overline{w}}\right), \tag{3.3}$$

where N is the number of data points in the light curve, $\overline{S}$ is the mean flux density across all epochs, and $\overline{w}$ is the mean of the measurement weights across all epochs, defined as $w_i = 1/\sigma_i^2$ with σ_i the measurement uncertainty at the i-th epoch. For more details on the VAST pipeline, please refer to Pintaldi et al. (2022).

Our pipeline run ingested all the low-band epochs of VAST-P (i.e., epochs 1-13, 15x, 17, 19). The pipeline run settings followed those described in Murphy et al. (2021), with the de Ruiter association radius being the key setting that controlled the source association and light-curve building process for this work. We set the de Ruiter association radius parameter to 5.68, which effectively allows only 10^{-7} genuine associations to be missed[5] and, in practice, this would correspond to an angular association radius that is much smaller than the size of our beam. This pipeline run returned 1 068 985 unique sources. We then applied the following filters to the dataset, including only sources that meet the following criteria:

1. has at least four measurements (either forced or SELAVY) as required by our methods in Section 3.3;
2. is compact as defined in Hale et al. (2021) by the integrated-to-peak flux-density ratio: $S_I/S_P < 1.025 + 0.69 \times \mathrm{SNR}^{-0.62}$;
3. is isolated with no neighbouring sources within a $< 1'$ separation radius to avoid source and sidelobe confusion;
4. has a minimum SNR of 10 for sources with one detection to minimise false detections (we relaxed this requirement for sources with more than one detection, requiring a lower minimum SNR of 7.5) – see Metzger et al. (2015) for a brief discussion;

[4] The flux density was measured at a specified location using the raw image, rms and background maps with the following package:
https://github.com/askap-vast/forced_phot

[5] This is based on the properties of the Rayleigh distribution. The de Ruiter positional differences between genuinely associated sources will follow this distribution (for details, see de Ruiter et al., 1977).

5. has a median image rms $< 0.8\,\mathrm{mJy\,beam^{-1}}$ to avoid regions of high noise, e.g., at the footprint edge;
6. has a positive modulation index V, excluding negative flux-density artefacts caused by bright sources.

After applying these filters, our sample included 130 406 unique sources with at least one detection in a low-band VAST-P epoch. A standard search for variables and transients could be performed at this point by identifying sources with large V and η values exceeding a certain threshold (e.g., similar to Murphy et al., 2021). However, as this method is prone to missing slow transients (discussed in more detail in Section 3.5), we developed a more suitable method for our search for orphan afterglows.

3.3 Orphan Afterglow Search

In our search, we identified sources from our sample which had light curves featuring power-law rises and/or decays; these are characteristic of GRB afterglows, and more generally, extragalactic synchrotron transients (e.g., Sari et al., 1998). For each unique source in our sample, we defined its *event duration* to range from the time of the first detection until the time of the first subsequent non-detection, where a detection was defined as a measurement with a SNR ≥ 2. In the case where the last measurement was also a detection, we instead counted until the time of the last detection. We justify that we have improved our confidence in our low-signal detections (those with SNR from 2 to 7.5) by ensuring that these are spatially associated with at least two $> 7.5\sigma$ detections and/or at least one $> 10\sigma$ detection from other epochs (as discussed previously in Subsection 3.2.2). We conducted our search by performing a functional fit to all measurements within the event duration for every unique source in our sample, where the functional form depended on the number of observations n taken within the event duration and the location of the highest flux-density measurement, i.e., the *peak measurement*.

For sources with $n \geq 6$ and a peak measurement not located as the first or last measurement in the event duration, we fitted a SBPL model:

$$S_t = S_{\mathrm{peak}} \left[\left(\frac{t - \Delta t}{t_{\mathrm{peak}}} \right)^{-s\delta_1} + \left(\frac{t - \Delta t}{t_{\mathrm{peak}}} \right)^{-s\delta_2} \right]^{-1/s}, \tag{3.4}$$

where t is the time after the first measurement (epoch 0), S_t is the flux density as a function of time t, Δt is the time elapsed between the time of the first measurement (epoch 0) and the time of the GRB explosion (or transient event), δ_1 is the asymptotic rise slope, δ_2 is the asymptotic decay slope, S_{peak} and t_{peak} are the approximate flux density and time post-burst of the light-curve peak, and s is the smoothness parameter. Since the light curve is often sampled at > 1 month cadence, we chose to reduce the number of measurements required for a fit by reducing the number of free parameters in this model to increase the sensitivity of our search to transients evolving on the timescale of a few months. We did this by fixing s to the fiducial value of 5 and did not consider additional breaks in our functional form, which may more aptly describe GRBs with observed jet breaks (Rhoads, 1999; Sari et al., 1999) and those exploding in a stellar-wind environment (Chevalier & Li, 2000).

For the scenarios where (a) the source has $n \geq 4$ and a peak measurement located as either the first or last measurement in the event duration, or (b) the source has $n = 5$ and a peak measurement that is not the middle measurement, we fitted a simple PL model:

$$S_t = A(t - \Delta t)^{\beta}, \tag{3.5}$$

where β is the temporal slope (positive for rise and negative for decay), A is a normalisation constant, and t, S_t, Δt are defined as in Equation 3.4 above. In scenario (b) where not enough data points were available to fit a SBPL, we fitted the simple PL only to observations on the side of the peak measurement with the most data points.

We performed these functional fits using the non-linear least-squares optimisation routine in the SciPy (Virtanen et al., 2020) Python library. We applied the following physically motivated constraints during the fitting process:

1. $0.8\,\max(S_t) < S_{\mathrm{peak}} < 3\,\max(S_t)$ – this constraint helps to exclude sources with erroneous fits of the SBPL peak, especially in cases where the light curve around the peak is undersampled, where as a result it becomes difficult to characterise the true properties of the underlying light curve;

2. $10\,\mathrm{d} < t_{\mathrm{peak}} < 1\,000\,\mathrm{d}$ – afterglows typically peak at ∼100+ days post-burst at gigahertz frequency and the constraints used here are consistent with known radio-afterglow light curves at this frequency (e.g., Chandra & Frail, 2012; Maity & Chandra, 2021);

3. $-30\,\mathrm{yr} < \Delta t < \min(t)$ – this constraint allows the search to be sensitive to bursts occurring up to 30 yr ago, accounting for the possibility of detecting decade-long transients, such as FIRST J141918.9+394036 (Law et al., 2018);

4. $0.2 < \delta_1 < 10$, $-5 < \delta_2 < -0.3$, and $-5 < \beta < 10$ – numerous analytical and numerical efforts (e.g., Granot & Sari, 2002; van Eerten & MacFadyen, 2011; Granot et al., 2018a,b; Lamb et al., 2021) have attempted to model radio light curves of afterglows seen off-axis. Their findings show the rise and decay behaviours differ substantially from the standard on-axis GRB afterglow (e.g., Sari et al., 1998) due to complex interplay of jet dynamics with viewing angle effects; the typical rise and decay slopes varied based on a range of factors including but not limited to the viewing angle, microphysics (e.g., stratification parameter), and assumptions about the jet geometry (e.g., top-hat, Gaussian, etc.). Our constraints on these slopes allow our search to be sensitive to the most extreme temporal indices predicted.

To measure how well the light curves were described by these functional fits, we calculated their corresponding χ^2-statistic:

$$\chi^2 = \sum_{i=1}^{n} \left(\frac{S_i - \widehat{S}_i}{\sigma_i} \right)^2, \tag{3.6}$$

where S_i, σ_i and $\widehat{S_i}$ are the measured flux density, the 1σ uncertainty on the measurement, and the model-fitted flux density at the i-th epoch of the n-epoch light curve, respectively. This quantity is distributed according to the χ^2-distribution with $n-p$ degrees of freedom, where n is the number of measurements in the light curve and p is the number of free parameters in the functional fit.

Aside from fitting each unique source in the sample to (SB)PL models, we also compared these fits against a constant benchmark model S_t = constant, for which we also calculated the χ^2 statistic. Persistent sources that are not varying, as well as other variable and/or transient phenomena that exhibit oscillatory, burst- or pulse-like light curves, such as AGN scintillation or flaring radio stars, would be better described by this benchmark model than the (SB)PL functions. Given the benchmark model is 'nested' within the (SB)PL models, we determined which light curves were *significantly* better described by (SB)PL models than the benchmark by calculating the F-statistic (e.g., Weisberg, 2005):

$$F = \frac{\chi^2_{\rm b} - \chi^2_{\rm m}}{p_{\rm m} - p_{\rm b}} \Big/ \frac{\chi^2_{\rm m}}{n - p_{\rm m}} = \left(\frac{\chi^2_{\rm b}}{\chi^2_{\rm m}} - 1\right) \Big/ \left(\frac{p_{\rm m} - p_{\rm b}}{n - p_{\rm m}}\right), \tag{3.7}$$

where χ^2 is calculated from Equation 3.6, p is the number of model free parameters, n is the number of measurements, and the subscript m refers to the (SB)PL models and the subscript b refers to the benchmark model. This quantity is distributed according to the F-distribution with $(p_{\rm m}–p_{\rm b}, n–p_{\rm m})$ degrees of freedom.

Having fit all the light curves and calculated the χ^2-, F-statistics, we discarded sources from our sample which had:

1. p-value$(\chi^2_{\rm m}) < 0.05$ significance level – the (SB)PL models do not fit the light curve *significantly* well;

2. p-value$(F) > 0.05$ significance level – the (SB)PL models do not fit the light curve *significantly* better than the benchmark model;

3. fitted parameters with values at the constraint boundaries, e.g., $\widehat{\delta_1} \approx 10$ – the optimisation algorithm suggests the light curve would be better fit with unphysical parameter values;

4. $|\beta| < 0.3$ – the slow rise or decay is consistent with a flat, non-varying light curve;

5. $\beta > 0$ and $\Delta t < -500$ days – the light curve has not turned over despite bursting more than 500 days prior. Turnovers occurring later than 500 days post-burst at gigahertz frequency have not been observed in large radio-afterglow samples (e.g., Chandra & Frail, 2012, but also see Ghirlanda et al. 2014).

After applying these cuts based on the functional fits, 193 (109 and 84 from the SBPL and PL fits, respectively) candidates remained in our sample. Beyond using our model-fitting methodology, we used additional radio and multi-wavelength data[6] as detailed below to further narrow down our candidate list. The candidate cuts we made include sources with:

1. Detections in archival radio surveys, indicating that they are persistent sources or variable sources. The exception is for sources fitted with a negative decay slope $\beta < 0$ using a PL model, in which case, the time elapsed between the burst and the first detection ($-\Delta t$) was also checked. The archival radio surveys we had cross-correlated with included the NRAO VLA Sky Survey (NVSS; Condon et al., 1998), Sydney University Molonglo Sky Survey (SUMSS; Mauch et al., 2003), Australia Telescope 20 GHz survey (AT20G; Murphy et al., 2010), GaLactic and Extragalactic All-sky Murchison Widefield Array survey (GLEAM; Hurley-Walker et al., 2017), and TIFR GMRT Sky Survey (TGSS; Intema et al., 2017). This archival data ruled out another 85 candidates (54 SBPL, 31 PL).

2. Spectral or temporal information from supplementary radio data that was inconsistent with the expected behaviour of afterglows and synchrotron transients. We used supplementary data from VLASS, mid-band data from VAST-P2 and publicly available archival ASKAP data from the CSIRO ASKAP Science Data Archive (CASDA; Chapman et al., 2017; Huynh et al., 2020, see Data Availability statement for more detail). A typical example of this involves a light curve exhibiting a power-law decline at a lower frequency, yet is rising at a higher frequency at a later time. We used supplementary data to rule out a further 43 candidates (26 SBPL, 17 PL).

3. Spatially consistent (i.e., not offset from nucleus) *Wide-field Infrared Survey Explorer* (*WISE*; Wright et al., 2010) counterparts, with infrared colours suggesting the source is likely a galaxy or an AGN. In particular, we relied on source classifications based on the [3.4 µm] − [4.6 µm] and [4.6 µm] − [12 µm] infrared colours, following the colour-colour classification system presented in Wright et al. (2010) (see Figure 3.1). Sources with infrared counterparts associated with AGNs were immediately ruled out since GRBs, with the exception of short GRB 150101B (Xie et al., 2016) and long GRB 191019A (interpreted to have been produced by the merger of a compact binary formed via dynamical interactions; Levan et al., 2023), are not known to be hosted by such systems. We made these cuts by using the AllWISE catalogue and its associated data products (Cutri et al., 2021). This data allowed us to rule out a further 40 candidates (13 SBPL, 27 PL).

[6] The association radius for sources detected in archival radio surveys and by the *Wide-field Infrared Survey Explorer* (*WISE*) was $5''$. This association radius factored in the typical astrometric uncertainties in our ASKAP data (see Table 3.2) in addition to the typical astrometric uncertainties of the archival/*WISE* data (see their respective papers for details), which was often worse due to a significantly larger point spread function. However, a smaller association radius of $3''$(still conservative, $\gtrsim 3\sigma_{\rm ASKAP}$) was used for crossmatches with the optical surveys since the astrometric uncertainties were dominated by the ASKAP data in this case.

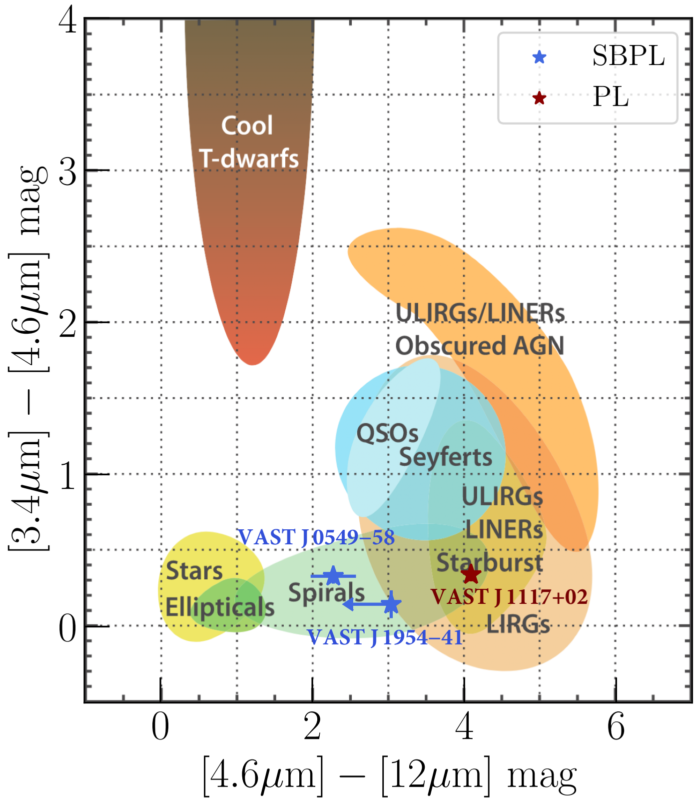

Figure 3.1: Orphan afterglow candidates obtained from our functional fits are overlaid on top of the *WISE* colour-colour classification regions described in Wright et al. (2010). Only candidates with a *WISE* counterpart are shown. Candidates that were obtained in the search with a SBPL fit are shown in blue, while those obtained with a PL fit are shown in red. We note that for VAST J195443.9−412511 an upper limit is given for the [4.6 µm] − [12 µm] colour due to a non-detection in the 12 µm band.

4. Other reasons indicating they were likely not afterglow related. These reasons included: data artefacts (e.g., incorrect dates extracted for the light curve or bright nearby sources affecting image quality), photometric redshifts derived from the Dark Energy Camera Legacy Survey (DECaLS; Dey et al., 2019; Zhou et al., 2021) with $z \gg 0.2$ (corresponding to the radio afterglow detectability threshold for VAST-P as shown in Leung et al., 2021a), inconsistent peak and integrated flux-density light curves for borderline extended sources (slightly below the compactness threshold), deviations from the power-law fits greater than that expected from scintillation[7] and noise errors, and prior classifications in the literature. These allowed us to rule out another 22 candidates (13 SBPL, 9 PL).

Even though some candidates could have been ruled out by multiple criteria above, our reported number of candidates ruled out by each criterion does not include those that were already eliminated by a previous criterion, i.e., this was a step-

[7]The scintillation model we used here is detailed later in Subsection 3.4.2. We excluded sources with a modulation index (after accounting for the variability that can be explained by the power-law fits) exceeding that predicted by the scintillation model by more than 10 per cent.

wise elimination process. Our remaining sample contained five orphan afterglow candidates (listed in Table 3.3); of these, three were found from a SBPL fit and two from a PL fit.

For each remaining candidate, we performed follow-up Australia Telescope Compact Array (ATCA) observations and present this in Subsection 3.4.1. In light of the new information obtained from these observations, we performed additional analysis to come to a final decision on whether each candidate is likely orphan afterglow related or can be explained by some other astrophysical phenomena. We mainly arrived at these decisions for each candidate by checking (a) whether the light curve continued to exhibit a power-law behaviour at the epoch of the new ATCA observations (if not, whether interstellar scintillation would instead be a better alternative for explaining the observed variability in the light curve), and (b) whether the spectral/temporal evolution of the candidate was consistent with known GRB closure relations (e.g., Granot & Sari, 2002) with a reasonable choice of microphysical parameters. These details are presented and more comprehensively explained in Subsection 3.4.2.

3.4 Results

3.4.1 Follow-up ATCA Observations

We observed each candidate with the ATCA in order to better characterise their spectral properties and evolution. We conducted observations for all candidates on 2022 May 16 UT under project C3363 (PI: T. Murphy): at central frequencies of 2.1, 5.5, and 9.0 GHz, each with 2 048 MHz bandwidth, and the array in 750D configuration. The 750D configuration consisted of 10 short baselines < 800 m and 5 long baselines $\sim$4 km. We also performed an additional epoch of observations for candidates VAST J195443.9−412511 and VAST J175036.1−181454. For VAST J195443.9−412511, we also observed on 2022 September 8, at central frequencies of 2.1, 5.5, and 9.0 GHz, each with 2 048 MHz bandwidth, and the array in 6D configuration (with a maximum baseline of 6 km). While for candidate VAST J175036.1−181454, we also observed on 2022 March 5, at central frequencies of 2.1, 5.5, 9.0, 16.7, and 21.2 GHz, each with 2 048 MHz bandwidth, and the array in 6A configuration (with a maximum baseline of 6 km). The observational and data reduction details are summarised in Table 3.3.

We reduced all the data using standard routines in Miriad (Sault et al., 1995). We used PKS 1934−638 to calibrate both the bandpass and the flux-density scale for all observations, with the exception of the 16.7/21.2 GHz observation for VAST J175036.1−181454, where we used PKS 1253−055 (3C 279) to calibrate the bandpass and PKS 1934−638 for the flux-density scale. The calibrators we used to correct for the time-variable complex gains for each target source are listed in Table 3.3. In the imaging process, we often flagged either the set of short or long baselines depending on the optimal (u, v)-coverage required for a reliable flux-density measurement. This decision depended on various factors that were considered in an observation-by-observation basis, including hour-angle coverage, source elevation,

Table 3.3: Table of follow-up ATCA observations for the five orphan afterglow candidates. Columns 1 through 6 show the candidate name, the right ascension and declination of the observation phase centre, the central frequency of the receiver, the gain calibrator used, and the baselines flagged in the imaging process. All observations, with the exception of two, were taken on 2022 May 16, in the 750D array configuration, using PKS 1934−638 for both bandpass and flux-scale calibration. The two exceptions are (a) VAST J195443.9−412511, which had an additional epoch of follow-up observations, taken on 2022 September 8 in the 6D array configuration; and (b) VAST J175036.1−181454, which had an additional epoch of follow-up observations, taken on 2022 March 5 in the 6A array configuration – for only the 16.7 GHz observation in this epoch, we used PKS 1253−055 (3C 279) to calibrate the bandpass and PKS 1934−638 for the flux-scale.

Source Name	RA (J2000)	Dec (J2000)	Receiver (GHz)	Gain Cal.	Flagged Baselines
VAST J195443.9−412511	19:54:44.0	−41:25:11.2	2.1	1954−388	CA01–CA02
			5.5	""	""
(22 May 16)			9.0	""	CA01–CA02, all long baselines including CA06
(22 Sep 8)			2.1	""	None
			5.5	""	""
			9.0	""	""
VAST J200430.5−401649	20:04:30.6	−40:16:49.9	2.1	1954−388	CA01–CA02
			5.5	""	""
			9.0	""	CA01–CA02, all long baselines including CA06
VAST J054958.0−581946	05:49:58.0	−58:19:46.4	2.1	0420−625	CA01–CA02
			5.5	0516−621	all short baselines not including CA06
			9.0	""	CA01–CA02, all long baselines including CA06
VAST J111757.5+021607	11:17:57.5	+02:16:07.3	2.1	1055+018	all (not imaged due to 1D (u, v) coverage)
			5.5	""	""
			9.0	""	""
VAST J175036.1−181454	17:50:36.1	−18:14:54.4	2.1	1730−130	None
			5.5	""	""
			9.0	""	""
			16.7	""	""
(22 Mar 5)			21.2	""	all (not imaged due to weather-related data issue)
(22 May 16)			2.1	""	all short baselines not including CA06
			5.5	""	CA01–CA02, all long baselines including CA06
			9.0	""	""

observing frequency, required sensitivity and the extent of confusion from neighbouring sources (and their sidelobes). We produced images using the multi-frequency synthesis CLEAN algorithm (Högbom, 1974; Clark, 1980; Sault & Wieringa, 1994), mostly with a robustness of 0, and report the flux-density measurements in Tables 3.6 and 3.7. The 2.1 to 9.0 GHz spectral index $\alpha_{2.1-9\,\mathrm{GHz}}$, obtained from an ordinary least-squares optimisation, is separately reported in Tables 3.4 and 3.5. We note that the data from the 21.2 GHz observation for VAST J175036.1−181454 was adversely affected by poor weather conditions, while the observations of VAST J111757.5+021607 were affected by the very 1D (u, v)-coverage that results for observations of sources near the celestial equator with a linear East-West array – as a result, no reliable measurements from these observations are reported here.

Table 3.4: The estimated temporal and spectral parameters for orphan afterglow candidates identified using a SBPL fit to the source light curve. Column 1 is the candidate source name, Columns 2-6 show the median values (and 1σ uncertainties) of the marginalised posterior distribution for each free parameter of the SBPL fit to the light curve attained from nested sampling, Column 7 is the spectral index from a least-squared fit to the ATCA measurements obtained on 2022 May 16.

Source Name	S_{peak}	$\log(\mathrm{t_{peak}})$	δ_1	δ_2	$\Delta t^{1/3}$	$\alpha_{2.1-9\,\mathrm{GHz}}$
VAST J195443.9−412511	$5.63^{+0.26}_{-0.26}$	$2.67^{+0.22}_{-0.25}$	$2.96^{+2.96}_{-1.88}$	$-0.47^{+0.12}_{-0.20}$	$-6.92^{+2.29}_{-1.71}$	-0.10 ± 0.02
VAST J200430.5−401649	$4.79^{+0.33}_{-0.30}$	$2.65^{+0.23}_{-0.25}$	$2.43^{+3.04}_{-1.58}$	$-0.61^{+0.20}_{-0.29}$	$-6.86^{+2.14}_{-1.74}$	-0.96 ± 0.05
VAST J054958.0−581946	$1.99^{+0.74}_{-0.28}$	$2.20^{+0.40}_{-0.51}$	$3.77^{+3.75}_{-2.46}$	$-0.47^{+0.12}_{-0.25}$	$-4.60^{+2.01}_{-2.29}$	-0.50 ± 0.01

Table 3.5: The estimated temporal and spectral parameters for orphan afterglow candidates identified using a PL fit to the source light curve, similar to Table 3.4. There is no fitted spectral index for VAST J111757.5+021607 as there were no reliable measurements from ATCA for this source.

Source Name	A	β	$\Delta t^{1/3}$	$\alpha_{2.1-9\,\mathrm{GHz}}$
VAST J111757.5+021607	$41.31^{+35.89}_{-26.80}$	$-0.38^{+0.12}_{-0.08}$	$-11.41^{+2.78}_{-4.28}$	—
VAST J175036.1−181454	$0.00^{+0.01}_{-0.00}$	$1.02^{+0.21}_{-0.21}$	$2.54^{+1.82}_{-1.30}$	-0.55 ± 0.08

3.4.2 Interpretation of Candidates

For each of our five candidates, we repeated our functional fits to Equations 3.4 and 3.5 to obtain more robust parameter (and error) estimates using the nested sampler Dynesty (Speagle, 2020) as implemented in the Bayesian inferences software Bilby (Ashton et al., 2019). We used the same physically motivated fit constraints from Section 3.3 with uniform priors, performing the nested sampling with 1 000 live points and a stopping criterion on the estimated evidence $\hat{\mathcal{Z}}$ of $\Delta\ln(\hat{\mathcal{Z}}) = 0.05$. The resulting parameter estimates are also reported in Tables 3.4 and 3.5, while the fitted light curves and radio spectra from ATCA observations are presented in Figures 3.2 and 3.3.

For each candidate, we also checked for counterparts in *WISE*, and where possible, obtained a classification from the infrared colours (using the same classification regions as described in Section 3.3, see Figure 3.1). We also compared the variability

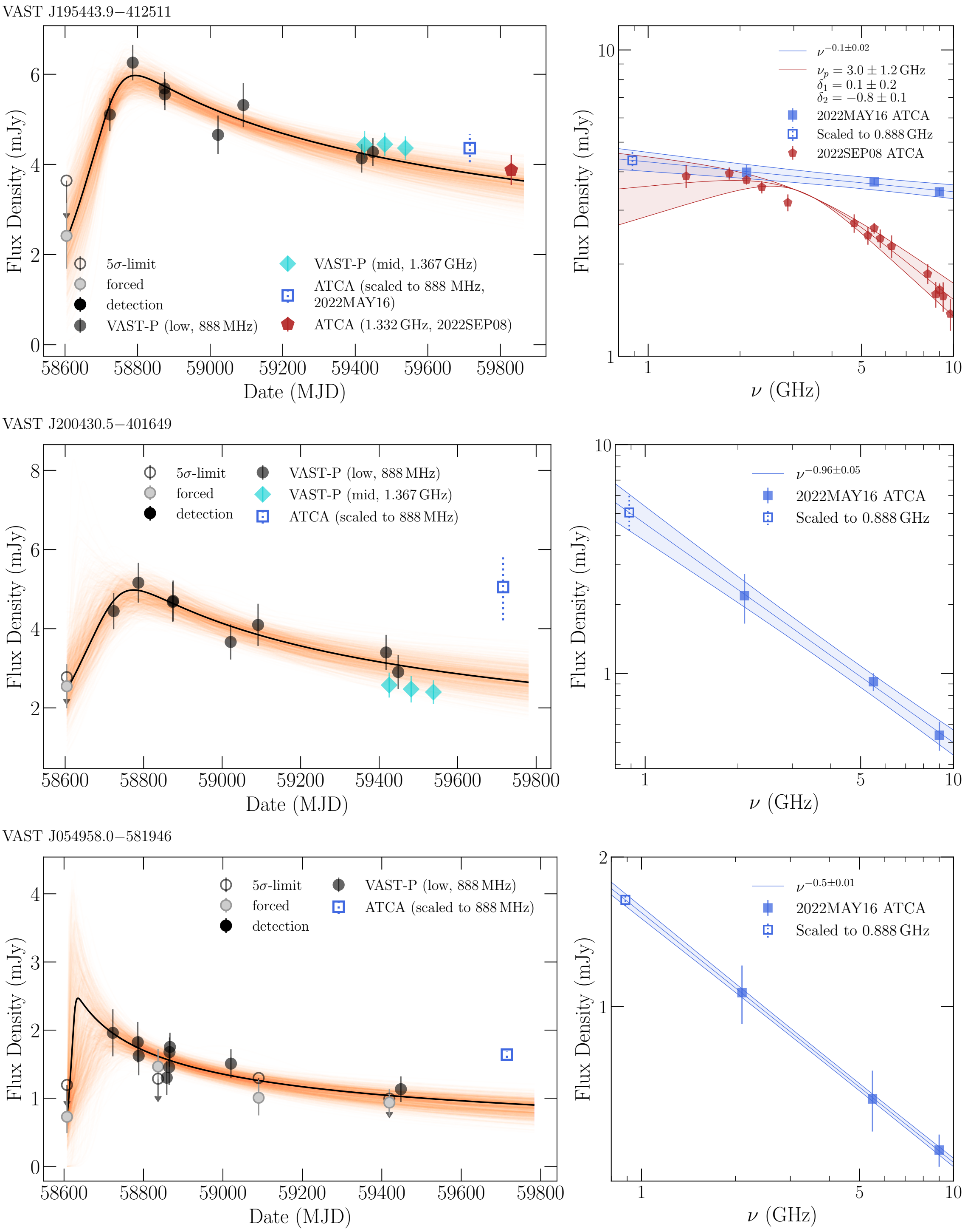

Figure 3.2: The radio light curves (*left*) and spectra (*right*) for each of the orphan afterglow candidates attained from a SBPL fit. For each light curve, only data from VAST-P and ATCA are shown; the full radio dataset for each source, including other complementary data from archival radio surveys, can be found in Tables 3.6 and 3.7. We represent the low-band (888 MHz) detections with black circular markers, and for the non-detections, we show both a measurement from forced extraction (grey circular markers) and also a 5σ limit (open circular markers). The mid-band (1.367 GHz) detections are shown with turquoise diamond markers (there are no mid-band non-detections). The ATCA flux density measurements *extrapolated* to 888 MHz from the 2022 May 16 observations are shown with blue, open, square markers. For VAST J195443.9−412511, we show an additional ATCA data point taken from the 2022 September 8 observations – this data point is represented by a red, filled, pentagonal marker and is from the 1.3 GHz sub-band measurement, not an extrapolation.

Figure 3.2 (*continued*): The black line is the fit to the light curve using parameters estimated from nested sampling (and overlaid are 1 000 random samples to illustrate the fit uncertainties). For each radio spectrum, we extrapolated the ATCA measurements from 2022 May 16 (blue, filled, square markers) to 888 MHz (blue, open, square markers) using a linear ordinary least-squares fit (blue line). For VAST J195443.9−412511, we show an additional radio spectral snapshot, using measurements taken from the 2022 September 8 ATCA observations (red pentagonal markers). For this 2022 September 8 radio spectrum, we fitted it with a smoothly broken power law (red line) with the estimated parameters for the peak frequency ν_p, rise slope δ_1, and decay slope δ_2 given in the legend.

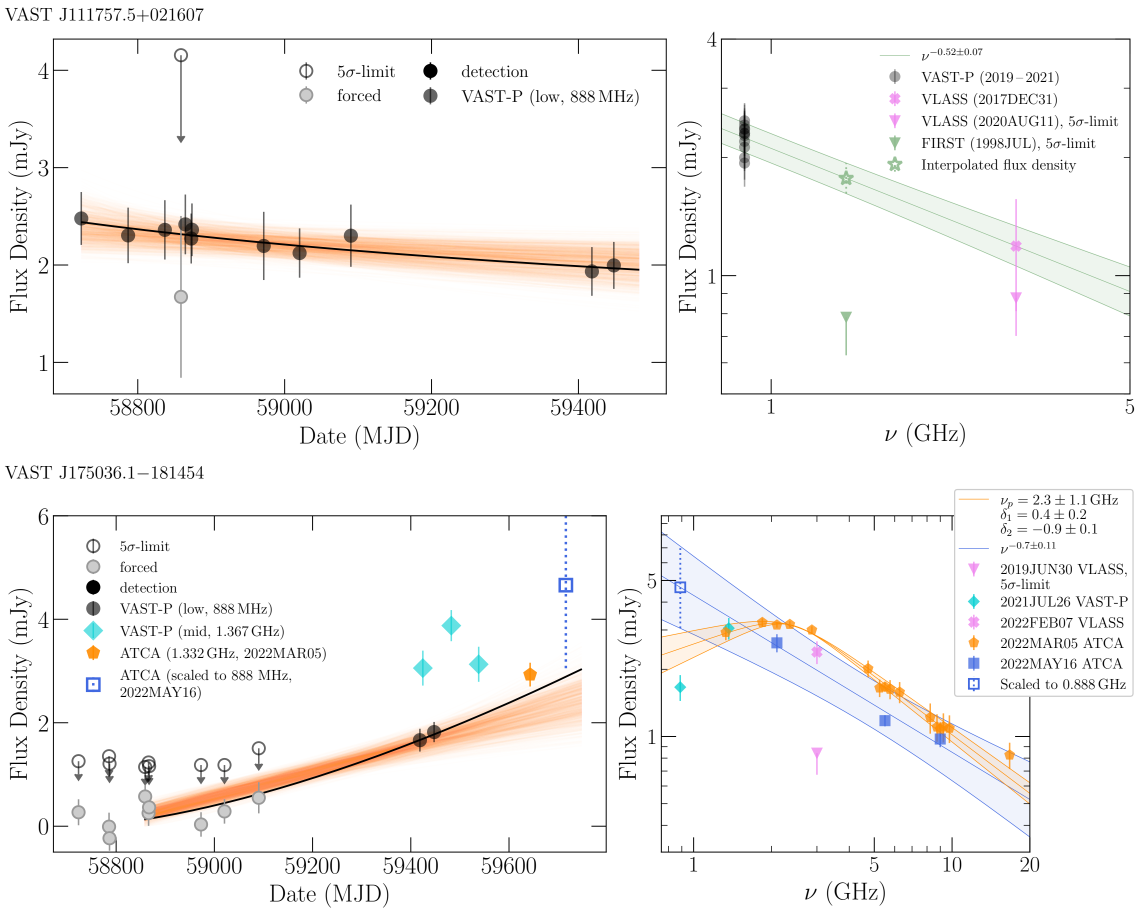

Figure 3.3: The radio light curves (*left*) and spectra (*right*) for each of the orphan afterglow candidates attained from a PL fit, similar to Figure 3.2. For VAST J111757.5+021607, the radio spectrum consists of archival measurements from VAST-P (black circular markers), FIRST (green inverted triangular marker, indicating a non-detection 5σ limit) and VLASS (pink square marker for detection and pink inverted triangular marker to indicate a non-detection 5σ limit), instead of ATCA measurements. The VAST-P and VLASS detections were *interpolated* to 1.4 GHz (green, open, star marker) using a linear ordinary least-squares fit (green line). For VAST J175036.1−181454, the ATCA data points in the light curve include a 1.3 GHz sub-band measurement from the 2022 March 5 observation (orange, filled, pentagonal marker) and a flux density measurement *extrapolated* to 888 MHz from the 2022 May 16 observations (blue, open, square marker). We show the radio spectral snapshots from both ATCA observations for this candidate – one from the 2022 March 5 epoch (orange pentagonal markers) and another from the 2022 May 16 epoch (blue square markers); we also show two VAST-P data points with turquoise diamond markers, and two VLASS data points with pink markers. The 2022 March 5 radio spectrum was fitted with a smoothly broken power law (orange line) with the estimated parameters for the peak frequency ν_p, rise slope δ_1, and decay slope δ_2 given in the legend. The 2022 May 16 radio spectrum was fitted by an ordinary least-squares fit (blue line), which was used for extrapolating the 2022 May 16 flux density measurements to 888 MHz (blue, open, square marker).

of each source to the expected extrinsic variability caused by refractive interstellar scintillation (RISS). This effect is caused by the propagation of radio waves through the ionised interstellar medium in our Galaxy, causing the wavefront to be distorted, leading to phase changes resulting in the observed variability. We used the NE2001 electron density model[8] (Cordes & Lazio, 2002) to estimate the Galactic contribution to the electron distribution along the line of sight to our sources. More specifically, the model outputs the transitional frequency ν_0, the characteristic frequency where the transition from the strong to weak scattering scintillation regimes occur, and we used this to calculate the modulation index due to RISS for each source by applying the equation presented in Walker (1998): $V = (\nu/\nu_0)^{17/30}$, where ν is the observing frequency. In the scenario where the source size $\theta_{\rm S}$ exceeds the angular broadening diameter $\theta_{\rm d}$ (which is dependent on the observing frequency and line of sight scattering measure), the modulation index (and degree of scintillation) would be reduced by a factor of $(\theta_{\rm d}/\theta_{\rm S})^{7/6}$. We used this RISS variability analysis together with the light curves, radio spectra, and *WISE* colour classifications to analyse each source.

VAST J195443.9−412511

VAST J195443.9−412511 was selected as a candidate via fitting to a SBPL; the fitted light curve (Figure 3.2, *upper-left panel*) rises with a slope of $2.96^{+2.96}_{-1.88}$ and decays with a slope of $-0.47^{+0.12}_{-0.20}$. Our follow-up ATCA observations on 2022 May 16 show a flat spectrum extending across the 2.1 to 9 GHz frequency range (see Figure 3.2, *upper-right panel*), with a spectral index of $\alpha_{2.1-9\,\rm GHz} = -0.10 \pm 0.02$. This spectral index is more shallow than any possible spectral segment expected for afterglow emission and cannot be explained by the expected curvature of the respective spectral breaks (e.g., Granot & Sari, 2002) so we rule out the possibility that this source is afterglow related. We obtained better spectral resolution in a subsequent epoch of ATCA observations taken on 2022 September 8 by splitting each observing band into four sub-bands, each with a bandwidth of 512 MHz, prior to imaging (see Table 3.6). These observations revealed a steepening of the spectrum, particularly at higher frequencies, and the presence of spectral curvature; a fit of this radio spectrum to a SBPL located a spectral turnover at $\nu = 3.0 \pm 1.2$ GHz with a rise and decay index of $\delta_1 = 0.1 \pm 0.2$ and $\delta_2 = -0.8 \pm 0.1$, respectively.

The flat radio spectrum observed in the first epoch of ATCA observations likely indicates the presence of a compact emitting region in a radio galaxy or an AGN jet aligned with our line of sight (i.e., a blazar; Urry & Padovani, 1995). The variability from the compact emitting region could either be intrinsic or extrinsic to the source. In the intrinsic scenario, we used light-crossing time arguments to constrain the size of the emitting region r to $r < \tau c = 0.16$ pc, where c is the speed of light and τ is the timescale of variability, estimated as the time between the minimum and maximum flux measurement in our light curve (Figure 3.2, *upper-left panel*). While this limit is broadly consistent with the inferred size of jets emanating from supermassive black holes detailed in the literature (e.g., Ighina et al., 2022), this upper-limit estimate

[8]We used the model via a python wrapper implemented in the package: https://pypi.org/project/pyne2001/

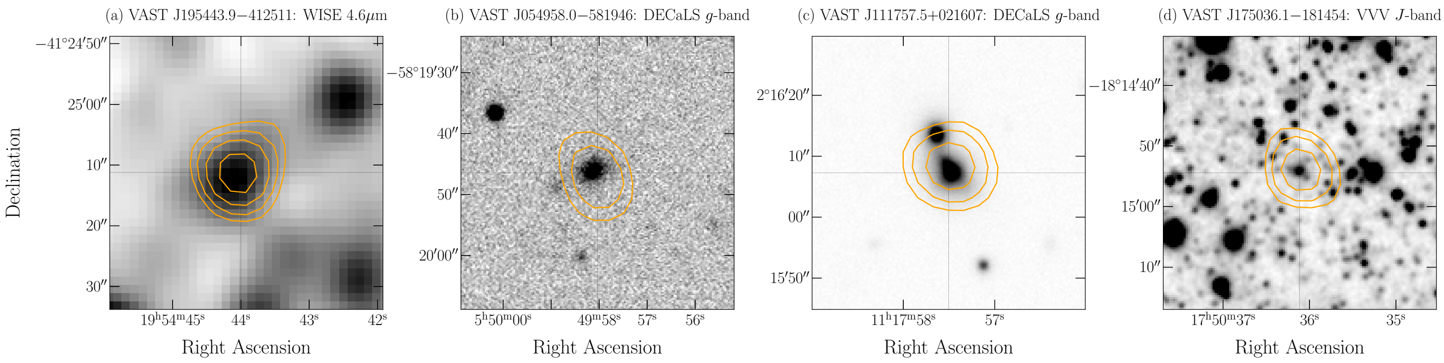

Figure 3.4: Images of multi-wavelength counterparts to the orphan afterglow candidates. Only candidates with a multi-wavelength counterpart are shown, with the image for each candidate selected from the highest resolution multi-wavelength survey available where a counterpart is detected. Presented from left to right are images of VAST J195443.9−412511 from the Wide-field Infrared Survey Explorer (WISE), VAST J054958.0−581946 from the Dark Energy Camera Legacy Survey (DECaLS), VAST J111757.5+021607 from DECaLS and VAST J175036.1−181454 from the VISTA Variables in the Via Lactea Survey (VVV). Overlaid are radio contours from the epoch of VAST with the highest signal-to-noise detection. The radio contours increase by a factor of $\sqrt{2}$ at each step, with the lowest contour starting at the 3σ level. Each image is $45'' \times 45''$, centred on the weighted average radio position across the VAST epochs, with North up and East to the left.

does not factor in the possibility that variability could travel quicker than the light-crossing time in the scenario of relativistic boosting and apparent superluminal motion. Alternatively, if the variability is attributed to extrinsic RISS, the observed modulation index is consistent with the expected modulation index from RISS; i.e., we can also put an angular constraint on the emission region to be smaller than the angular broadening diameter in the source's line of sight $\theta_{\rm d} = 1.4\,{\rm mas}$. Although the rapid rise and prolonged decay could be produced by a scattering screen with somewhat constrained properties, we feel that the intrinsic scenario is more likely to be correct.

The observed properties of VAST J195443.9−412511 – the rapid rise in the light curve and prolonged decay, the flat-to-steep radio spectrum transition, the high-to-low frequency evolution, and the evolution timescale of the source on the order of months – are similar to those observed in quasar 3C273 flares (e.g., Robson et al., 1983). The observed properties of such flares have been explained by models invoking relativistic shocks originating from disturbances in the outflow of an adiabatic, conical jet (e.g. Marscher & Gear, 1985; O'Dell, 1988). One caveat to this interpretation is the detection of a *WISE* counterpart (see Figure 3.4, *panel a*); although the non-detection in the 12 μm band prevents a conclusive source classification from using only *WISE* colours ($[3.4\,\mu{\rm m}] - [4.6\,\mu{\rm m}] = 0.15 \pm 0.09\,{\rm mag}$ and $[4.6\,\mu{\rm m}] - [12\,\mu{\rm m}] < 3.04\,{\rm mag}$), the colours provide sufficient constraints to disfavour an AGN origin (see Figure 3.1). Alternatively, for interpreting the observed properties of VAST J195443.9−412511, we have also considered the possibilities of a jet quenching in X–ray binaries (e.g., Russell et al., 2020) and radio flares from TDEs (e.g., Horesh et al., 2021). However, we rule out these since the former is expected to evolve on timescales much shorter on the order of hours and days (even though it can explain the flat-to-steep radio spectrum transition), while the latter struggles to explain the initially observed flat spectrum (even though it can explain the light-curve evolution). While we currently consider the AGN flare to be the leading interpretation, a definitive source classification would require spectroscopic follow-up and a comprehensive characterisation would benefit from continued multi-frequency monitoring to trace the evolution of the source's radio spectra as well as VLBI follow-up to constrain the source size.

VAST J200430.5−401649

VAST J200430.5−401649 was selected as a candidate via fitting to a SBPL; the fitted light curve (Figure 3.2, *middle-left panel*) rises with a slope of $2.43^{+3.04}_{-1.58}$ and decays with a slope of $-0.61^{+0.20}_{-0.29}$. The source was not detected in archival radio surveys and has no known counterparts in any multi-wavelength survey. ATCA follow-up revealed that it had a spectral index of $\alpha_{2.1-9\,\mathrm{GHz}} = -0.96 \pm 0.02$, consistent with the spectral index of $\alpha \sim -1$ inferred from the low-band epoch 17 and mid-band epoch 18 measurements taken one week apart. By extrapolating the radio spectrum from the ATCA observations (Figure 3.2, *middle-right panel*), the scaled flux density at 888 MHz on 2022 May 16 is 5.1 ± 0.9 mJy. This is a significant deviation away from the temporal power-law decay expected from an orphan afterglow (see Figure 3.2, *middle-left panel*); we therefore disfavour an afterglow interpretation for this variable source. The source has a modulation index of $V = 0.22$ (calculated from the low-band VAST-P data points), consistent with the expected variability from RISS along this line of sight.

In the analysis above where we disfavour the afterglow scenario, we note that extending the single power-law component from the ATCA frequencies to 888 MHz requires us to assume the absence of a spectral break at and around these frequencies. This assumption is at odds with the radio spectra of VAST J195443.9−412511 and VAST J111757.5+021607 in Figures 3.2 and 3.3, respectively; these plots instead show that the extrapolations have a tendency to lead to an overprediction due to the possible presence of spectral curvature. Despite this, we reason below that for the sole purpose of disfavouring the afterglow scenario, where we can use the fireball model to describe the location of the spectral turnover, it is valid to assume the absence of a spectral break for this extrapolation (and this analysis). This is a reasonable assumption because the injection break ν_m is expected to be $\ll$ 888 MHz at the epoch of our ATCA observation based on an estimation using *conservative* afterglow parameters in the following relation described in Panaitescu & Kumar (2000):

$$\nu_\mathrm{m} = 1.9 \times 10^{13}\, E_{\mathrm{iso,kin},53}^{1/2}\, \epsilon_{\mathrm{e},-1}^{2}\, \epsilon_{\mathrm{B},-2}^{1/2}\, T_\mathrm{d}^{-3/2}\, (1+z)^{1/2}\, \mathrm{Hz}, \tag{3.8}$$

where $E_\mathrm{iso,kin} = 10^{53} E_{\mathrm{iso,kin},53}$ erg is the total isotropic equivalent kinetic energy of the blast wave, $\epsilon_\mathrm{e} = 0.1\epsilon_{\mathrm{e},-1}$ and $\epsilon_\mathrm{B} = 0.01\epsilon_{\mathrm{B},-2}$ are the fractional shock energies in the accelerated electrons and magnetic fields, respectively, z is the redshift to the source, and T_d is the number of days elapsed since the burst event. In particular, this equation assumes a uniform jet, a wind environment[9], no additional energy injections, and an electron spectral index $p = 2.5$, with the conservative input parameters we used taking values within a physically reasonable range that maximise ν_m. Specifically, the input parameters we used were:

- $E_\mathrm{iso,kin} = 10^{54}$ erg – most bursts have $E_\mathrm{iso,kin} \sim 10^{53}$ erg, but the GRBs at the energetic end of the distribution will have $E_\mathrm{iso,kin}$ values an order of magnitude higher (e.g., Panaitescu & Kumar, 2001; Cenko et al., 2011);
- $\epsilon_\mathrm{e} = 0.1$ – the distribution of ϵ_e is narrowly around ~0.1 (e.g., Beniamini & van der Horst, 2017);
- $\epsilon_\mathrm{B} = 10^{-5}$ – a systematic study of magnetic fields in GRB shocks showed that in a wind environment the range for this parameter is from 10^{-7} to 10^{-5} (Santana et al., 2014);
- $T_\mathrm{d} = 1\,100$ days – this chosen value corresponds to the time between the epoch of the first ASKAP detection and the epoch of the ATCA observations, for which we are performing the extrapolation, i.e., the minimum possible onset time for the GRB event; and
- $z = 0.2$ – the limiting redshift which we expect an afterglow to be detectable in our surveys.

These conservative input parameters predicts the location of the injection frequency at the time of the ATCA observations to be $\lessapprox 200$ MHz. However, owing to the significant uncertainty in the range of values ϵ_B can take (spanning many orders of magnitude in the literature), we only disfavour rather than completely rule out an afterglow origin when considering candidates using this method. VAST J054958.0−581946 was the only other source where we applied this method (with the same set of assumptions and reasoning) to disfavour the afterglow scenario.

VAST J054958.0−581946

VAST J054958.0−581946 was selected as a candidate via fitting to a SBPL; the fitted light curve (Figure 3.2, *lower-left panel*) rises with a slope of $3.77^{+3.75}_{-2.46}$ and decays with a slope of $-0.47^{+0.12}_{-0.25}$. The source is associated with both *WISE* and DECaLS counterparts (see Figure 3.4, *panel b*); the *WISE* colours ($[3.4\,\mu\mathrm{m}] - [4.6\,\mu\mathrm{m}] = 0.33 \pm 0.05$ mag and $[4.6\,\mu\mathrm{m}] - [12\,\mu\mathrm{m}] = 2.28 \pm 0.30$ mag) suggest the source is associated with a spiral galaxy at a photometric redshift (as determined by DECaLS) of $z_\mathrm{photo} = 0.218$. ATCA follow-up revealed that it had a spectral index of $\alpha_{2.1-9\,\mathrm{GHz}} = -0.50 \pm 0.01$. By extrapolating the radio spectrum from the ATCA observations (Figure 3.2, *lower-right panel*), the scaled flux density at 888 MHz on 2022 May 16 is 1.64 ± 0.05 mJy. This is a significant deviation away from the temporal power-law decay expected from an orphan afterglow (see Figure 3.2, *lower-left panel*); we therefore disfavour the possibility the radio emission is afterglow related (following a similar argument to VAST J200430.5−401649) and propose it is most likely associated with the spiral galaxy. The source has a modulation index of $V = 0.26$ (calculated

[9]We selected the equation in Panaitescu & Kumar (2000) that described a wind environment since this was the more conservative option, producing a ν_m value that was a factor of ~2 higher than that in a homogeneous interstellar medium environment.

from low-band VAST-P data points), consistent with the expected variability from RISS.

VAST J111757.5+021607

VAST J111757.5+021607 was selected as a candidate via fitting to a decaying PL; the fitted light curve (Figure 3.3, *upper-left panel*) decays with a shallow slope of $-0.38^{+0.12}_{-0.08}$. The source is associated with both *WISE* and DECaLS counterparts (see Figure 3.4, *panel c*); the *WISE* colours ($[3.4\,\mu\text{m}]-[4.6\,\mu\text{m}] = 0.34\pm0.04$ mag and $[4.6\,\mu\text{m}]-[12\,\mu\text{m}] = 4.09\pm0.05$ mag) suggest the source is associated with a starburst galaxy at a photometric redshift (as determined by DECaLS) of $z_{\text{photo}} = 0.079$, i.e., at a luminosity distance of 370 Mpc.

Even though ATCA follow-up observations could not provide useful measurements due to the poor (u, v)-coverage arising from the source's proximity to the celestial equator, reliable measurements of the source at a higher frequency were obtained from quick-look images from two separate VLASS epochs taken on 2017 Dec 31 and 2020 Aug 11, respectively. The source was detected in the first VLASS epoch at 1.19 ± 0.38 mJy (measurement from the VLASS Quick Look Images catalogue; Gordon et al., 2021), but was below the 5σ detection threshold of 0.88 mJy in the second epoch. Since the uncertainties from the detection in the first epoch overlaps with the 5σ limit in the second epoch, we could not assess the degree nor significance of variability for the source at 3 GHz between the two epochs. The VAST-P measurements alone, however, indicate little variability[10], with the source having a modulation index of $V = 0.11$ and reduced χ^2 of $\eta = 0.43$ (calculated from the low-band VAST-P data points).

Taking these results, we assumed the source had limited variability and performed a spectral fit between the detections from the VAST-P observations taken at 888 MHz and the VLASS epoch 1 observation taken 2 yr prior at 3 GHz. This yielded a spectral index of -0.52 ± 0.07; interpolating the radio spectrum to 1.4 GHz gives a flux density of 1.77 ± 0.15 mJy, which is inconsistent with FIRST observations taken in 1998 July as shown in Figure 3.3 (*upper-right panel*). Those FIRST observations yielded a non-detection with a 5σ limit of 0.78 mJy, though there is a spatially coincident peak 4σ above the noise floor at $\sim$0.6 mJy. This suggests our prior assumption that the source has limited variability does not hold and instead indicates source brightening of *up to*[11] a factor of $\sim$3 in the 20 yr since the FIRST observation.

[10] Despite the small amount of variability, the source passed our F-statistic criterion, which compared the PL model to the constant benchmark model. This is because, while both models explained the data quite well with $\chi^2_{\text{PL}} = 1.24$ and $\chi^2_{\text{benchmark}} = 4.74$ (corresponding to p-values of 0.998 and 0.943, respectively), the F-statistic determines whether the PL fit is *significantly* better than the benchmark based on the ratio of the χ^2 values, not the absolute difference (see Equation 3.7). The resulting $F = 12.77$ corresponds to a p-value of 0.002 under the F-distribution with $(2, 9)$ degrees of freedom, indicating a *significantly* better fit for the PL model over the benchmark model.

[11] This is an upper limit since we must use the 5σ limit from the second epoch of VLASS, taken at a similar time as the VAST-P epochs, for the interpolation given that the source flux density evolves over time. The interpolation of this non-detection limit to 1.4 GHz yields an upper limit of 1.6 mJy.

A possible interpretation of these observations could be a variable or transient with variability on decade-long timescales found in a starburst radio galaxy. If this source is related to an orphan afterglow, it would decay similarly to the afterglow from that of a standard on-axis GRB (e.g., see figure 1 in Granot et al. 2018b); the fitted slope of $-0.38^{+0.12}_{-0.08}$ suggests an extreme, but possible (e.g., Ghisellini et al., 2009; Wang et al., 2015), electron spectral index $p{\sim}1.5$ for a burst exploding in a homogeneous interstellar-medium environment in the slow-cooling regime (e.g., Sari et al., 1998), following the relationship $S \propto t^{3(1-p)/4}$. However, these closure relations also necessitate, in this scenario, the spectrum to follow $S \propto \nu^{(1-p)/2}$; a value for $p{\sim}1.5$ implies a spectral index of $\alpha \sim -0.25$, which is inconsistent with the spectral index of -0.52 ± 0.07 fitted earlier using the epoch 1 VLASS detection (if we instead considered the more temporally aligned epoch 2 VLASS upper limit, the spectral index is even steeper, $\alpha < -0.8$, allowing us to arrive at the same conclusion). We therefore rule out the possibility the radio emission is afterglow related, but do not rule out the possibility it is produced by a non-afterglow related transient with variability on decade-long timescales.

In an alternate scenario treating the FIRST observations as an aberration, the low variability of the source with a modulation index smaller than that expected from RISS by a factor of three indicates the primary contribution to the radio emission is extended, emanating from the star-forming galaxy. The detection in the higher resolution VLASS epoch 1 data also supports the interpretation of extended radio emission, with an integrated-to-peak flux-density ratio of $S_I/S_P = 1.8$, though there are some systematic uncertainties affecting the integrated flux density differently to the peak flux density particularly at low flux densities (Lacy et al., 2020; Gordon et al., 2021). Under this interpretation, the radio emission may have been resolved out to a degree in the FIRST observations, which have comparable resolution to that of VLASS. The extended radio emission, arising from synchrotron processes associated with relativistic electrons accelerated in supernova remnants, could be used to infer the star formation rate (SFR) from recent star formation (10^8 yr) occurring in the galaxy (Condon, 1992). To calculate the SFR, we applied the relationship presented in Greiner et al. (2016):

$$\frac{\mathrm{SFR}}{M_\odot\,\mathrm{yr}^{-1}} = 0.059 \left(\frac{S_\nu}{\mathrm{\mu Jy}}\right) (1+z)^{-(\alpha+1)} \left(\frac{D_\mathrm{L}}{\mathrm{Gpc}}\right)^2 \left(\frac{\nu}{\mathrm{GHz}}\right)^{-\alpha}, \tag{3.9}$$

where S_ν is the total flux density, z is the redshift, α is the spectral index of the radio emission, D_L is the luminosity distance and ν is the observing frequency. The radio-derived SFR is $9.37\,M_\odot\,\mathrm{yr}^{-1}$ and this is consistent with previous studies of radio-derived SFR from star-forming radio galaxies in the local Universe (e.g., Bonzini et al., 2015). Although we currently favour this interpretation, continued long-term monitoring on the timescale of years would enable us to confirm whether the radio emission from VAST J111757.5+021607 is due to star formation from the host galaxy or the presence of a slowly evolving radio transient.

VAST J175036.1−181454

VAST J175036.1−181454 was selected as a candidate via fitting to a rising PL; the fitted light curve (Figure 3.3, *lower-left panel*) rises with a slope of $1.02^{+0.21}_{-0.21}$. This candidate is the only candidate in our sample we do not rule out as possibly afterglow related.

The radio spectrum inferred from the quasi-simultaneous low-band epoch 17 and mid-band epoch 18 observations taken one week apart appears to be inverted (positive), in contrast to the higher frequency ATCA observations which had a negative spectral slope. For each of the 2.1, 5.5 and 9.0 GHz frequency bands in the 22 March 5 ATCA observations, we split the 2 048 MHz bandwidth into four sub-bands, each with a bandwidth of 512 MHz, and imaged them to obtain a better spectral resolution (see Table 3.7). The resulting radio spectrum shown in Figure 3.3 (*lower-right panel*) reveals a spectral turnover at $\nu = 2.3 \pm 1.1$ GHz with a rise and decay index of $\delta_1 = 0.4 \pm 0.2$ and $\delta_2 = -0.9 \pm 0.1$, respectively, obtained from a fit to a SBPL. Due to a range of different factors in the 22 May 16 observations, including shorter integration time, more significant radio frequency interference, and poorer (u, v)-coverage, we could not obtain reliable flux-density measurements for the sub-bands to check whether the location of the spectral turnover had shifted; however, we note that the decay slope of $\alpha_{2.1-9\,\mathrm{GHz}} = -0.7 \pm 0.1$ is broadly consistent with the previous epoch of ATCA observations and the flux density faded by a factor of $\sim$1.3 across the entire radio spectrum.

The first epoch of ATCA observations also showed evidence for the source being extended at smaller spatial scales: while it was unresolved at 2.1 GHz with a beam size of $14.05'' \times 2.47''$, it had an integrated-to-peak flux-density ratio of $S_I/S_P \sim 1.4$ in each of the 5.5, 9.0, and 16.7 GHz observing bands, with beam sizes of $7.19'' \times 1.01''$, $4.44'' \times 0.65''$, and $3.73'' \times 0.44''$, respectively. This suggests that if the radio source is a transient, it could have some low-level contamination from its host galaxy or a slightly-extended foreground source. However, the source was unresolved in all bands of the second epoch of ATCA observations, which had lower angular resolution due to shorter baselines in the array configuration, as well as in the 2022 February 7 VLASS observation with beam size $2.82'' \times 1.67''$ (i.e., with angular resolution comparable to those in the first epoch of ATCA observations).

Since the source was not detected prior to epoch 17 (i.e., no detections in VAST-P1 or archival surveys), we classified this source as a transient. The modulation index of the source (calculated from the low-band VAST-P data points) $V = 1.29$ (and a reduced χ^2 of $\eta = 9.13$) cannot be explained by extrinsic variability from RISS (expected to be $V \sim 0.09$), which supports the classification of the source as a transient. It is located close to the Galactic plane ($l = 9.78°$, $b = 4.53°$) and 10.8° away from the Galactic Centre, though we rule out the possibility of this source being a Galactic Centre Radio Transient (this was a transient type we previously found near the Galactic Centre in a VAST-P1 variability search; Wang et al., 2021a) since it does not exhibit a steep spectrum nor show evidence of Stokes V emission in any of our radio datasets.

If we consider the source under the assumption its temporal and spectral evolution can be described by synchrotron radiation, which is common for extragalactic transients, we can independently estimate the electron spectral index p from the light-curve decay, using the relation $S \propto t^{(1-3p)/4}$, and the optically thin radio spectrum, using the relation $S \propto \nu^{(1-p)/2}$ (e.g., Granot & Sari, 2002). The analysis and assumptions used here are similar to what we have outlined in Subsection 3.4.2 when we assessed the viability of an orphan afterglow interpretation for VAST J111757.5+021607; the main difference here is that we have used relations valid for a burst exploding into a stellar wind environment (typical of long GRB and supernova environments) instead of an homogeneous interstellar medium environment (typical of short GRB environments) since we later show the radio luminosity of this transient disfavours a short GRB origin. Assuming the transient occurred approximately halfway between the last epoch of non-detection and the first epoch of detection, the temporal decay index inferred from the 5.5 GHz[12] ATCA observations is $\beta = -2.2 \pm 0.6$, corresponding to an electron spectral index of $p = 3.2 \pm 0.8$. We note that while the uncertainties are large since there are only two data points available after the light-curve turnover (and the uncertainties on the ATCA measurements are larger after accounting for systematics), this value is consistent with the more reliable estimate inferred from the optically thin segment of the high-signal radio spectrum obtained from the the first epoch of ATCA observation, $p = 2.8 \pm 0.2$. This inferred value for p is broadly consistent with the higher end of the electron spectral index distribution expected for GRBs (e.g., Wang et al., 2015), but also for other synchrotron transients.

A near-infrared counterpart with an association separation of $\sim 0\farcs4$ was found in the VISTA Variables in the Via Lactea Survey (VVV) DR2 catalogue (Minniti et al., 2010, 2017, see Figure 3.4, *panel d*), where it was morphologically classified as a galaxy. An optical counterpart with an association separation of $\sim 0\farcs3$ was also detected in a Pan-STARRS sky survey, allowing for the determination of a photometric redshift $z_{\rm photo} = 0.25 \pm 0.02$ (Beck et al., 2021). With a chance coincidence probability[13] of 0.6 per cent and 0.7 per cent respectively, we interpret these counterparts as the candidate host galaxy associated with the transient.

At the distance inferred from the photometric redshift, the transient has a measured peak spectral luminosity of $L_\nu = (7.5 \pm 0.6) \times 10^{30}\,{\rm erg\,s^{-1}\,Hz^{-1}}$ at 1.4 GHz and $\nu L_\nu = (1.1 \pm 0.1) \times 10^{40}\,{\rm erg\,s^{-1}}$, where the errors are propagated from the statistical uncertainties of the flux density measurements only. The inferred peak luminosity of this transient is incompatible with most classes of transients, including fast luminous

[12]We did not consider 2.1 and 9 GHz observations here because their reliability for estimating p is affected by the spectral turnover and low signal-to-noise, respectively.

[13]Calculated as $p_{\rm cc} = 1 - \exp(-\pi r^2 \sigma_{\leq m})$, where r is the angular offset of the counterpart from the radio source location and $\sigma_{\leq m}$ is the average surface density of sources brighter than the counterpart magnitude m in the region near the source.

transients[14], short GRBs and all classes of supernovae (e.g., see figure 9 in Ho et al., 2020a); only the most luminous classes of transients, i.e., long GRBs and the sub-class of relativistic TDEs (e.g., *Swift* J164449.3+573451; Zauderer et al., 2011, Alexander et al. 2020), are consistent with the inferred peak luminosity of VAST J175036.1−181454.

In the long GRB scenario, we used an updated version of the catalogue compiled in Leung et al. (2021a) to check for any GRBs that are both temporally (occurring between the third last non-detection and the first detection) and spatially (GRB error region containing the transient sky direction) consistent with the transient; we found no corresponding high-energy trigger and therefore classify this transient as a strong orphan afterglow candidate. The catalogue we used for these checks also included sub-threshold triggers from the *Swift*/Burst Alert Telescope (BAT) Gamma-Ray Urgent Archiver for Novel Opportunities (GUANO; Tohuvavohu et al., 2020) programme, low-significance *INTEGRAL* WEAK alert events[15] and unclassified *Fermi*/Gamma-ray Burst Monitor (GBM) triggers[16]. We also found no association with any known TDEs after checking with published databases[17], which was expected in the off-axis TDE scenario.

This transient is the target of an ongoing follow-up programme, involving the addition of low-frequency and high-resolution radio facilities, high-energy follow-up as well as spectroscopic observations. The goal of this programme is to definitively classify and better characterise the transient; we will present the results from this programme in a future work.

3.5 Discussion and Conclusions

The follow-up observations and analysis of the five orphan afterglow candidates revealed the following:

1. one candidate is likely a synchrotron transient, with an off-axis afterglow or an off-axis TDE as the leading interpretations;
2. one candidate is likely a flaring AGN, displaying a flat-to-steep radio-spectral transition over the span of 4 months;

[14]One exception to this is ZTF18abvkwla (the “Koala”), which had also reached $\nu L_\nu \gtrsim 10^{40}\,\mathrm{erg\,s^{-1}}$ – this is more than an order of magnitude higher than other fast luminous transients in the literature. The rise time of the “koala” at radio frequencies, in particular, occurred on shorter timescales than what was observed for VAST J175036.1−181454. For these reasons, we currently disfavour a fast luminous transient origin for this transient, but do not rule it out entirely – a more careful consideration will be discussed in future work.

[15]These are circulated via the *INTEGRAL* Burst Alert System (Mereghetti et al., 2003) and can be found at: http://ibas.ncac.torun.pl/~jubork/ibas/ibas.php?slcn=weak

[16]These include *all* triggers (including those not classified as GRBs) found in the following database maintained by NASA/GSFC: https://heasarc.gsfc.nasa.gov/W3Browse/fermi/fermigtrig.html

[17]The databases we used included the Transient Name Server (maintained by the IAU supernova working group, https://www.wis-tns.org/) and the Open TDE Catalogue (maintained by James Guillochon, https://tde.space)

3. one candidate is associated with a starburst galaxy, with the radio emission originating from either star formation or an underlying slowly evolving transient; and
4. the remaining two candidates are likely extrinsic variables caused by interstellar scintillation.

We discuss and summarise the possible implications of these results on transient and GRB rates as well as for future radio transient studies.

3.5.1 Rates and the Inverse Beaming Fraction

From this work, we found one extragalactic radio transient in the VAST-P, which repeatedly covered a footprint of $\sim$5 000 deg^2 over a 2.5-yr span. Considering $\sim$30 d transient timescales (typical of gigahertz extragalatic synchrotron sources at our survey sensitivity; e.g., Ghirlanda et al., 2014; Metzger et al., 2015), the effective sky area covered by VAST-P (low-band) is 35 820 deg^2, implying a surface transient density of $(2.79^{+12.8}_{-2.72}) \times 10^{-5}\,\mathrm{deg}^{-2}$ (the upper and lower limits represent the 95 per cent confidence interval as defined in Gehrels 1986) at the flux-density threshold of $\sim$2 mJy[18]. We note that: (a) comparisons with previous variability surveys should be taken with care since many sources we had ruled out as being transients would have been classified as transients in previous surveys which spanned much shorter time periods, and (b) the rate can be considered a conservative lower limit rate as it does not account for possible detection of transients from traditional statistical search techniques (although our preliminary analysis of the VAST-P data suggests no additional radio transients have been found).

Estimating the event rate for objects similar to the one transient we had found, VAST J175036.1−181454, we find:

$$\mathcal{R} \approx \frac{1\,\mathrm{event}}{\Delta t \Delta\Omega(\frac{4}{3}\pi d^3) C_{2\mathrm{mJy}}} \approx 0.52^{+2.36}_{-0.51}\,\mathrm{Gpc}^{-3}\,\mathrm{yr}^{-1}, \tag{3.10}$$

where $\Delta t \sim 2.5\,\mathrm{yr}$ is the temporal baseline of VAST-P (low-band), $\Delta\Omega \sim 0.12$ is the fractional sky coverage of the VAST-P (low-band) footprint, $d \sim 1.3\,\mathrm{Gpc}$ is the maximum distance at which a source as luminous as VAST J175036.1−181454 would be detectable above $\sim$2 mJy, and $C_{2\mathrm{mJy}} \sim 0.7$ is the completeness of VAST-P (low-band) at 2 mJy (Hale et al., 2021). The corresponding 95 per cent confidence interval is then 0.01-2.88 $\mathrm{Gpc}^{-3}\,\mathrm{yr}^{-1}$. This estimated rate for VAST J175036.1−181454-like objects is compatible with predicted rates for off-axis long GRBs and off-axis TDEs, but are too small to be consistent with short GRBs and supernovae; this is in agreement with the surface transient density inferred from the search results, which is also compatible with predictions for off-axis long GRBs and off-axis TDEs at gigahertz frequency (see table 1 and figure 3 in Metzger et al., 2015).

If indeed VAST J175036.1−181454 is an off-axis long GRB, the average inverse beaming fraction can then be estimated using the method introduced in Levinson

[18]Our search criteria in Section 3.3 requires at least two 7.5σ detections or one 10σ detection. With $\sigma_{\mathrm{rms}} = 0.24\,\mathrm{mJy\,beam}^{-1}$, this is equivalent to $\sim$2 mJy.

et al. (2002)[19]:

$$\langle f_{\rm b}^{-1}\rangle \approx 70\,N \left(\frac{\mathcal{R}_{\text{on-axis}}}{0.3\,\text{Gpc}^{-3}\,\text{yr}^{-1}}\right)^{-1} \left(\frac{E_{\theta,\rm kin}}{10^{51}\,\text{erg}}\right)^{-11/6} \times \left(\frac{n}{10\,\text{cm}^{-3}}\right)^{-19/24} \left(\frac{\epsilon_{\rm e}}{0.1}\right)^{-3/2} \left(\frac{\epsilon_{\rm B}}{0.001}\right)^{-9/8}, \tag{3.11}$$

where N is the number of orphan afterglows found in the search above the minimum flux-density threshold of 2 mJy at gigahertz frequency (this is the all-sky number so we had corrected our observed count by the sky fraction $\Delta\Omega$ and survey completeness $C_{\rm 2mJy}$), $\mathcal{R}_{\text{on-axis}}$ is the observed rate for on-axis long GRBs in the local Universe, $E_{\theta,\rm kin}$ is the total beam-corrected kinetic energy in the blast wave, n is density of the circumburst medium, $\epsilon_{\rm e}$ and $\epsilon_{\rm B}$ are the fractional shock energies in the accelerated electrons and magnetic fields, respectively. Taking $\mathcal{R}_{\text{on-axis}} = 0.3\,\text{Gpc}^{-3}\,\text{yr}^{-1}$ (e.g., Guetta et al., 2005), $E_{\theta,\rm kin} = 10^{51}$ erg (e.g., Frail et al., 2001), $n = 10\,\text{cm}^{-3}$ (e.g., Ghisellini et al., 2009), $\epsilon_{\rm e} = 0.1$ (e.g., Beniamini & van der Horst, 2017) and $\epsilon_{\rm B} = 0.001$ (e.g., Santana et al., 2014), we obtain the average inverse beaming factor $\langle f_{\rm b}^{-1}\rangle = 860^{+1980}_{-710}$, or equivalently, an average jet opening angle of $\langle\theta_{\rm j}\rangle = 3^{+4}_{-1}$ deg, and an implied true long GRB rate of $\langle f_{\rm b}^{-1}\rangle\,\mathcal{R}_{\text{on-axis}} = 260^{+590}_{-210}\,\text{Gpc}^{-3}\text{yr}^{-1}$ (uncertainties representing the 1σ confidence intervals). While these results are broadly consistent with previous studies (e.g., Frail et al., 2001; Levinson et al., 2002; Guetta et al., 2005; Gal-Yam et al., 2006; Goldstein et al., 2016; Mooley et al., 2022; Ghirlanda & Salvaterra, 2022), we caution that our estimate is only a general approximation, since the methodology suffers from being fairly model dependent (e.g., the distribution of possible values for both $E_{\theta,\rm kin}$ and $\epsilon_{\rm B}$ span a few orders of magnitude and have a strong dependence – approximately quadratic and linear, respectively – on the average inverse beaming fraction $\langle f_{\rm b}^{-1}\rangle$) and also because our results still have many uncertainties remaining (e.g., confirmation of the transient photometric redshift, modelling of the microphysical parameters, etc.).

3.5.2 Radio Transient Search Strategies

VAST-P is one of the first radio surveys to have repeated, regular coverage of a significant fraction of the sky, allowing for comprehensive light curves spanning years to be built for many sources. This has allowed for the sensitivity of different search techniques to variables and transients with different types of light curves – including those with random/stochastic variations, a single pulse/spike, slow power-law rises/decays – to be explored in depth. In particular, we compare the utility of the standard $\eta - V$ statistical approach with our matched-filter approach in variability and transient surveys. Figure 3.5 shows a plot of the η and V values for all sources in the VAST-P footprint: the shaded area represents the region in variability parameter space exceeding the 3σ thresholds for both η and V, while the overlaid markers represent the five orphan afterglow candidates presented in Section 3.4 (as well as GRB 171205A).

[19] τ_i, the time at which the afterglow becomes isotropic, has a weak dependence with the inverse beaming fraction $f_{\rm b}^{-1} \propto \tau_i^{7/20}$ so we do not consider this parameter in our estimation (giving it the default assumed value of 3 yr)

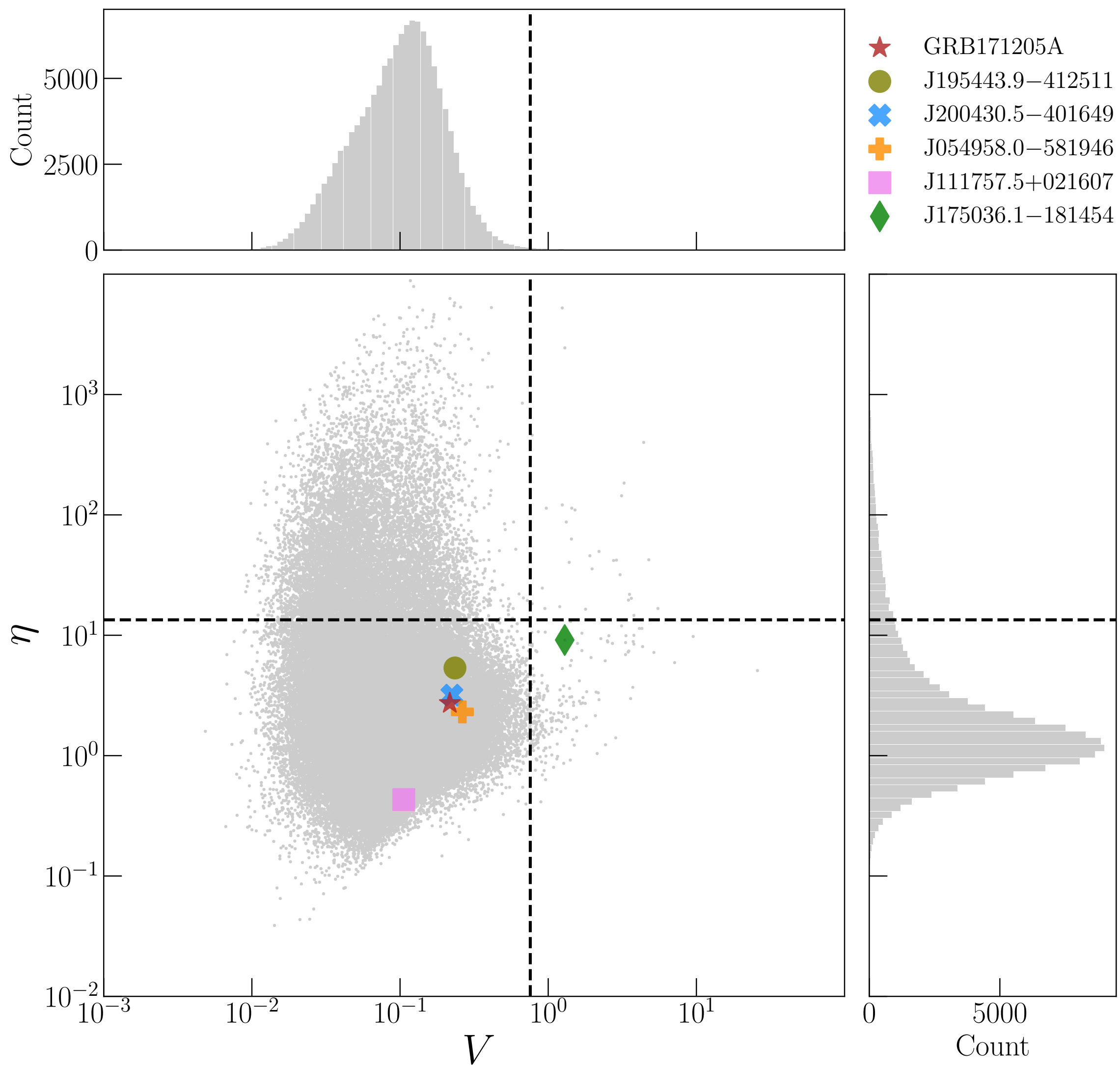

Figure 3.5: Plot of η against V, two standard variability metrics used to identify variable and transient radio sources in VAST-P. The dotted lines are 3σ thresholds for the variability statistics, above which (represented by the light yellow shaded region) a radio source is identified as a strong variable or transient: $\eta = 13.43$ (horizontal line) and $V = 76$ per cent. Each grey point represents a source in VAST-P. Candidates from this work and GRB 171205A, which motivated this work, are represented by different colours and markers as shown in the legend on the upper right of the plot.

Sources with light curves that exhibit random, stochastic variations are now routinely recovered with the $\eta - V$ approach, provided these variations exceed the statistical thresholds defined by the search parameters. These light curves make up the majority of the 71 sources in the shaded region of Figure 3.5 and also all the variables identified in the search performed on VAST-P1 (Murphy et al., 2021). They are typical of those that may be expected in radio stars, pulsars as well as strong scintillators. For sources with single pulse or spike light curves, which would be observed from a transient whose timescale for rise and decay are faster than the sampling cadence of the survey, the $\eta - V$ approach would be able to recover a subset of the most luminous sources. If we assume the same noise characteristics and number of observations as VAST-P (low-band), a light curve with a single spike would only be detected by an $\eta - V$ search with 3σ thresholds on η and V if the spike was above $\sim$3 mJy (i.e., a 12σ detection). For a transient with peak spectral luminosity of $\sim 10^{30}\,\mathrm{erg\,s^{-1}\,Hz^{-1}}$ at gigahertz frequency (typical of a bright, long GRB radio afterglow), this equates to a detectability radius out to redshift $z \sim 0.1$ or luminosity distance $D_{\mathrm{L}} \sim 500\,\mathrm{Mpc}$. This suggests only rare transients, which are both bright and nearby, would be detectable in a search with similar survey and variability parameters, possibly leading to a biased sample of extragalactic transients.

The matched-filter approach for finding variables and transients is limited by the functional forms or templates that the light curves need to fit. This makes finding both sources with random, stochastic variations and those with a single spike in their light curve very difficult for a PL/SBPL matched-filter. However, if an appropriate functional template is chosen, they allow the identification of variables and transients with much lower levels of significance (based on traditional variability metrics) and closer to the noise. For example, unlike a requirement for a 12σ detection, a matched-filter approach using a top-hat template had been introduced to find single-spike transients close to the noise (Feng et al., 2017); although the study was implemented at much lower frequencies ($< 200\,\mathrm{MHz}$) and did not find any transients. In this work, the PL/SBPL matched-filter was designed to find synchrotron transients, in particular, orphan GRB afterglows, with temporal rise and decays following power laws. This was motivated by the slow temporal evolution in GRB 171205A at low frequencies at late times (Leung et al., 2021a). Just like GRB 171205A, all five orphan afterglow candidates identified with the PL/SBPL matched-filter in this work would not have been detected in an $\eta - V$ search using 3σ thresholds[20] (see Figure 3.5).

[20] We note that with more relaxed 2σ thresholds, which would yield 304 variable and transient candidates, VAST J175036.1−181454 would have been detected.

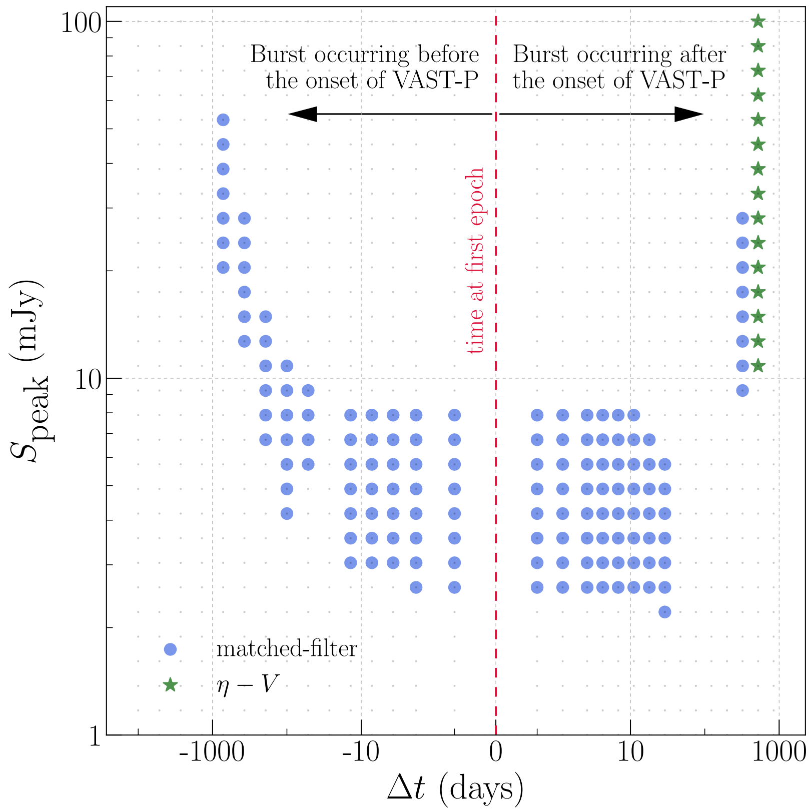

Figure 3.6: A grid of 900 light curves, generated using a SBPL functional template, varying logarithmically in its input parameters S_{peak} (the maximum flux density) and Δt (time elapsed between the first measurement and the time of a burst event). The blue circular markers represent the light curves that would be recovered through a PL/SBPL matched-filter search, while the green star markers represent the light curves that would be recovered through a search using the η, V variability metrics at 3σ thresholds.

As an illustrative example, we compare the transient yields of the matched-filter approach to the standard $\eta - V$ approach for sources with SBPL light curves in Figure 3.6. To do this, we generated 900 light curves, varying the S_{peak} (flux density at the light-curve peak) and Δt (time elapsed between the first measurement and the time of a burst event) parameters over a logarithmic grid; the S_{peak} parameter varied from 1 to 100 mJy and the Δt parameter from $-10\,000$ to $1\,000$ days. We fixed the time of peak to $t_{\mathrm{peak}} = 100$ days (consistent with predictions from afterglow models with typical microphysical parameters; Sari et al., 1998), the rise slope to $\delta_1 = 1$ (the expected rise slope for an on-axis GRB in a wind environment; while this parameter varies considerably depending on the inclination angle and jet model for an off-axis GRB, we found the effect on our simulation results below is negligible) and the decay slope to $\delta_2 = -1.5$ (corresponding to $p = 2.3$ for a GRB exploding in a wind environment). For each light curve, we replicated the same observing cadence as our VAST-P observations (low-band) (see Table 3.1) and added two sources of noise (see Section 3.1): (a) from the scatter in the VAST-P flux-density scale, and (b) from the image noise.

Figure 3.6 shows the light curves that would be recovered through a PL/SBPL matched-filter search (blue circular markers) compared to those that would be recovered through a search using the η, V variability metrics at 3σ thresholds (green star markers). The results show that the $\eta - V$ search performs well in finding new and bright afterglow events, but is otherwise hampered by the mean flux-density normalisation factor in the modulation index (Equation 3.2) for events with many more data points. Alternatively, the PL/SBPL matched-filter is able to recover sources occurring much earlier and with lower brightness. Its performance, however, is hampered for sources with peak brightness greater than 10 mJy due to the large scatter in the flux-density scale (but this is expected to improve in future ASKAP surveys). While the results suggest the matched-filter approach would be unable to recover bursts occurring greater than 1 000 days before the first epoch, we did not account for possible flattening in the light-curve decay, which may be expected as the afterglow enters the deep-Newtonian regime (Sironi & Giannios, 2013). Our illustrative example here therefore suggests the $\eta - V$ approach would be sensitive to more bursty light curves (such as radio emission from a new burst), while the matched-filter approach would be more sensitive to lower signal and slowly evolving light curves (such as radio emission from a burst occurring many years prior), which is consistent with our expectations.

Although the matched-filter approach is effective in finding transient candidates exhibiting PL/SBPL light-curve structure, confirmation and characterisation of these transient candidates rely on complementary information. In Section 3.3, the 193 candidates from the PL/SBPL matched-filter cuts were narrowed down to five only after the use of multi-frequency radio data (ruling out ∼30 per cent of candidates) and archival radio data (ruling out ∼40 per cent of candidates), among other auxiliary information including, but not limited to, multi-wavelength and/or redshift information. This work therefore highlights the need for (a) multiple, complementary approaches to variability searches in addition to the use of standard variability metrics (in particular, we showed the addition of the matched-filter approach would benefit afterglow and synchrotron transient recovery), and (b) the availability of both archival and contemporaneous, complementary, multi-frequency/wavelength data, in order to maximise the scientific value of future variability and transient surveys.

Acknowledgements

We thank the anonymous referee for their useful comments that improved the quality of this manuscript. We also thank Jess Broderick, Dougal Dobie, Marcello Giroletti, Marcus Lower, Ilya Mandel, Hao Qiu and Om Sharan Salafia for useful discussions. JL is supported by Australian Government Research Training Program Scholarships. TM acknowledges the support of the Australian Research Council through grant DP190100561. GG acknowledges the support of the PRIN-INAF "Towards the SKA and CTA era: discovery, localisation, and physics of transient sources" grant (1.05.01.88.06) and PRIN-MUR 2017 grant (20179ZF5KS). DK is supported by National Science Foundation grant AST-1816492. Parts of this research were conducted by the Australian Research Council Centre of Excellence for Gravitational Wave Discovery (OzGrav), through project number CE170100004.

This scientific work uses data obtained from Inyarrimanha Ilgari Bundara / the Murchison Radio-astronomy Observatory. We acknowledge the Wajarri Yamaji People as the Traditional Owners and native title holders of the Observatory site. CSIRO's ASKAP radio telescope is part of the Australia Telescope National Facility (https://ror.org/05qajvd42). Operation of ASKAP is funded by the Australian Government with support from the National Collaborative Research Infrastructure Strategy. ASKAP uses the resources of the Pawsey Supercomputing Research Centre. Establishment of ASKAP, Inyarrimanha Ilgari Bundara, the CSIRO Murchison Radio-astronomy Observatory and the Pawsey Supercomputing Research Centre are initiatives of the Australian Government, with support from the Government of Western Australia and the Science and Industry Endowment Fund. The Australia Telescope Compact Array is part of the Australia Telescope National Facility (https://ror.org/05qajvd42) which is funded by the Australian Government for operation as a National Facility managed by CSIRO. We acknowledge the Gomeroi people as the Traditional Owners of the Observatory site.

This research was supported by the Sydney Informatics Hub (SIH), a core research facility at the University of Sydney. This work was also supported by software support resources awarded under the Astronomy Data and Computing Services (ADACS) Merit Allocation Program. ADACS is funded from the Astronomy National Collaborative Research Infrastructure Strategy (NCRIS) allocation provided by the Australian Government and managed by Astronomy Australia Limited (AAL).

This publication makes use of data products from the *Wide-field Infrared Survey Explorer*, which is a joint project of the University of California, Los Angeles, and the Jet Propulsion Laboratory/California Institute of Technology, funded by the National Aeronautics and Space Administration.

The Legacy Surveys consist of three individual and complementary projects: the Dark Energy Camera Legacy Survey (DECaLS; Proposal ID #2014B-0404; PIs: David Schlegel and Arjun Dey), the Beijing-Arizona Sky Survey (BASS; NOAO Prop. ID #2015A-0801; PIs: Zhou Xu and Xiaohui Fan), and the Mayall z-band Legacy Survey (MzLS; Prop. ID #2016A-0453; PI: Arjun Dey). DECaLS, BASS and MzLS together include data obtained, respectively, at the Blanco telescope, Cerro Tololo Inter-American Observatory, NSF' s NOIRLab; the Bok telescope, Steward Observatory, University of Arizona; and the Mayall telescope, Kitt Peak National Observatory, NOIRLab. Pipeline processing and analyses of the data were supported by NOIRLab and the Lawrence Berkeley National Laboratory (LBNL). The Legacy Surveys project is honored to be permitted to conduct astronomical research on Iolkam Du' ag (Kitt Peak), a mountain with particular significance to the Tohono O' odham Nation. NOIRLab is operated by the Association of Universities for Research in Astronomy (AURA) under a cooperative agreement with the National Science Foundation. LBNL is managed by the Regents of the University of California under contract to the U.S. Department of Energy. This project used data obtained with the Dark Energy Camera (DECam), which was constructed by the Dark Energy Survey (DES) collaboration. Funding for the DES Projects has been provided by the U.S. Department of Energy, the U.S. National Science Foundation, the Ministry of Science and Education of Spain, the Science and Technology Facilities Council of the United Kingdom, the Higher Education Funding Council for England, the National Center for Supercomputing Applications at the University of Illinois at Urbana-Champaign, the Kavli Institute of Cosmological Physics at the University of Chicago, Center for Cosmology and Astro-Particle Physics at the Ohio State University, the Mitchell Institute for Fundamental Physics and Astronomy at Texas A&M University, Financiadora de Estudos e Projetos, Fundacao Carlos Chagas Filho de Amparo, Financiadora de Estudos e Projetos, Fundacao Carlos Chagas Filho de Amparo a Pesquisa do Estado do Rio de Janeiro, Conselho Nacional de Desenvolvimento Cientifico e Tecnologico and the Ministerio da Ciencia, Tecnologia e Inovacao, the Deutsche Forschungsgemeinschaft and the Collaborating Institutions in the Dark Energy Survey. The Collaborating Institutions are Argonne National Laboratory, the University of California at Santa Cruz, the University of Cambridge, Centro de Investigaciones Energeticas, Medioambientales y Tecnologicas-Madrid, the University of Chicago, University College London, the DES-Brazil Consortium, the University of Edinburgh, the Eidgenossische Technische Hochschule (ETH) Zurich, Fermi National Accelerator Laboratory, the University of Illinois at Urbana-Champaign, the Institut de Ciencies de l' Espai (IEEC/CSIC), the Institut de Fisica d' Altes Energies, Lawrence Berkeley National Laboratory, the Ludwig Maximilians Universitat Munchen and the associated Excellence Cluster Universe, the University of Michigan, NSF' s NOIRLab, the University of Nottingham, the Ohio State University, the University of Pennsylvania, the University of Portsmouth, SLAC National Accelerator Laboratory, Stanford University, the University of Sussex, and Texas A&M University. BASS is a key project of the Telescope Access Program (TAP), which has been funded by the National Astronomical Observatories of China, the Chinese Academy of Sciences (the Strategic Priority Research Program "The Emergence of Cosmological Structures" Grant # XDB09000000), and the Special Fund for Astronomy from the Ministry of Finance. The BASS is also supported by the External Cooperation Program of Chinese Academy of Sciences (Grant # 114A11KYSB20160057), and Chinese National Natural Science Foundation (Grant # 12120101003, # 11433005). The Legacy Survey team makes use of data products from the Near-Earth Object Wide-field Infrared Survey Explorer (NEOWISE), which is a project of the Jet Propulsion Laboratory/California Institute of Technology. NEOWISE is funded by the National Aeronautics and Space Administration. The Legacy Surveys imaging of the DESI footprint is supported by the Director, Office of Science, Office of High Energy Physics of the U.S. Department of Energy under Contract No. DE-AC02-05CH1123, by the National Energy Research Scientific Computing Center, a DOE Office of Science User Facility under the same contract; and by the U.S. National Science Foundation, Division of Astronomical Sciences under Contract No. AST-0950945 to NOAO. The Photometric Redshifts for the Legacy Surveys (PRLS) catalogue used in this paper was produced thanks to funding from the U.S. Department of Energy Office of Science, Office of High Energy Physics via grant DE-SC0007914. The Pan-STARRS1 Surveys (PS1) and the PS1 public science archive have been made possible through contributions by the Institute for Astronomy, the University of Hawaii, the Pan-STARRS Project Office, the Max-Planck Society and its participating institutes, the Max Planck Institute for Astronomy, Heidelberg and the Max Planck Institute for Extraterrestrial Physics, Garching, The Johns Hopkins University, Durham University, the University of Edinburgh, the Queen's University Belfast, the Harvard-Smithsonian Center for Astrophysics, the Las Cumbres Observatory Global Telescope Network Incorporated, the National Central University of Taiwan, the Space Telescope Science Institute, the National Aeronautics and Space Administration under Grant No. NNX08AR22G issued through the Planetary Science Division of the NASA Science Mission Directorate, the National Science Foundation Grant No. AST-1238877, the University of Maryland, Eotvos Lorand University (ELTE), the Los Alamos National Laboratory, and the Gordon and Betty Moore Foundation.

Based on observations made with ESO Telescopes at the La Silla or Paranal Observatories under programme ID(s) 179.B-2002(B), 179.B-2002(A), 179.B-2002(C).

This research has made use of the CIRADA cutout service at URL cutouts.cirada.ca, operated by the Canadian Initiative for Radio Astronomy Data Analysis (CIRADA). CIRADA is funded by a grant from the Canada Foundation for Innovation 2017 Innovation Fund (Project 35999), as well as by the Provinces of Ontario, British Columbia, Alberta, Manitoba and Quebec, in collaboration with the National Research Council of Canada, the US National Radio Astronomy Observatory and Australia's Commonwealth Scientific and Industrial Research Organisation.

Data Availability

The ASKAP data used in this paper can be accessed through the CSIRO ASKAP Science Data Archive (CASDA)[21]. Specifically the data from the RACS and VAST projects are available under the codes AS110 and AS107, respectively. The ATCA data used in this paper can be accessed through the Australia Telescope Online Archive (ATOA)[22] under the project code C3363. Reasonable requests for other auxiliary datasets can be accommodated for via email to the corresponding author.

3.6 Appendix: Measurement Tables

This appendix section provides the full table of radio measurements for all five orphan afterglow candidates investigated in Section 3.4, including the measurements from the follow-up ATCA observations carried out in this work.

[21] https://data.csiro.au/dap/public/casda/casdaSearch.zul
[22] https://atoa.atnf.csiro.au/query.jsp

Table 3.6: Radio observations of the three orphan afterglow candidates we obtained from performing a SBPL fit to the source light curves. Columns 1 through 4 show the date of observation, the radio survey or observing telescope, the central frequency of the radio image, and the flux-density measurements for the observation. Epochs of ATCA follow-up observations detailed in Subsection 3.4.1 separated by dashed horizontal lines. For the ATCA 2022 September 8 observation, images produced from using the full 2 048 MHz bandwidth is indicated with the dagger (†) symbol; all other images from that epoch are produced from using a sub-band with 512 MHz bandwidth. For a non-detection, a 5σ limit is reported and, where applicable, a measurement from forced extraction (see Subsection 3.2.2) is given in parenthesis. The reported uncertainties are purely statistical and these were the uncertainties used for calculations in our pipelines. The systematic errors (not factored into our quoted numbers) are $\lesssim 5$ per cent for ATCA (e.g. Reynolds, 1994; Tingay et al., 2003), $\sim$10 per cent for VLASS (Lacy et al., 2022), typically $\sim$7 per cent but *up to* $\sim$30 per cent for ASKAP (McConnell et al., 2020; Duchesne et al., 2023).

Date (UT)	Survey or Telescope	ν (GHz)	S_ν (mJy)
SBPL Candidate 1: VAST J195443.9−412511			
2019 Apr 30	VAST-P	0.887	< 3.64 (2.42 ± 0.73)
2019 Aug 28	" "	" "	5.11 ± 0.37
2019 Oct 30	" "	" "	6.26 ± 0.39
2020 Jan 26	" "	" "	5.68 ± 0.37
2020 Jan 27	" "	" "	5.55 ± 0.35
2020 Jun 21	" "	" "	4.66 ± 0.43
2020 Jul 4	FLASH-P	0.855	6.39 ± 0.02
2020 Aug 30	VAST-P	0.887	5.32 ± 0.49
2021 Jul 22	" "	" "	4.14 ± 0.32
2021 Jul 30	" "	1.367	4.44 ± 0.31
2021 Aug 22	" "	0.887	4.28 ± 0.31
2021 Sep 24	" "	1.367	4.45 ± 0.26
2021 Nov 20	" "	" "	4.36 ± 0.26
2022 May 16	ATCA	2.100	3.99 ± 0.23
" "	" "	5.500	3.71 ± 0.09
" "	" "	9.000	3.44 ± 0.10
2022 Sep 8	ATCA	1.332	3.87 ± 0.33
" "	" "	1.844	3.95 ± 0.18
" "	" "	2.100†	3.76 ± 0.13
" "	" "	2.356	3.57 ± 0.16
" "	" "	2.868	3.18 ± 0.20
" "	" "	4.732	2.72 ± 0.19
" "	" "	5.244	2.48 ± 0.16
" "	" "	5.500†	2.62 ± 0.11
" "	" "	5.756	2.43 ± 0.17
" "	" "	6.268	2.29 ± 0.20
" "	" "	8.232	1.86 ± 0.14
" "	" "	8.744	1.59 ± 0.15
" "	" "	9.000†	1.65 ± 0.08
" "	" "	9.256	1.57 ± 0.17
" "	" "	9.768	1.38 ± 0.16

continued on the next page

continued from the previous page

Date (UT)	Survey or Telescope	ν (GHz)	S_ν (mJy)
SBPL Candidate 2: VAST J200430.5−401649			
2018 Feb 3	VLASS	3.000	< 0.66
2019 Apr 30	VAST-P	0.887	< 2.78 (2.55 ± 0.56)
2019 Aug 28	VAST-P	0.887	4.45 ± 0.46
2019 Oct 30	""	""	5.16 ± 0.50
2020 Jan 26	""	""	4.68 ± 0.51
2020 Jan 27	""	""	4.70 ± 0.52
2020 Jun 21	""	""	3.66 ± 0.44
2020 Jul 4	FLASH-P	0.855	4.31 ± 0.03
2020 Aug 30	VAST-P	0.887	4.10 ± 0.53
2020 Nov 9	VLASS	3.000	< 0.82
2021 Jul 22	VAST-P	0.887	3.40 ± 0.45
2021 Jul 30	""	1.367	2.58 ± 0.31
2021 Aug 22	""	0.887	2.91 ± 0.43
2021 Sep 24	""	1.367	2.47 ± 0.34
2021 Nov 20	""	""	2.40 ± 0.30
2022 May 16	ATCA	2.100	2.19 ± 0.54
""	""	5.500	0.92 ± 0.08
""	""	9.000	0.54 ± 0.08
SBPL Candidate 3: VAST J054958.0−581946			
2019 May 4	VAST-P	0.887	< 1.20 (0.73 ± 0.24)
2019 Aug 27	""	""	1.96 ± 0.34
2019 Oct 29	""	""	1.82 ± 0.30
2019 Oct 31	""	""	1.62 ± 0.29
2019 Dec 19	""	""	< 1.29 (1.47 ± 0.26)
2020 Jan 10	""	""	1.30 ± 0.25
2020 Jan 16	""	""	1.46 ± 0.26
2020 Jan 17	""	""	1.68 ± 0.21
2020 Jan 18	""	""	1.75 ± 0.21
2020 Jun 20	""	""	1.51 ± 0.21
2020 Aug 28	""	""	< 1.30 (1.01 ± 0.26)
2021 Jul 24	""	""	< 0.99 (0.94 ± 0.20)
2021 Aug 22	""	""	1.13 ± 0.19
2022 May 16	ATCA	2.100	1.07 ± 0.14
""	""	5.500	0.65 ± 0.09
""	""	9.000	0.51 ± 0.04

Table 3.7: Radio observations of the two orphan afterglow candidates we obtained from performing a PL fit to the source light curves. Columns 1 through 4 show the date of observation, the radio survey or observing telescope, the central frequency of the radio image, and the flux-density measurements for the observation. Epochs of ATCA follow-up observations detailed in Subsection 3.4.1 separated by dashed horizontal lines. For the ATCA 2022 March 5 observation, images produced from using the full 2 048 MHz bandwidth is indicated with the dagger (†) symbol; all other images from that epoch are produced from using a sub-band with 512 MHz bandwidth. For a non-detection, a 5σ limit is reported and, where applicable, a measurement from forced extraction (see Subsection 3.2.2) is given in parenthesis. The reported uncertainties are purely statistical and these were the uncertainties used for calculations in our pipelines. The systematic errors (not factored into our quoted numbers) are $\lesssim 5$ per cent for ATCA (e.g. Reynolds, 1994; Tingay et al., 2003), ∼10 per cent for VLASS (Lacy et al., 2022), typically ∼7 per cent but *up to* ∼30 per cent for ASKAP (McConnell et al., 2020; Duchesne et al., 2023).

Date (UT)	Survey or Telescope	ν (GHz)	S_ν (mJy)
PL Candidate 1: VAST J111757.5+021607			
1998 Jul	FIRST	1.400	< 0.78
2017 Dec 31	VLASS	3.000	1.19 ± 0.38
2019 Aug 28	VAST-P	0.887	2.48 ± 0.27
2019 Oct 30	" "	" "	2.30 ± 0.29
2019 Dec 19	" "	" "	2.36 ± 0.30
2020 Jan 10	" "	" "	< 4.15 (1.67 ± 0.83)
2020 Jan 16	" "	" "	2.42 ± 0.31
2020 Jan 24	" "	" "	2.27 ± 0.26
2020 Jan 25	" "	" "	2.36 ± 0.27
2020 May 2	" "	" "	2.20 ± 0.35
2020 Jun 20	" "	" "	2.12 ± 0.25
2020 Aug 11	VLASS	3.000	< 0.88
2020 Aug 29	VAST-P	0.887	2.30 ± 0.32
2021 Jul 23	" "	" "	1.93 ± 0.25
2021 Aug 22	" "	" "	2.00 ± 0.24

continued on the next page

continued from the previous page

Date (UT)	Survey or Telescope	ν (GHz)	S_ν (mJy)
PL Candidate 2: VAST J175036.1−181454			
2019 Jun 30	VLASS	3.000	< 0.84
2019 Aug 28	VAST-P	0.887	< 1.26 (0.27 ± 0.25)
2019 Oct 29	" "	" "	< 1.35 (-0.01 ± 0.27)
2019 Oct 30	" "	" "	< 1.21 (-0.23 ± 0.24)
2020 Jan 11	" "	" "	< 1.15 (0.57 ± 0.23)
2020 Jan 18	" "	" "	< 1.23 (0.25 ± 0.25)
2020 Jan 19	" "	" "	< 1.16 (0.37 ± 0.23)
2020 May 3	" "	" "	< 1.18 (0.03 ± 0.24)
2020 Jun 20	" "	" "	< 1.18 (0.29 ± 0.24)
2020 Aug 29	" "	" "	< 1.51 (0.55 ± 0.30)
2021 Jul 23	" "	" "	1.66 ± 0.22
2021 Jul 29	" "	1.367	3.06 ± 0.34
2021 Aug 21	" "	0.887	1.82 ± 0.20
2021 Sep 25	" "	1.367	3.88 ± 0.30
2021 Nov 20	" "	" "	3.13 ± 0.34
2022 Feb 7	VLASS	3.000	2.39 ± 0.28
2022 Mar 5	ATCA	1.332	2.93 ± 0.23
" "	" "	1.844	3.25 ± 0.13
" "	" "	2.100†	3.16 ± 0.09
" "	" "	2.356	3.18 ± 0.11
" "	" "	2.868	3.00 ± 0.11
" "	" "	4.732	2.01 ± 0.17
" "	" "	5.244	1.65 ± 0.15
" "	" "	5.500†	1.67 ± 0.08
" "	" "	5.756	1.63 ± 0.16
" "	" "	6.268	1.58 ± 0.17
" "	" "	8.232	1.22 ± 0.19
" "	" "	8.744	1.10 ± 0.16
" "	" "	9.000†	1.08 ± 0.08
" "	" "	9.256	1.11 ± 0.16
" "	" "	9.768	1.09 ± 0.15
" "	" "	16.700†	0.83 ± 0.11
2022 May 16	ATCA	2.100	2.63 ± 0.25
" "	" "	5.500	1.18 ± 0.07
" "	" "	9.000	0.97 ± 0.08

Chapter 4

The radio afterglow of ultra-long gamma-ray burst GRB 220627A

The work in this chapter is being prepared for submission to the Monthly Notices of the Royal Astronomical Society. All the content included in this chapter is my own work, with some parts involving joint contributions from collaborators as described below.

Stefano Giarratana (U. Bologna, INAF/IRA), Om Sharan Salafia (INAF/Brera) contributed to the broader GRB 220627A radio observing campaign detailed in Section 4.3, while Marcello Giroletti (INAF/IRA) contributed to the VLBA observing strategy detailed in Subsection 4.3.4. VLBA observations were reduced independently in both AIPS *and* CASA *by Cormac Reynolds (CSIRO), Cristiana Spingola (INAF/IRA) and myself for independent verification. The version of the VLBA reduction presented here is from the procedure performed jointly by Cormac Reynolds and myself using* AIPS.

Abstract

We present the discovery of the radio afterglow for the most distant ultra-long gamma-ray burst (GRB) detected to date, GRB 220627A. The ultra-long GRB classification follows the rejection of an earlier hypothesis suggesting that GRB 220627A may have been gravitationally lensed; this hypothesis was ruled out after a detailed analysis of its high-energy spectra (Huang et al., 2022). We monitored the radio afterglow from 7 to 45 d post-burst; this enabled us to characterise the phenomenological properties of the radio afterglow and inform our observing strategy for the Very Long Baseline Interferometry (VLBI) observations taken 11 and 12 d post-burst. The observed temporal and spectral properties of the radio afterglow were difficult to explain using the standard forward shock model and may require invoking non-standard model assumptions to explain. Our novel VLBI experiment aimed to provide an independent test of the lensing hypothesis that was free from possible ambiguities from studying the light curves and/or spectra only; in the event of lensing, it would have also provided the lens model necessary for performing time-delay cosmography. However, the results from our VLBI experiment were inconclusive due to insufficient sensitivity and points to several improvements for future experiments, including strategies to minimise trigger latency and a readiness to include high-sensitivity elements and/or longer baselines into the array.

4.1 Introduction

The most striking feature of gamma-ray burst (GRB) 220627A was the presence of two emission episodes, showing similar temporal profiles, separated by ∼15 min in the prompt light curve (Roberts et al., 2022). The initial trigger event on the *Fermi*/Gamma-ray Burst Monitor (GBM) occurred at 21:21:00.09 UT on 2022 June 27 (Fermi GBM Team, 2022). The detection of this prompt counterpart was later confirmed by reports of high-energy detections by the *Fermi*/Large Area Telescope (di Lalla et al., 2022), *Swift*/Burst Alert Telescope (BAT) via the Gamma-Ray Urgent Archiver for Novel Opportunities (GUANO) programme (Raman et al., 2022), *Konus-Wind* (Frederiks et al., 2022), and the *AstroSat* Cadmium-Zinc-Telluride Imager (CZTI) (Suresh et al., 2022). A second trigger event on the *Fermi*/GBM, localised to the same region of the sky, occurred ∼ 15 min later; it was shown that this second burst episode had a similar duration ($T_{90} \approx 127$ s) and burst shape to the first episode ($T_{90} \approx 138$ s). The two immediate competing interpretations proposed for this event were either: (i) a gravitationally lensed GRB event, or (ii) an ultra-long GRB event (Roberts et al., 2022).

A gravitationally lensed GRB event is expected to have clear signatures imprinted on the prompt light: two or more segments of the light curve should show similar temporal and spectral profiles that are indicative of different arrival times for photons from different lensed images due to the different paths traversed. Given that 1 to 4 GRBs are detected every day out to very high redshifts $z \sim 9$ (e.g., Salvaterra, 2015), a small fraction of them are expected to be gravitationally lensed. Their lensing rates are estimated to be approximately 1 in 1000 GRBs (Mao, 1992) or $\sim$0.3 sky^{-1} yr^{-1} (Oguri, 2019). Five bursts, through the identification of feature similarities in different segments of their prompt light curves, have been claimed to be gravitationally lensed: GRBs 950830 (Paynter et al., 2021), 081126A (Lin et al., 2022), 090717 (Kalantari et al., 2021), 200716C (Wang et al., 2021a; Yang et al., 2021) and 210812A (Veres et al., 2021); however, among them, many of these claims have been disputed on statistical grounds (e.g., Mukherjee & Nemiroff, 2023). Lensed GRBs allow the physical properties of the intervening lens to be studied (e.g., Paynter et al., 2021) and for time delay cosmography to be performed, yielding new constraints on cosmological parameters, such as the Hubble parameter (Refsdal, 1964). The lensing interpretation of the GRB 220627A prompt light curve, however, was later proved to be inconsistent with the *Fermi*/LAT[1] data (Huang et al., 2022). In the subsequent analysis of the data, it was shown that the high-energy spectrum of the burst in the first episode was inconsistent with that in the second episode; 49 photons above 100 MeV were detected by *Fermi*/LAT in the first episode compared to none in the second.

This data instead suggested GRB 220627A was the eighth event confirmed in the literature belonging to the subpopulation of ultra-long GRBs. These are GRBs with extremely long durations (> 1 000 s); it is still unclear whether they represent the tail of the standard long GRB duration distribution (Virgili et al., 2013) or a new

[1] *Fermi*/LAT covered the energy range from 20 MeV to 300 GeV (Atwood et al., 2009), compared to the 8 keV to 40 MeV energy range covered by the *Fermi*/GBM (Meegan et al., 2009)

class of GRBs with fundamentally different properties (Boër et al., 2015). Evidence of properties for this subpopulation differing from standard long GRBs have started to emerge over the years. For example, supernova SN 2011kl, associated with ultra-long GRB 111209A, was found to be three times more luminous compared to type Ic supernovae associated with standard long GRBs, while also possessing a very distinct spectrum (Greiner et al., 2015). Radio observations of GRB 130925A revealed a sharp spectral cut off above 10 GHz, suggesting either a mono-energetic electron distribution or very steep electron spectral index ($p \approx 4$, where the electron power law energy distribution is defined as $dN/dE \propto E^{-p}$), which is inconsistent with previously observed properties for standard long GRBs and their radio afterglows (Horesh et al., 2015). To explain the long central engine activity required for ultra-long GRBs, it has been proposed that ultra-long GRB progenitors may involve the core-collapse of low-metallicity blue supergiants (Gendre et al., 2013), with much larger radii than the Wolf-Rayet progenitors of standard long GRBs, or the tidal disruption of compact stars by massive black holes (Levan et al., 2014).

An afterglow for GRB 220627A was also detected in X–ray (Gropp et al., 2022), optical (de Wet et al., 2022; Nicuesa Guelbenzu et al., 2022) and radio (preliminary analysis from our observations was reported in these GCN Circulars; Leung et al., 2022a; Giarratana et al., 2022) wavelengths. Its localisation enabled the spectroscopic redshift measurement of the afterglow at $z = 3.084$, and also the detection of lines from an intervening system at $z = 2.665$ (Izzo et al., 2022).

In this paper, we present the results from our radio observations of GRB 220627A, which also include Very Long Baseline Interferometry (VLBI) observations intended for testing the lensing hypothesis. While the high-energy spectrum in this case had offered sufficient data to disfavour the lensing scenario, VLBI observations offer an independent and direct test of this hypothesis, potentially free from ambiguities from light curve and spectral analysis only. In the case of strong lensing, these observations would enable us to model the lens, which is an important step for using lensed GRB events for time-delay cosmography. In Section 4.2, we give an overview of our ongoing VLBI program for confirming lensed GRB candidates. In Section 4.3, we summarise our radio observations and our data reduction strategies for GRB 220627A, which include the first trigger of our VLBI program for confirming lensed GRB candidates. In Section 4.4, we present the outcomes of our radio observations, including the detection and flux-density measurements of the radio afterglow. We also provide here a discussion of these results, in particular: (i) the unusual phenomenological properties of the GRB 220627A radio afterglow, and (ii) the implications, both challenges and future opportunities, for a VLBI programme targeting the GRB strong lensing phenomenon. Finally, we provide our conclusions in Section 4.5.

In this paper, we assume a flat Λ-CDM cosmology with $H_0 = 67.7\,\mathrm{km\,s^{-1}\,Mpc^{-1}}$, $\Omega_\mathrm{M} = 0.310$, and $\Omega_\Lambda = 0.690$ (Planck Collaboration et al., 2020).

4.2 Imaging Lensed GRB Afterglows with VLBI

In this section we describe our programme to confirm gravitationally lensed GRBs using VLBI imaging and the broader scientific implications of such a detection. GRB 220627A was the first event trigger for this programme.

4.2.1 Strong Gravitational Lensing

If a GRB is strongly gravitationally lensed, multiple images of the GRB would be produced (e.g., Oguri, 2019). In the milli-lensing regime (i.e., the angular separations of the lensed images are ∼milliarcsecond), this gravitational lens signature is superimposed onto the prompt light curve (Blaes & Webster, 1992). Any flux variation from the GRB will appear at different times in the lensed images because the photons travel different path-lengths. Therefore, in a spatially unresolved light curve there would be two pulses (for two lensed images), where the temporal profile of the second pulse should be similar to the first pulse, albeit weaker in intensity. The spectral properties of the two pulses in this scenario should also be similar, i.e., the lens signature is consistent across all energy bands. The time delay between the two pulses can be explained by a combination of both the Shapiro time delay and geometric effects from differing paths traversed by the two rays; it is governed by the relation in (Krauss & Small, 1991):

$$\Delta t = \frac{2GM_z}{c^3}\left[\frac{r-1}{\sqrt{r}} + \ln(r)\right] \text{ s}, \tag{4.1}$$

where $M_z = M(1+z)$ is the redshifted lens mass, r is the brightness ratio of the two lensed images, G is the gravitational constant, and c is the speed of light. This time delay is usually on the order of seconds to minutes for milli-lensing systems (or equivalently, a lens mass of $\sim 10^{5-6}$ $M_\odot$).

Since high-energy satellites have sub-second temporal resolutions, double-pulse prompt light curves have been the basis of various claims (and disputes) of gravitationally lensed GRBs as discussed in Section 4.1. An example shown in Figure 4.1 is the prompt light curve for GRB 220627A from *Konus-Wind*. The two pulses with a flux ratio $r \approx 3$ (as determined by the ratio of the pulse fluences, see Roberts et al., 2022), showing similar temporal profiles across more than one energy band, provided compelling evidence supporting the strong gravitational lensing scenario. However, such observations cannot rule out the possibility that the double-pulse profile may be produced by a physical emission mechanism intrinsic to the GRB (rather than by lensing), or even the possibility that the double-pulse profile does not appear in energy bands outside the observable range of the instrument (as demonstrated by the *Fermi*/LAT data for GRB 220627A).

The smoking gun for a gravitationally lensed GRB would be the detection of two (or more) consistently evolving lensed images of the afterglow with the same surface brightness. The angular separation of the images is on the order of the Einstein radius:

$$\theta_{\rm E} = \sqrt{\frac{4GM}{c^2}\frac{D_{\rm LS}}{D_{\rm L}D_{\rm S}}} \text{ rad}, \tag{4.2}$$

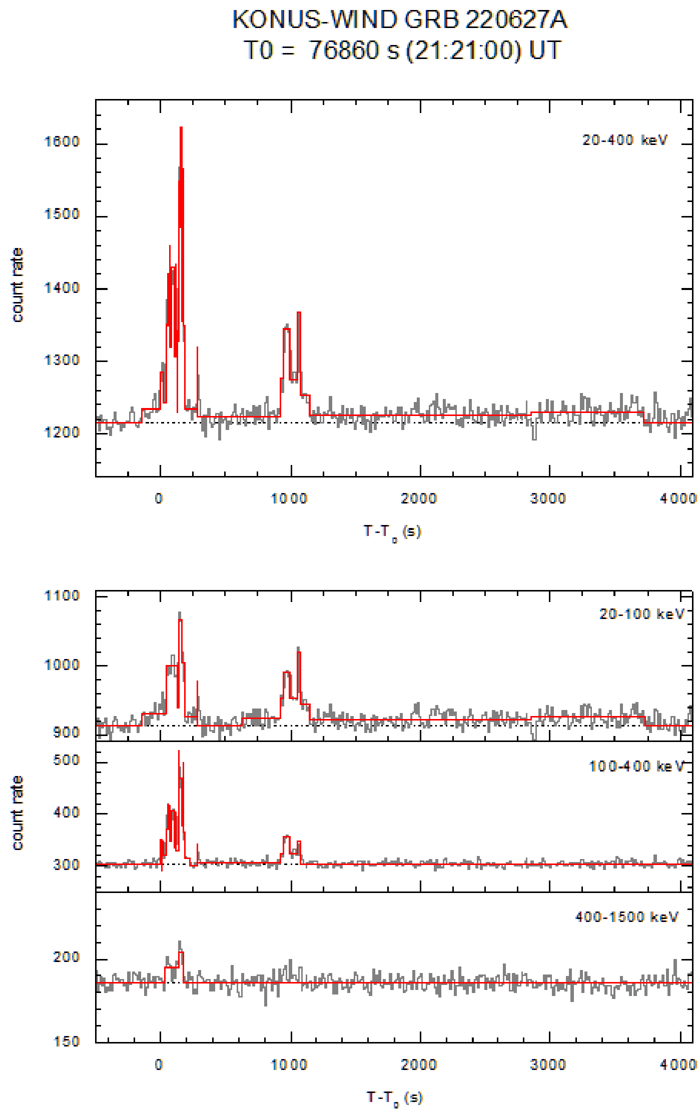

Figure 4.1: The *Konus-Wind* prompt light curve for GRB 220627A, a lensed GRB candidate. The light curves of GRB 220627A across different energy bands show two pulses with similar temporal and spectral profiles; these are necessary properties for any lensing candidate. This image was reproduced from http://www.ioffe.ru/LEA/GRBs/GRB220627A/, which is maintained by the Ioffe Institute Laboratory for Experimental Astrophysics.

where $D_{\rm LS}$, $D_{\rm L}$ and $D_{\rm S}$ are the distances between the lens and the GRB, the distance to the lens, and the distance to the GRB, respectively. For a typical event, with GRB redshift $z_{\rm S} = 1$ and lens redshift $z_{\rm L} = 0.4$, the Einstein radius for a $10^6\,M_\odot$ point mass lens (this is the typical lens mass inferred from previous claims – e.g., Veres et al. 2021; Wang et al. 2021a; Yang et al. 2021 – using Equation 4.1) is $\theta_{\rm E} \approx 3\,{\rm mas}\,(M/10^6\,M_\odot)^{1/2}(D/0.6\,{\rm Gpc})^{-1/2}$, where $D = D_{\rm L}D_{\rm LS}/D_{\rm S}$ (Veres et al., 2021). Specifically for considering GRB 220627A under the lensing hypothesis and by interpreting the redshift of the intervening system reported in Izzo et al. (2022) as the lens redshift, the expected Einstein radius would be $\theta_{\rm E} \approx 1.8\,{\rm mas}$. Considering this typical angular scale expected from lensed GRB systems, direct detection of the two images in the prompt gamma-rays or through standard X-ray/optical/radio afterglow observations would be infeasible. VLBI is currently the only way of reaching the necessary angular resolution for confirming a strongly lensed GRB event.

To confirm a strongly lensed GRB event with VLBI observations, *at least* two epochs are required, and ideally *at least* one of these epochs are observed at two frequencies simultaneously. These allow for a confirmation of lensing by:

- checking for surface brightness preservation between the two lensed images (a necessary signature of gravitational lensing);
- checking for consistency between the spectra of two lensed images (e.g. figure 6 of Katz et al., 1997);
- checking the two lensed images preserve their brightness ratio as they evolve and, aided by complementary low-resolution radio observations, evolve in accordance with known GRB closure relations (e.g., Sari et al., 1998); and
- checking the brightness ratio of the afterglow images matches the ratio of the pulse fluences from the GRB prompt light curve.

The combination of all these checks makes a confirmation robust against potential ambiguities that arise from using one or two checks, such as the possibility of chance spatial association with non-afterglow related sources (e.g., a background host galaxy).

4.2.2 Broader Scientific Implications

The confirmation of a strongly lensed GRB candidate has scientific implications for time-delay cosmography, the physics of the lens and our understanding of GRBs. A confirmation would provide a new example of gravitational lensing to test Einstein's General Relativity, checking for consistency in both the temporal and spatial data. Like other strong gravitational lensed explosive transients, lensed GRBs have important applications in time-delay cosmography; the measured time delay can be used alongside a well-constrained Einstein radius to constrain the Hubble parameter H_0 (Refsdal, 1964). This is a direct consequence of the time delay between the lensed GRB images being dependent on the mass distribution of the lens, which can be modelled from the morphology and distribution of detected components in high-resolution VLBI images, as well as geometric effects from different paths in space-time, which is determined by the Hubble parameter – for a comprehensive review of time-delay cosmography for transients, see Oguri (2019).

As GRBs are found at high redshifts up to $z \sim 9$ (e.g., Salvaterra, 2015) and their light curves (and any time delays) can be sampled accurately down to sub-second temporal resolution (e.g., Meegan et al., 2009), strongly lensed GRBs can probe for lens mass and distance ranges that cannot be probed by strongly lensed quasars and supernovae (since the temporal resolution of the time delay determines the redshifted lens mass range your probe is sensitive to as shown in Equation 4.1). Accompanying previous claims of lensed GRB were suggestions of using them to study the population statistics and physics of their lens (e.g., Paynter et al., 2021). In fact, a confirmation of a lensed GRB would also be the first confirmation of a milli-lens object, which implies the presence of massive compact objects, such as intermediate-mass black holes (IMBH) and dark matter halos (e.g., Spingola et al., 2019; Casadio et al., 2021).

On the other hand, a conclusive rejection of a lensing explanation for a GRB with a double-pulse profile would put extra constraints on the physics of GRB central engines. For example, current GRB models that can explain multiple pulses in the prompt emission would need to be extended to explain how their emission mechanism in some GRBs can produce repeated pulses with similar temporal and spectral profiles. In the specific case of GRB 220627A, the rejection of the lensing hypothesis indicated that the GRB belonged to the subpopulation of ultra-long GRBs.

In Section 4.3, we describe the radio telescopes triggered for GRB 220627A as part of this programme. The Australia Telescope Compact Array (ATCA), MeerKAT, and the Karl G. Jansky Very Large Array (VLA) observations led to the discovery of the radio afterglow and contributed to the monitoring of its evolution over a span of $\sim$40 d. This data informed our trigger of the high-resolution Very Long Baseline Array (VLBA) observations, which aimed to provide an independent test of the lensing hypothesis to verify the conclusions from the high-energy spectra analysis (Huang et al., 2022).

4.3 Observations and Data Reduction

This Section describes the radio observations taken as part of our programme outlined in Section 4.2 and our data reduction for these observations. We collate the flux densities from these radio observations in Table 4.1.

Table 4.1: Radio flux-density measurements for GRB 220627A. Columns 1 through 4 show the number of days since the *Fermi*/GBM trigger (21:21:00.09 UT on 2022 June 27), the observing telescope, the central frequency of the radio image, and the flux-density measurements for the observation. We report the 3σ limit for all non-detections, except for the VLBA observation, where a more conservative 5σ limit is provided instead.

dT (d)	Telescope	ν (GHz)	S_ν (µJy)
7.5	ATCA	5.5	< 93
7.5	ATCA	9.0	< 87
7.5	ATCA	17.9	275 ± 54
8.9	MeerKAT	1.3	< 27
11.7	VLBA	15.2	< 255
27.4	ATCA	5.5	< 60
27.4	ATCA	9.0	< 39
27.4	ATCA	17.7	63 ± 19
35.7	MeerKAT	1.3	< 42
39.0	VLA	6.0	< 39
45.1	VLA	15.1	44 ± 8

4.3.1 ATCA Observations

We observed the field of GRB 220627A with the ATCA, using the coordinates of the reported optical afterglow (de Wet et al., 2022) as the phase tracking centre. We conducted two epochs of ATCA observations, observing the first epoch on 2022 July 5 UT for 10 h and the second epoch on 2022 July 25 UT for 12.5 h, under project C3478 (PI: J. Leung). For both epochs, the observations were observed at multiple bands, centred on 5.5, 9, 17 and 19 GHz, each with a bandwidth of 2 GHz. The array was in H214 configuration for both observations.[2] In this configuration, the maximum baseline is 247 m; this figure does not consider baselines involving antenna CA06 (all of which exceed 4 km) since they were flagged in our data reduction process as discussed below.

We reduced the visibility data using standard MIRIAD procedures (Sault et al., 1995). For both epochs, we used PKS B1934−638 to set the flux-density scale and PKS B1313−333 (J1316−3338) to calibrate the complex gains. To calibrate the bandpass response, we used PKS 1934−638 at the 5.5/9 GHz frequency bands and PKS 0537−441 at the 17/19 GHz frequency bands. Prior to imaging, we flagged out all the baselines involving antenna CA06. This was because the large gap in (u, v)-coverage between these longer baselines and the other much shorter baselines in the array created difficulties in the imaging process (due to the highly irregular shape of the resulting dirty beam). We produced images using the multi-frequency synthesis CLEAN algorithm (Högbom, 1974; Clark, 1980; Sault & Wieringa, 1994) and extracted flux densities in the case of a detection by fitting a point-source model in the image plane. The 17 and 19 GHz frequency bands were imaged together, providing a contiguous bandwidth of 4 GHz centred on 18 GHz. The flux densities (and 3σ upper limits for non-detections) are reported in Table 4.1. The rms noise in all bands was higher in the first observation, compared to the second, due to poor weather conditions.

4.3.2 MeerKAT Observations

MeerKAT observations of GRB 220627A were carried out on 2022 July 6 UT and 2022 August 2 UT (Giarratana et al., 2022). These observations were centred on 1.28 GHz (L band), with a bandwidth of 0.78 GHz, and yielded non-detections. The 3σ non-detection limits are given in Table 4.1.

4.3.3 VLA Observations

We obtained observations for GRB 220627A with the VLA at two separate epochs, with 1 h of observation time per epoch, under project VLA/22B-031 (Legacy ID: AL1245; PI: J. Leung). The first epoch of observations occurred on 2022 August 5 at the central frequency of 6 GHz (C band), while the second occurred on 2022 August 11 at the central frequency of 15 GHz (Ku band). For both observations,

[2] https://www.narrabri.atnf.csiro.au/operations/array_configurations/configurations.html

the array was in the D configuration,[3] with a maximum baseline of 1 km. For each observation, we used 3C 286 to calibrate the bandpass response and flux-density scale, and PKS B1313−333 (J1316−3338) to calibrate the complex gains.

Prior to imaging, we obtained the pipeline-calibrated[4] visibility data from the data archives (see Data Availability section). We used CASA (McMullin et al., 2007; CASA Team et al., 2022) to verify the quality of the pipeline-calibrated data and also to image the field using the wide-field, multi-frequency synthesis CLEAN algorithm. For the 2022 August 5 observation (at 6 GHz), after accounting for antennas under maintenance and antennas flagged by the automated pipeline, the imaging process used data from only 21 antennas; for the 2022 August 11 observation (at 15 GHz), the imaging process used data from 22 antennas. Further self-calibration was not performed for either observation since weak field sources in addition to the presence of poorly-modelled extended sources led to limited improvements in the gain solutions. Due to the presence of imaging artefacts caused by the sidelobes of a bright, extended source outside the primary beam, PKS J1325−3236, we phase rotated the 2022 August 5 (6-GHz band) visibility data to J2000 13:25:32.8,−32:30:45 before imaging so we could deconvolve both the target and PKS J1325−3236 in our CLEAN cycles. We imaged the 2022 August 5 observation with the full 4 GHz bandwidth, centred on 6 GHz, and the 2022 August 11 observation with the full 6 GHz bandwidth, centred on 15 GHz. In the case of a detection, we extracted the flux densities by fitting a point-source model in the image plane and report them in Table 4.1 (for non-detections, we give the 3σ upper limit).

4.3.4 VLBA Observations

We obtained high-resolution observations for GRB 220627A with the VLBA on two consecutive days under project VLBA/22B-032 (Legacy ID: BL296; PI: J. Leung). These observations were 6 h in duration, starting at 22:30 UT on both 2022 July 8 and 9. All standard VLBA antennas,[5] with the exception of the Kitt Peak station which was out due to wildfires, were available for both observations. The longest baseline was from Mauna Kea to Saint Croix, giving a projected baseline of ∼8 600 km or ∼430 Mλ. For these observations, the VLBA was configured to use the digital downconverter (DDC) observing system, observing at the central frequency of 15.168 GHz (Ku band), with a total bandwidth of 512 MHz (split into four 128 MHz sub-bands) in two circular polarisations (right- and left-circular polarisations). Using a 2-bit sampler, the resulting data rate was 4 Gbps. The data was correlated after the observations using DiFX (Deller et al., 2007) with an integration time of 1 s and a spectral resolution of 1 MHz at Socorro, New Mexico, USA.

[3] For more information on VLA configurations, see: https://public.nrao.edu/vla-configurations/

[4] All VLA data is calibrated by an automated CASA pipeline (Kent et al., 2020). For more information, see: https://science.nrao.edu/facilities/vla/data-processing/pipeline

[5] The standard array of antennas consists of 10 stations, see: https://science.nrao.edu/facilities/vlba/docs/manuals/oss/sites

We carried out standard reduction procedures on the correlated datasets from both observations simultaneously using AIPS (Greisen, 2003). The instrumental delays were determined using the fringe finders J0555+3948 and J1642+3948. The latter was also used for solving the bandpass. Since the expected flux density of our target, GRB 220627A, was < 0.5 mJy as informed by our earlier ATCA observations, we phase-referenced our experiment using the calibrator J1324−3235, which was observed in 45 s scans as part of 100 s duty cycle. Although this calibrator had a low unresolved flux-density measurement at 8.6 GHz (50 mJy), it was chosen due to its close separation (0.32°) from the target position, which was particular important given the low elevation of the source with respect to the VLBA antenna stations. To attain better signal-to-noise, we combined all the sub-bands during our global fringe fitting process on the fringe finders and phase-reference calibrators in order to solve for the residual phases, delays, and rates. The solutions from the phase-reference calibrator were interpolated to both the target and our check source, PKS B1313−333 (J1316−3338), located 1.75° away from the target. Finally, we used Difmap (Shepherd, 1997) with a natural weighting scheme to obtain the final images of both the target and the check source. The resulting image had a beam size of 0.49 mas × 1.51 mas with a position angle of −5.4°.

In our VLBA observations, we were unable to identify any sources that were related to the GRB 220627A event within the optical (de Wet et al., 2022) and radio (from our ATCA/VLA detections) positional uncertainties. The final target image achieved a rms sensitivity of 51 µJy beam^{-1} and no noise peaks exceeded the 5σ level (i.e., $\sim$250 µJy beam^{-1}). After performing self-calibration iterations on the check source (located further from the phase-reference calibrator than the target), we found that the phase errors were no more than $\sim$10° for most antennas, suggesting that possible problems with phase transfer were not responsible for the non-detection. The 5σ upper limit is reported in Table 4.1.

4.4 Results and Discussion

4.4.1 Unusual Phenomenology of the Radio Afterglow

The radio light curve and spectral energy distribution (SED) for GRB 220627A are plotted in Figure 4.2 *left* and *right* panels, respectively. In all three spectral snapshots (at 8, 27, and 40 d post-burst), the radio spectrum appears to be self-absorbed, with the spectrum peaking at frequencies higher than those sampled in our observing campaign. As a result, we only detected the radio emission at the 15 and 18 GHz observing bands. For the first epoch in particular, measuring the spectral slope of the radio source from the 9 GHz limit to the 18 GHz detection, we constrain $\alpha > 1.7$, where $S \propto \nu^{\alpha}$, at these early times. If we assume the radio emission detected in each epoch is from the same source, the radio source decays with a $t^{-0.9\pm0.2}$ dependence in the 15–18 GHz frequency range. This assumption may not be true, if, for example, the radio emission detected at the second and third epochs is from the host galaxy, in which case, the temporal decay of such a radio afterglow, detected in the first epoch, is even steeper.

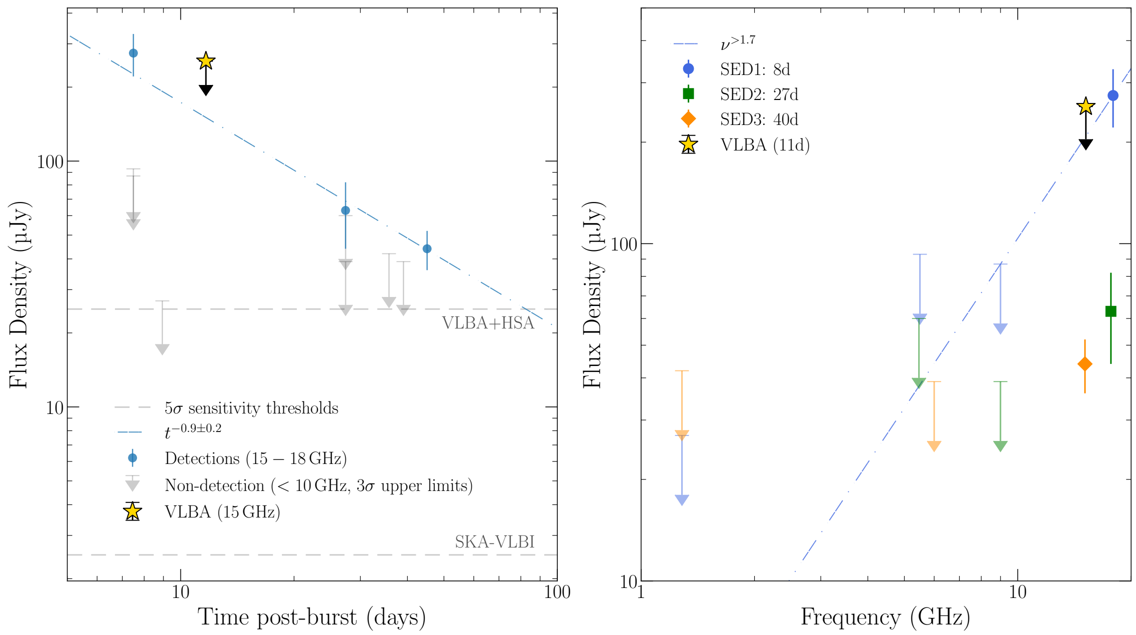

Figure 4.2: ***Left:*** Radio light curve for GRB 220627A. The radio light curve shows the 15–18 GHz detections (blue circular markers), which were fit with a power law (blue dash-dotted line) to obtain a temporal index. A 3σ upper limit is used for all non-detections (grey arrows), with the exception of the VLBA observation, where a 5σ upper limit is used instead (yellow star and arrow). The dashed lines represent the 5σ sensitivity thresholds expected for the VLBA+HSA and SKA-VLBI arrays (in 10 and 1 h of integration, respectively). ***Right:*** Radio SED for GRB 220627A. The radio SED plot shows different spectral snapshots of the radio afterglow: SED1 approximately at 8 d post-burst (blue circular markers), SED2 approximately 27 d post-burst (green square markers), and SED3 approximately 40 d post-burst (orange diamond markers). All non-detections are coloured by their observing epoch, but are represented by arrows representing the 3σ upper limit. The 18 GHz detection and 9 GHz non-detection limit were fit with a power law (blue dash-dotted line) to obtain a lower limit on the spectral index at the first epoch of observations (SED1, 8 d post-burst). The details of each radio data point are summarised in Table 4.1.

The detections in the last two epochs, when accounting for the uncertainties, are consistent with a lack of variability, which may be expected in a host galaxy. However, we argue it is unlikely to be emission from the host given synchrotron emission due to star formation expected from the host galaxy is likely to be optically thin at radio frequencies rather than optically thick as we observe in our scenario (Condon, 1992); it is also unlikely to be thermal dust emission redshifted from the millimetre host spectrum (as it is usually quite attenuated at this corresponding rest frame frequency), but we cannot entirely rule out this possibility. Using the redshift $z = 3.084$ and our maximum flux-density measurement at 18 GHz, we find that the peak radio luminosity of the afterglow to be $\nu L_\nu \gtrsim 6 \times 10^{40}\,\mathrm{erg\,s^{-1}}$, which is consistent with the wider long GRB population (e.g., see Figure 9 in Ho et al., 2020a).

However, the observed temporal and spectral behaviours are still difficult to explain in the standard afterglow model. As $\nu < \nu_\mathrm{a}$ or $\nu < \nu_\mathrm{m}$ for all our observing epochs, where ν is our observing frequency, ν_a is the self-absorption frequency, and ν_m is the peak synchrotron frequency, the only scenario where a temporal decay is predicted to be observed in this regime is when $\nu_a < \nu < \nu_m$.[6] In particular, this is predicted only after accounting for the geometry of the jet (as opposed to assuming an isotropic blast wave), which is significant when the jet has slowed down and started to spread laterally (e.g., Sari et al., 1999). The forward shock model accounting for the jet geometry in Sari et al. (1999) predicts the flux density could decay as $t^{-1/3}$ when $\nu_a < \nu < \nu_m$, which is still somewhat flatter and incompatible with the steeper $t^{-0.9\pm0.2}$ that is observed in our data. A possibility that can produce a steeper slope, is for the the synchrotron peak ν_m to have moved between the 9 and 17 GHz observing bands, but this is an unlikely possibility. A multi-wavelength model may provide further avenues of explaining the peculiar observed radio behaviours under the standard afterglow model, but this is beyond the scope of this thesis chapter. Previous radio observations of ultra-long GRBs, such as GRB 130925A, were also unable to be explained under the standard afterglow model and required alternative assumptions on the synchrotron electron distributions (Horesh et al., 2015).

4.4.2 VLBI Test of the GRB 220627A Lensing Scenario

Our VLBA experiment aimed to provide an independent test of the lensing scenario for GRB 220627A (i.e., independent of the conclusions drawn from the analysis of the high-energy spectra; Huang et al., 2022). Using the temporal and spectral scalings determined in Subsection 4.4.1, we interpolated our low-resolution, multi-frequency ATCA measurements (at 5.5/9/18 GHz, taken 7.5 and 27.4 d post-burst) in both the frequency and temporal domains to estimate the unresolved flux density at the time and frequency of our VLBA observation (15 GHz, 11.7 d post-burst); this was estimated to be ~120 µJy. This suggests that in the ultra-long GRB (non-lensing) scenario, we should expect a compact radio source at ~120 µJy, and in the lensing scenario, two compact sources at even dimmer flux-density levels of ~30 and ~90 µJy (as determined by their gamma-ray fluence brightness ratio $r \approx 3$). As reported in Subsection 4.3.4, our VLBA observations yielded a non-detection down to a 5σ limit of ~250 µJy beam^{-1} (within the uncertainty region of lower-resolution optical and radio detections, there were multiple noise peaks at, but not exceeding, this 5σ level). This means we were unable to claim a detection or a non-detection of an afterglow source (or any source) at the ~250 µJy level; the lensing and ultra-long GRB scenarios could not be distinguished so our VLBI experiment yielded a non-conclusive result.

This experiment was the first time VLBI was used to search for the multiple images of a candidate strongly gravitationally lensed GRB afterglow. The only lensed GRB candidate that had VLBI follow-up prior to this event was GRB 200716C (Giarratana et al., 2023). For that event, as the afterglow had faded by the time of the observation, the European VLBI Network (EVN) and *e*-Merlin was used to search the candidate host galaxy for a possible IMBH that could act as the lens, rather than directly for the multiple images of the afterglow. Their non-detection

[6] The steep spectral slope in our first epoch shows that the observing frequency is located below the self-absorption frequency $\nu < \nu_a$, but the limit on the spectral index is relaxed in subsequent epochs as the flux density decreases at the 15–18 GHz bands, allowing for the possibility that $\nu_a < \nu < \nu_m$.

(at $< 50\,\mu$Jy beam^{-1} rms) also yielded an inconclusive result, unable to confirm the presence of a possible IMBH lens in the candidate host galaxy. These results highlight the difficulty of such an experiment and the need for improvements in future programmes. Below, we evaluate the outcomes of our VLBI campaign for GRB 220627A and discuss possible improvements that can be implemented in the areas of angular resolution, sensitivity, and trigger timing.

Our resulting VLBA image had a synthesised beam size of 0.49 mas × 1.51 mas. In Figure 4.3, we show the expected Einstein radius for GRB 220627A in the lensing scenario as a function of the lens redshift, calculated using Equations 4.1 and 4.2, compared to our major-axis beam size. With the major-axis beam size being smaller than the expected Einstein radius out to $z \approx 2.8$ (n.b., $z_{\rm GRB} = 3.084$), our VLBA observations had sufficient angular resolution to resolve the lensed images for much of the lens redshift parameter space. As an intervening absorber was identified at $z = 2.665$ via the presence of S IV, Si II, C IV, Fe II, Al II lines in the optical spectrum (Izzo et al., 2022), we considered this system the likely location of the lens during our radio campaign. At this redshift, the Einstein radius would be $\theta_{\rm E} \approx 1.8$ mas, so the two distinct lensed images of the afterglow (in the lensing scenario) would have been resolved by our VLBA observations. However, in the extreme scenarios, where the lens redshift is greater than $z_{\rm L} \approx 2.8$, the lensed images may overlap. In this scenario, the lensed event may still be confirmed by modelling a multi-component source, but this may be at the expense of accuracy in both the astrometry and source structure, which are critical for modelling of the lens (and by extension, time-delay cosmography). Future improvements to the programme should include the optionality to add longer baselines to the array, thereby improving the resolution; for example, adding EVN telescopes like Effelsberg to the VLBA to improve East-West (u, v)-coverage, or similarly, adding the East-Asian VLBI Array to the Long Baseline Array in Australia to improve North-South (u, v)-coverage.

The more critical aspect for the GRB 220627A VLBI experiment pertains to sensitivity as this was the limiting factor that led to the non-conclusive outcome. Two factors in particular need to be considered: the instrumentation and the brightness ratio in the scenario where the lensed images can be resolved. As shown in Subsection 4.4.1 (and in Figure 4.2, *right*), the radio spectrum below ∼15 GHz was self-absorbed. This meant that the Australian LBA could not be triggered, despite its advantageous geographic position,[7] because their optimal observing frequency is centred at 8.4 GHz (above which their receivers are significantly less sensitive). The VLBA was well-equipped to observe at 15 GHz, but for our scenario, the observations were hindered by shorter integration times (with the source above the horizon for ∼6 h per day, c.f. ∼14 h per day for the LBA) and greater levels of atmospheric seeing ($< 30°$ elevation through the entire observation for most antennas due to the low Declination). The resulting image reached a rms sensitivity of $51\,\mu$Jy beam^{-1} (after combining two consecutive days of observations). This sensitivity, as previously discussed, was insufficient to distinguish between the lensing and ultra-long GRB scenarios (as it does not reach the sensitivity level required to make a detec-

[7] GRB 220627A is located at a Declination of −32°, while most LBA stations are located between a latitude of −30° and −40°.

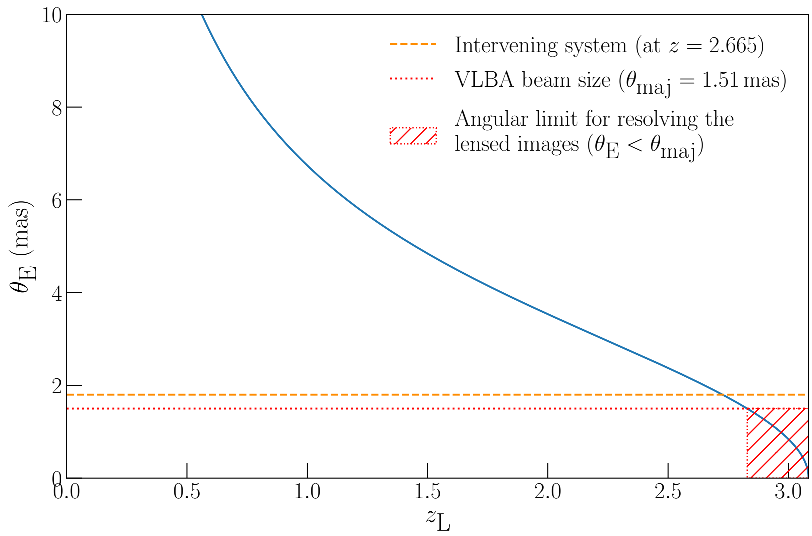

Figure 4.3: We show the Einstein radius θ_{E} as a function of the lens redshift z_{L} for GRB 220627A (blue solid line). We also show the expected Einstein radius for a lens located at the redshift $z = 2.665$ (orange dashed line), which was the redshift of the intervening system identified in the optical spectrum (Izzo et al., 2022). For comparison, we compare these to our VLBA major-axis beam size θ_{maj} (red dotted line), showing that only a small part of the parameter space is beyond the angular limit of our observation (red hatched region).

tion of the unresolved afterglow). With a lensing brightness ratio of $r \approx 3$ (more typically $r \approx 2$ from previous claims of GRB lensing candidates), the sensitivity requirements in the lensing scenario for detecting both lensed images would be at least four times more severe than those required for only detecting the unresolved (and magnified) afterglow.

Our programme to confirm and study the properties of lensed GRB afterglows with VLBI serves as a pathfinder project for the SKA-era of radio astronomy. While the programme today is quite sensitivity limited, VLBI in the SKA-era is expected to reach rms sensitivities of $\sim$0.05 µJy beam^{-1} in 1 hr of integration (e.g., Paragi et al., 2015). With this level of sensitivity, the SKA-era VLBI array should be able to make strong detections of the lensed images for the majority of GRBs regardless of their redshift, even if their afterglows are self-absorbed at the observing frequency (see figure 2 in Leung et al., 2021a). However, since the SKA telescope will not be operating likely until the next decade, our pathfinder programme needs other ways to improve instrumental sensitivity in the future triggers to successfully achieve its science goals. The main method for achieving this would be to ensure the trigger proposals have the option to add high-sensitivity telescopes to the array when the sensitivity requires it. For example, for GRB 220627A, if the observations had included the High Sensitivity Array (HSA), consisting of the Green Bank Telescope and the phased Very Large Array, our observations would have achieved a rms sensitivity[8] of ∼5 µJy beam^{-1}. This rms sensitivity would enable ∼6σ and ∼18σ detections of the two resolved lensed images in the lensing scenario, or a ∼24σ detection of an unresolved afterglow in the non-lensing, i.e., the ultra-long GRB afterglow (see Figure 4.2, *left*); this would have provided sufficient sensitivity for testing the lensing hypothesis.

Besides instrumental sensitivity, the other aspect that will determine the signal-to-noise of any detection is the intrinsic brightness of the afterglow, which relates to the light curve evolution and timing of an programme trigger. As most radio afterglows decay on the timescale of a few weeks (e.g., Chandra & Frail, 2012), both the initial low-resolution and subsequent VLBI observations need to be triggered in a timely manner when an event occurs. If the GRB is able to observed in a timely manner near the radio peak, the typical 10–30 µJy rms sensitivity that the VLBA/LBA is able to achieve in a 10 hr observation without high-sensitivity telescopes in the array is sufficient for detecting the lensing signature for ∼75% of all expected events with a radio-loud counterpart (i.e., those with integrated flux density reaches down to ∼200 µJy; Chandra & Frail, 2012). In the case of GRB 220627A, the LBA was planned to be triggered a day after the ATCA observation if there was a detection at 9 GHz; but the self-absorbed spectrum led to a non-detection, and the detection instead at higher frequencies requiring the VLBA instead led to a 4-day delay in the trigger. The delay corresponded to a ∼60 µJy reduction in flux density, or a 33% reduction in signal-to-noise. We also note that our initial flux-density measurement reported in Leung et al. (2022a) of ∼400 µJy at 17 GHz was inflated due to an incorrect flux-density scaling that has since been corrected; this led us to trigger the VLBA with an expected rms sensitivity of 30 µJy beam^{-1} despite the instrument not having sufficient sensitivity to distinguish the lensing and ultra-long GRB scenarios.

Our GRB 220627A campaign therefore emphasises the requirement for future programmes to have a quick trigger turnaround time as well as the option to include high-sensitivity telescopes in the array, where possible. With event rates estimated to be as low as one every three years (Oguri, 2019), it is critical to ensure these requirements are met to maximise the science output of a gravitationally lensed GRB event. For example, one successful VLBI campaign for such an event would lead to the first confirmation of lensed GRB event (also the first milli-lens), provide a model for the lens, and also an estimate for the Hubble parameter, H_0. Assuming a typical event with the lensed images observed with an astrometric uncertainty of ∼100 µas, H_0 could be obtained to a 10% precision (e.g., equation 17 in Birrer & Treu, 2019); 20 to 30 such events (inclusive of other non-GRB explosive transients and variables) would enable a similar precision, and with different systematics, to other cosmology experiments (e.g., Verde et al., 2019).

[8]The HSA usually also includes Effelsberg, but this station does not operate at our Ku observing band. The estimated rms sensitivity reached by including the HSA was calculated here using the online tool maintained by Benito Marcote: https://planobs.jive.eu/

4.5 Conclusions

We have conducted a radio campaign to study the afterglow of GRB 220627A, an ultra-long GRB that was originally classified as a potential lensed GRB candidate. Our radio campaign led to the discovery of the radio afterglow 7 d post-burst and we continued monitor it at multiple frequencies until 45 d post-burst. We found that the steep temporal decay was difficult to reconcile with the self-absorbed spectrum under the standard afterglow model, indicating that the observed properties of the radio afterglow may require non-standard model assumptions to explain.

While the lensing interpretation for this GRB was already ruled out by after a detailed analysis of its high-energy spectra (Huang et al., 2022), we used VLBI as part of our radio campaign in an attempt to provide an independent verification of this conclusion in a way that was free from possible ambiguities from studying the light curves and/or spectra only. This experiment was the first time VLBI was used to search for the multiple images of a candidate strongly gravitationally lensed GRB afterglow. However, the results from our VLBI experiment were inconclusive due to insufficient sensitivity and points to several improvements required for future experiments, including strategies to minimise trigger latency and readiness to include high-sensitivity elements and/or longer baselines into the array.

Acknowledgements

The Australia Telescope Compact Array is part of the Australia Telescope National Facility (https://ror.org/05qajvd42) which is funded by the Australian Government for operation as a National Facility managed by CSIRO. We acknowledge the Gomeroi people as the Traditional Owners of the Observatory site. The National Radio Astronomy Observatory is a facility of the National Science Foundation operated under cooperative agreement by Associated Universities, Inc. This work made use of the Swinburne University of Technology software correlator, developed as part of the Australian Major National Research Facilities Programme and operated under licence.

Data Availability

The ATCA data can be accessed through the Australia Telescope Online Archive[9] under the project code C3478. The VLA and VLBA data can be accessed through the NRAO Archive Interface[10] under project codes VLA/22B-031 and VLBA/22B-032, respectively. Reasonable requests for other auxiliary datasets can be accommodated for via email to the corresponding author.

[9] https://atoa.atnf.csiro.au

[10] https://data.nrao.edu

Chapter 5

Conclusions and Future Outlook

For the past two decades, efforts to use wide-field radio surveys for GRB studies have been limited by instrumental sensitivity (e.g., Levinson et al., 2002; Gal-Yam et al., 2006; Mooley et al., 2016). Improvements driven by the development of pathfinder technologies for SKA-era telescopes have since made drastic improvements on this front. This thesis has shown for the first time wide-field radio surveys are now sensitive enough to contribute to the detection and the study of GRB afterglows. This opens the door to many opportunities; for example, wide-field surveys would provide valuable contributions towards monitoring GRB events with unexpected late-time radio emission, such as supernova-powered rebrightening events (e.g., Barniol Duran & Giannios, 2015) and kilonova afterglows (e.g., Nakar & Piran, 2011), finding and characterising orphan afterglows (e.g., Law et al., 2018), localising GRB as well as gravitational wave events with poor localisation regions (e.g., Dobie et al., 2019), and constraining the fraction of GRB systems that may lead to the formation of a superamassive neutron star (e.g., Beniamini & Lu, 2021). When complemented with multi-frequency, multi-scale observational data, they provide a more complete understanding of the GRB phenomena.

This thesis has highlighted the opportunities and challenges that recent and upcoming advances in radio interferometry brings for answering important open questions about GRBs and their afterglows. I recap below the key conclusions from this thesis and the future outlook continuing from this work.

In Chapter 2, I presented the results from a targeted search for radio emission from long GRB afterglows located in the RACS footprint. I showed the resulting detection of late-time radio emission from the low-luminosity GRB 171205A, the first confirmed detection of a radio afterglow in a wide-field radio survey. The detection paved the way for a multi-frequency late-time radio monitoring campaign, which helped to constrain the microphysical parameters of the GRB and reveal a circumburst environment consistent with one shaped by pre-explosion stellar winds.

The unexpected discovery of radio emission from GRB 171205A has enabled a late-time multi-frequency, multi-scale monitoring campaign. With the late-time monitoring campaign, we are able to study the GRB blast wave deep into the Newtonian regime, allowing us to perform calorimetry independent of inclination angle effects and also to study the mass-loss history of the progenitor. Given the proximity of the event, late-time VLBI observations following the detection provide significant constraints on the viewing angle and/or source expansion. These observations are the focus of future publications.

In Chapter 3, I described a novel matched-filter approach to finding orphan afterglows in the multi-epoch radio survey, VAST-P. This matched-filter search was motivated by the slow evolution of GRB 171205A at gigahertz frequency; this is because radio transient searches using traditional variability metrics struggle to recover sources whose evolution timescale is significantly longer than the survey cadence. The matched-filter search yielded five candidates, including one synchrotron transient candidate, VAST J175036.1−181454, which I interpreted as either a likely off-axis GRB or tidal disruption event.

All five candidates would not have been recovered in traditional variability searches at the 3σ level, pointing to the need for complementary strategies in future searches for extragalactic transients in wide-field radio surveys. If VAST J175036.1−181454 is interpreted to be a GRB, the beaming fraction (and implied jet opening angle) is consistent with what is expected from previous studies. VAST J175036.1−181454 is the target of an ongoing follow-up programme, involving the addition of low-frequency and high-resolution radio facilities, high-energy follow-up as well as spectroscopic observations. The goal of this programme is to definitively classify and better characterise the transient; the results from this programme are the focus of future publications.

In Chapter 4, I discussed the radio observing campaign for ultra-long GRB 220627A, which was initially identified as a possible gravitationally lensed GRB candidate. While the high-energy spectrum in this case was sufficient for disfavouring the lensing scenario, VLBI observations provide an independent and direct test of the lensing hypothesis, potentially free from any ambiguities that may arise from light curve and spectral analysis only. The high-resolution observations in my GRB 220627A radio campaign was the first attempt at confirming a gravitationally lensed GRB candidate using VLBI while the radio afterglow was still detectable. The VLBI observations, however, were inconclusive, partly due to insufficient sensitivity, but the wider observing campaign helped to characterise the properties of the ultra-long GRB radio afterglow, of which only a handful have been previously studied.

The continuation of our triggered programmes on global VLBI facilities will be scientifically critical in the event of a gravitationally lensed GRB event. Such observations would allow us to model the lens, which is an important step for using lensed GRB events for time-delay cosmography (to estimate the Hubble parameter; Refsdal, 1964), and provide a definitive confirmation for any lensed events, which would be a significant breakthrough as no milli-lenses have previously been confirmed. These events are exceptionally rare, with early estimates suggesting approximately one event every three years (e.g., Oguri, 2019). Learning from our experience with GRB 220627A, a campaign with minimal trigger latency and a readiness to include higher sensitivity telescopes in the arrays, where possible, would be ideal for maximising the science from these rare, yet impactful, events.

This thesis has given some insight into the opportunities that the coming era of radio astronomy can bring to GRB science (and more generally, radio transients science). I have demonstrated that the current generation of radio surveys are now sensitive enough to detect the brightest and closest radio afterglows. In the near future, shallow surveys conducted by the SKA, for example, expected to reach sub-µJy sensitivity with daily cadence (Dewdney et al., 2009; Fender et al., 2015), would improve greatly on our current capabilities. For example, the power of these instruments would allow for: an unbiased radio follow-up of all GRBs, the ability to localise bursts with large error regions, the characterisation of the off-axis GRB population, and by extension, the typical jet geometry of the GRBs.

Equally as important are the challenges that may present themselves, for example: the efficient and timely processing of large datasets, the ability to identify transients from the abundance of non-varying sources, and the ability to distinguish between different classes of transients in multi-epoch data. This thesis has explored some early ideas for combating a selection of these challenges. I have demonstrated the need for alternative transient identification approaches, such as the use of matched-filters, discussed the usefulness of infrastructure that can provide both complementary archival and contemporaneous multi-wavelength data, and emphasised the necessity of having an optimised trigger strategy for different events and/or science cases. Our success in the SKA-era of radio astronomy yet to come therefore lies in our preparation for it.

"The Universe is crazy, always. You should know, since you study those damn crazy sources called GRBs!"

— Om Sharan Salafia

Appendix A

General Coordinates Network

I reproduce below the General Coordinates Network (GCN) Circulars I have published as part of this PhD thesis.

GCN 27812

```
TITLE: GCN CIRCULAR
NUMBER: 27812
SUBJECT: GRB 171205A: ATCA observations of late-time radio emission
DATE: 20/05/25 04:50:43 GMT
FROM: James Leung at U of Sydney/VAST <jleu9465@uni.sydney.edu.au>

James Leung (University of Sydney/CSIRO), Tara Murphy (University of
Sydney), Emil Lenc (CSIRO), Dougal Dobie (University of Sydney/CSIRO),
David Kaplan (UWM)

We have performed two observations for GRB 171205A (V. D'Elia et al.,
GCN Circ. 22177) centred on the optical afterglow position (L. Izzo et
al., GCN Circ. 22180) with the Australia Telescope Compact Array (ATCA).
The observations took place on 2020 April 12 (859 days post-burst) and
2020 May 7 (884 days post-burst) at several frequencies. We report the
detections and 3-sigma limits below:

Date (UTC) | Freq (GHz) | Peak Flux Density (micro-Jy/beam)
-----------------------------------------------------------
2020/04/12 | 2.1 | 708 +/- 253
2020/04/12 | 5.5 | 412 +/- 47
2020/04/12 | 9.0 | 252 +/- 27
2020/04/12 | 16.7 | 112 +/- 38
2020/04/12 | 21.2 | < 87
2020/05/07 | 2.1 | 816 +/- 287
2020/05/07 | 5.5 | 440 +/- 52
2020/05/07 | 9.0 | 237 +/- 26
2020/05/07 | 16.7 | 133 +/- 50
2020/05/07 | 21.2 | < 122

We thank CSIRO staff for supporting these observations during these
especially difficult times.
```

GCN 29640

TITLE: GCN CIRCULAR
NUMBER: 29640
SUBJECT: GRB 171205A: Continued ATCA observations
DATE: 21/03/10 08:47:32 GMT
FROM: James Leung at U of Sydney/VAST <jleu9465@uni.sydney.edu.au>

James Leung (University of Sydney/CSIRO), Emil Lenc (CSIRO), Tara Murphy (University of Sydney), Giancarlo Ghirlanda (INAF/Brera), Ziteng Wang (University of Sydney/CSIRO)

We have been monitoring the late-time radio emission of GRB 171205A (V. D' Elia et al., GCN Circ. 22177) centred on the optical counterpart position (L. Izzo et al., GCN Circ. 22180) with the Australia Telescope Compact Array (ATCA). The observations took place on 2021 March 7 (1171 days or 3.21 years post-trigger) at 2.1, 5.5 and 9.0 GHz frequencies. We report the detections below:

Date (UTC)	Freq (GHz)	Peak Flux Density (micro-Jy/beam)
2021/03/07	2.1	554 +/- 92
2021/03/07	5.5	293 +/- 35
2021/03/07	9.0	179 +/- 28

Ongoing observations are planned.

We thank CSIRO staff for supporting these observations during these especially difficult times.

GCN 30324

TITLE: GCN CIRCULAR
NUMBER: 30324
SUBJECT: GRB 150428A: late-time radio observations
DATE: 21/06/26 13:58:18 GMT
FROM: James Leung at U of Sydney/VAST <jleu9465@uni.sydney.edu.au>

James Leung (University of Sydney/CSIRO), Poonam Chandra (NCRA-TIFR), Emil Lenc (CSIRO), Tara Murphy (University of Sydney), Ziteng Wang (University of Sydney/CSIRO)

ASKAP J123409+065712 is a radio source found in a search of Australian Square Kilometre Array Pathfinder (ASKAP) data (SB10736). The radio source position is consistent with the enhanced Swift-XRT position (Osborne et al., GCN Circ. 17768) and inconsistent with the GROND source position (Knust et al., GCN Circ. 17767).

We conducted further observations of the radio source with the Australia Telescope Compact Array (ATCA) and the upgraded Giant Metrewave Radio Telescope (uGMRT). We summarise these observations in the table below.

Date (UTC)	Telescope	Freq (GHz)	Peak Flux Density (uJy/beam)
2019/12/05	ASKAP	1.4	363 +/- 56
2021/05/21	ATCA	5.5	94 +/- 26
2021/06/13	uGMRT	1.3	386 +/- 17

The fitted position of the radio source from the uGMRT observation is
RA: 12:34:09.296
Dec: +06:57:13.83

Observations of the radio source do not show any evidence for fading in epochs separated by 555 days and we therefore conclude the source is likely the host galaxy of GRB 150428A.

We thank CSIRO and GMRT staff for supporting these observations during these especially difficult times.

GCN 32341

TITLE: GCN CIRCULAR
NUMBER: 32341
SUBJECT: GRB 220627A: ATCA detection of radio counterpart
DATE: 22/07/07 14:26:05 GMT
FROM: James Leung at U of Sydney/VAST <jleu9465@uni.sydney.edu.au>

James Leung (U. Sydney, CSIRO), Ziteng Wang (U. Sydney, CSIRO), Tao An (SHAO), Adam Deller (Swinburne), Giancarlo Ghirlanda (INAF/Brera), Stefano Giarratana (U. Bologna, INAF/IRA), Marcello Giroletti (INAF/IRA), David L. Kaplan (UWM), Emil Lenc (CSIRO), Tara Murphy (U. Sydney), Lauren Rhodes (U. Oxford), Om Sharan Salafia (U. Milano-Bicocca, INAF/Brera), Cristiana Spingola (INAF/IRA)

The Australia Telescope Compact Array (ATCA) observed GRB 220627A (Fermi GBM team, GCN Circ. 32278) at multiple frequencies starting at 04:00 UT on 2022 July 5 (7.3 days post-burst). We detected a radio source with a preliminary flux density of 0.4 mJy at a central frequency of 17 GHz at

RA = 13:25:28.48
Dec = -32:25:32.14

with positional uncertainty of 1.5 arcsec. The position of the radio source is consistent with the candidate optical (de Wet et al., GCN Circ. 32289) and X-ray afterglow (Gropp et al., GCN Circ. 32296) positions.

Further observations with several facilities at different frequencies are ongoing.

We thank CSIRO staff for rapidly scheduling and supporting these observations.

GCN 32618

TITLE: GCN CIRCULAR
NUMBER: 32618
SUBJECT: GRB 220921A: ATCA detection of radio counterpart
DATE: 22/10/03 06:49:53 GMT
FROM: James Leung at U of Sydney/VAST <jleu9465@uni.sydney.edu.au>

James Leung (University of Sydney/CSIRO), Ziteng Wang (University of Sydney/CSIRO), Emil Lenc (CSIRO), Tara Murphy (University of Sydney)

The Australia Telescope Compact Array (ATCA) observed GRB 220921A (Pillera et al., GCN 32568) at multiple frequencies starting on 2022 September 28, from 16:30 to 21:00 UTC (7.2 to 7.4d post-trigger).

We detect a radio source in all bands at the position:
RA (J2000) = 04:25:53.4
Dec (J2000) = -40:24:20.5

with uncertainty 0.5" in each coordinate, which is consistent with the MASTER optical (Lipunov et al., GCN 32570) and ALMA mm (Laskar et al., GCN 32577) candidate afterglow positions.

We report our preliminary flux density measurements below:

Freq (GHz)	Peak Flux Density (micro-Jy/beam)
5.5	163 +/- 19
9.0	364 +/- 17
16.7	763 +/- 50
21.2	988 +/- 95

Ongoing observations are planned.

We thank CSIRO staff for rapidly scheduling and supporting these observations.

GCN 32736

TITLE: GCN CIRCULAR
NUMBER: 32736
SUBJECT: GRB 221009A/Swift J1913.1+1946: low-frequency ASKAP observations
DATE: 22/10/13 10:48:46 GMT
FROM: James Leung at U of Sydney/VAST <jleu9465@uni.sydney.edu.au>

James Leung (University of Sydney/CSIRO), Emil Lenc (CSIRO),
Tara Murphy (University of Sydney)

The Australian Square Kilometre Array Pathfinder (ASKAP) observed the field of GRB 221009A/Swift J1913.1+1946 (Dichiara et al., GCN 32632; Kennea & Williams., GCN 32635; Veres et al., GCN 32636) at 888 MHz on 2022 October 12 from 07:00 to 13:00 UTC (2.70 to 2.95d after the Swift/BAT trigger).

We detect an unresolved radio source at a position consistent with the Swift/UVOT position (Dichiara et al., GCN 32632) with a preliminary flux density measurement of 2.2 +/- 0.1 mJy/beam.

We thank CSIRO staff for rapidly scheduling and supporting these observations.

GCN 32766

TITLE: GCN CIRCULAR
NUMBER: 32766
SUBJECT: GRB 221009A: ATCA radio spectrum
DATE: 22/10/15 23:15:43 GMT
FROM: James Leung at U of Sydney/VAST <jleu9465@uni.sydney.edu.au>

James Leung (University of Sydney/CSIRO), Tara Murphy (University of Sydney), Emil Lenc (CSIRO), Gemma Anderson (Curtin)

We report the radio spectrum for the Australia Compact Telescope Array (ATCA) observations (Bhandari et al., GCN 32763) taken on 2022 October 15 from 05:00 to 11:30 UTC (5.6 to 5.9d after the Swift/BAT trigger).

ATCA observed at 16.7, 21.2, 33, 35, 45 and 47 GHz. In our preliminary analysis, we detect the radio counterpart at each frequency (Trushkin et al., ATel 15671; Bright et al., GCN 32653; Farah et al., GCN 32655; de Ugarte Postigo et al., GCN 32676; Rhodes et al., GCN 32700; Leung et al., GCN 32836; Laskar et al., GCN 32740; Laskar et al., GCN 32757; Urata et al., GCN 32761; Bhandari et al., GCN 32763) at a position consistent with the Swift/UVOT position (Dichiara et al., GCN 32632).

The preliminary flux density measurements are reported below, with uncertainties being purely statistical:

7.1 +/- 0.1 mJy/beam at 16.7 GHz
6.1 +/- 0.1 mJy/beam at 21.2 GHz
4.8 +/- 0.1 mJy/beam at 33 GHz
4.4 +/- 0.1 mJy/beam at 35 GHz
3.6 +/- 0.2 mJy/beam at 45 GHz
3.5 +/- 0.2 mJy/beam at 47 GHz

Ongoing observations are planned.

We thank CSIRO staff for rapidly scheduling, supporting and executing these observations.

The Australia Telescope Compact Array is part of the Australia Telescope National Facility which is funded by the Australian Government for operation as a National Facility managed by CSIRO. We acknowledge the Gomeroi people as the traditional owners of the Observatory site.

GCN 34518

TITLE: GCN CIRCULAR
NUMBER: 34518
SUBJECT: GRB 230815A: ATCA detection of radio counterpart
DATE: 23/08/22 11:44:32 GMT
FROM: James Leung at U of Sydney/VAST <jleu9465@uni.sydney.edu.au>

J. K. Leung (USyd), G. E. Anderson (Curtin), S. D. Ryder (Macquarie), A. J. van der Horst (GWU), A. Gulati (USyd), L. Rhodes (Oxford), S. Chastain (UNM) on behalf of the PanRadio GRB collaboration

The Australia Telescope Compact Array (ATCA) observed long GRB 230815A (Klingler et al., GCN 34434; Mailyan et al., GCN 34440) as part of the ATCA "PanRadio GRB" follow-up Large Project C3542 (PI. Anderson) on 2023-08-17 UT and 2023-08-18 UT.

No radio sources were detected at the GRB location in the first observation conducted from 2023-08-17 02:00 UT for 10 hrs at 5.5, 9.0, 16.7 and 21.2 GHz. The 3-sigma upper limits were 75, 69, 324, 741 microJy/beam, respectively. Note the higher than usual rms was due to bad weather during the observation.

The second observation was conducted from 2023-08-18 22:00 UT for 6 hrs at 5.5, 9.0 and 44 GHz. In our preliminary analysis, we detect a radio counterpart with a flux density of 70+/-10 microJy at 9 GHz. The fitted position is:

RAJ2000 = 12:18:53.2
DECJ2000 = -58:03:09.0
with an uncertainty of 0.3".

This is in broad agreement with previously reported Swift/XRT (Beardmore et al., GCN 34437) and VLT/HAWK-I (Schneider et al., GCN 34467) afterglow positions. There was also a marginal 3 sigma detection at 5.5 GHz (rms=14 microJy/beam) and a non-detection at 44 GHz with a 3-sigma upper limit of 111 microJy/beam.

Further observations are planned.

We thank the CSIRO Space and Astronomy staff for supporting these observations. We acknowledge the Gomeroi people as the traditional owners of the Observatory site. The Australia Telescope Compact Array is
part of the Australia Telescope National Facility (https://ror.org/05qajvd42) which is funded by the Australian Government for operation as a National Facility managed by CSIRO.

Appendix B

The Astronomer's Telegram

I reproduce below a notice I published in The Astronomer's Telegram (ATel) as part of this PhD thesis.

ATCA radio observations of SN 2023bee (ATel #15890)

James Leung (U. Sydney/CSIRO), Luca Izzo (DARK/NBI), Aprajita Hajela (DARK/NBI), Ziteng Wang (ICRAR/Curtin), Katie Auchettl (U. Melbourne), Fabio De Colle (UNAM), Keiichi Maeda (Kyoto U.), Tara Murphy (U. Sydney)

on 6 Feb 2023; 10:33 UT

Credential Certification: Luca Izzo (luca.izzo@gmail.com)

We report radio observations of **SN 2023bee** (**ATel #15882**, **ATel #15883**) conducted with the Australia Telescope Compact Array (ATCA). The observations were conducted from 10:00 to 16:00 UT on 2023 February 4, centered on frequencies 5.5, 9.0, 16.7 and 21.2 GHz. From preliminary analysis, we report non-detections in all observed bands, with the following 3-sigma upper limits: $<$ 84 micro-Jy at 5.5 GHz, $<$ 60 micro-Jy at 9 GHz, $<$ 87 micro-Jy at 16.7 GHz, $<$ 129 micro-Jy at 21.2 GHz.

We thank CSIRO staff for rapidly scheduling, supporting and executing these observations.

Bibliography

Abbott B. P., et al., 2017a, Nature, 551, 85

Abbott B. P., et al., 2017b, ApJ, 848, L13

Abbott B. P., et al., 2019, Phys. Rev. Lett., 123, 011102

Ahumada T., et al., 2021, Nature Astronomy, 5, 917

Ajello M., et al., 2019, ApJ, 878, 52

Akerlof C., et al., 1999, Nature, 398, 400

Alexander K. D., et al., 2020, Space Sci. Rev., 216, 81

Amati L., et al., 2008, MNRAS, 391, 577

Anderson G. E., et al., 2018, MNRAS, 473, 1512

Anumarlapudi A., et al., 2023, arXiv e-prints, p. arXiv:2308.00100

Arnaud K. A., 1996, in Jacoby G. H., Barnes J., eds, Astronomical Society of the Pacific Conference Series Vol. 101, Astronomical Data Analysis Software and Systems V. p. 17

Ashton G., et al., 2019, ApJS, 241, 27

Astropy Collaboration et al., 2013, A&A, 558, A33

Astropy Collaboration et al., 2018, AJ, 156, 123

Atwood W. B., et al., 2009, ApJ, 697, 1071

Barnes J., Kasen D., 2013, ApJ, 775, 18

Barniol Duran R., 2014, MNRAS, 442, 3147

Barniol Duran R., Giannios D., 2015, MNRAS, 454, 1711

Beck R., et al., 2021, MNRAS, 500, 1633

Becker R. H., White R. L., Helfand D. J., 1995, ApJ, 450, 559

Bellm E. C., et al., 2019, PASP, 131, 018002

Beniamini P., Lu W., 2021, ApJ, 920, 109

Beniamini P., Nakar E., 2019, MNRAS, 482, 5430

Beniamini P., van der Horst A. J., 2017, MNRAS, 472, 3161

Beniamini P., et al., 2015, MNRAS, 454, 1073

Berger E., 2009, ApJ, 690, 231

Berger E., et al., 2005, Nature, 438, 988

Berger E., Fong W., Chornock R., 2013, ApJ, 774, L23

Birrer S., Treu T., 2019, MNRAS, 489, 2097

Blaes O. M., Webster R. L., 1992, ApJ, 391, L63

Blanchard P. K., Berger E., Fong W.-f., 2016, ApJ, 817, 144

Blandford R. D., McKee C. F., 1976, Physics of Fluids, 19, 1130

Blandford R. D., Znajek R. L., 1977, MNRAS, 179, 433

Bloom J. S., Kulkarni S. R., Djorgovski S. G., 2002, AJ, 123, 1111

Boella G., et al., 1997, A&AS, 122, 299

Boër M., Gendre B., Stratta G., 2015, ApJ, 800, 16

Bonzini M., et al., 2015, MNRAS, 453, 1079

Bright J. S., et al., 2023, arXiv e-prints, p. arXiv:2303.13583

Bromberg O., et al., 2012, ApJ, 749, 110

Bromberg O., et al., 2013, ApJ, 764, 179

Burlon D., et al., 2016, MNRAS, 459, 3356

CASA Team et al., 2022, PASP, 134, 114501

Camilo F., et al., 2018, ApJ, 856, 180

Cano Z., et al., 2017, Advances in Astronomy, 2017, 8929054

Carilli C. L., Yun M. S., 1999, ApJ, 513, L13

Casadio C., et al., 2021, MNRAS, 507, L6

Cenko S. B., et al., 2011, ApJ, 732, 29

Cenko S. B., et al., 2013, ApJ, 769, 130

Chambers K. C., et al., 2016, arXiv e-prints, p. arXiv:1612.05560

Chandra P., Frail D. A., 2012, ApJ, 746, 156

Chandra P., et al., 2017a, GRB Coordinates Network, 22222, 1

Chandra P., et al., 2017b, GRB Coordinates Network, 22264, 1

Chapman J. M., et al., 2017, in Lorente N. P. F., Shortridge K., Wayth R., eds, Astronomical Society of the Pacific Conference Series Vol. 512, Astronomical Data Analysis Software and Systems XXV. p. 73

Charlot P., et al., 2020, A&A, 644, A159

Chevalier R. A., Li Z.-Y., 2000, ApJ, 536, 195

Christensen L., Hjorth J., Gorosabel J., 2004, A&A, 425, 913

Ciardi B., Loeb A., 2000, ApJ, 540, 687

Clark B. G., 1980, A&A, 89, 377

Cohen E., Piran T., Sari R., 1998, ApJ, 509, 717

Condon J. J., 1992, ARA&A, 30, 575

Condon J. J., et al., 1998, AJ, 115, 1693

Cordes J. M., Lazio T. J. W., 2002, arXiv e-prints, pp astro–ph/0207156

Cornwell T., et al., 2011, ASKAP-SW-0020: ASKAP Science Processing, ASKAP Science Case Memo Series 027, https://www.atnf.csiro.au/projects/askap/ASKAP-SW-0020.pdf

Costa E., et al., 1997a, Nature, 387, 783

Costa E., et al., 1997b, IAU Circ., 6649, 1

Cutri R. M., et al., 2021, VizieR Online Data Catalog, p. II/328

D'Elia V., et al., 2017, GRB Coordinates Network, 22177, 1

D'Elia V., et al., 2018, A&A, 619, A66

Dai Z. G., Lu T., 1998, A&A, 333, L87

Deller A. T., et al., 2007, PASP, 119, 318

Dermer C. D., Chiang J., Böttcher M., 1999, ApJ, 513, 656

Desai D., Metzger B. D., Foucart F., 2019, MNRAS, 485, 4404

Dewdney P. E., et al., 2009, IEEE Proceedings, 97, 1482

Dey A., et al., 2019, AJ, 157, 168

Djorgovski S. G., et al., 2001, ApJ, 562, 654

Dobie D., et al., 2019, PASA, 36, e019

Dobie D., et al., 2022, MNRAS, 510, 3794

Dobie D., et al., 2023, MNRAS, 519, 4684

Driessen L. N., et al., 2023, PASA, 40, e036

Duchesne S. W., et al., 2023, PASA, 40, e034

Eichler D., 2011, ApJ, 730, 41

Eichler D., Waxman E., 2005, ApJ, 627, 861

Eichler D., et al., 1989, Nature, 340, 126

Evans P. A., et al., 2009, MNRAS, 397, 1177

Evans P. A., et al., 2010, A&A, 519, A102

Fender R., et al., 2015, Advancing Astrophysics with the Square Kilometre Array (AASKA14), p. 51

Feng L., et al., 2017, AJ, 153, 98

Fermi GBM Team 2022, GRB Coordinates Network, 32278, 1

Fey A. L., et al., 2015, AJ, 150, 58

Fishman G. J., et al., 1992, in NASA Conference Publication. pp 26–34

Fong W., Berger E., 2013, ApJ, 776, 18

Fong W., et al., 2015, ApJ, 815, 102

Foreman-Mackey D., et al., 2013, PASP, 125, 306

Fox D. B., et al., 2005, Nature, 437, 845

Frail D. A., et al., 1997, Nature, 389, 261

Frail D. A., Waxman E., Kulkarni S. R., 2000, ApJ, 537, 191

Frail D. A., et al., 2001, ApJ, 562, L55

Frail D. A., et al., 2005, ApJ, 619, 994

Frail D. A., et al., 2006, ApJ, 646, L99

Frederiks D., et al., 2022, GRB Coordinates Network, 32295, 1

Fynbo J. P. U., et al., 2006, Nature, 444, 1047

Gal-Yam A., et al., 2006, ApJ, 639, 331

Galama T. J., et al., 1998, Nature, 395, 670

Galama T. J., et al., 2003, ApJ, 585, 899

Gao H., et al., 2013, NewAR, 57, 141

Gehrels N., 1986, ApJ, 303, 336

Gehrels N., et al., 2004, ApJ, 611, 1005

Gehrels N., et al., 2005, Nature, 437, 851

Gehrels N., et al., 2006, Nature, 444, 1044

Gendre B., et al., 2013, ApJ, 766, 30

Ghirlanda G., Salvaterra R., 2022, ApJ, 932, 10

Ghirlanda G., et al., 2013, MNRAS, 435, 2543

Ghirlanda G., et al., 2014, PASA, 31, e022

Ghirlanda G., et al., 2019, Science, 363, 968

Ghisellini G., et al., 2009, MNRAS, 393, 253

Giarratana S., et al., 2022, GRB Coordinates Network, 32454, 1

Giarratana S., et al., 2023, A&A, 670, A35

Goldstein A., et al., 2016, ApJ, 818, 18

Goodman J., 1986, ApJ, 308, L47

Goodman J., 1997, New Astron., 2, 449

Gordon Y. A., et al., 2021, ApJS, 255, 30

Granot J., Sari R., 2002, ApJ, 568, 820

Granot J., van der Horst A. J., 2014, PASA, 31, e008

Granot J., Piran T., Sari R., 1999, ApJ, 513, 679

Granot J., et al., 2018a, MNRAS, 481, 1597

Granot J., De Colle F., Ramirez-Ruiz E., 2018b, MNRAS, 481, 2711

Greiner J., et al., 2015, Nature, 523, 189

Greiner J., et al., 2016, A&A, 593, A17

Greisen E. W., 2003, in Heck A., ed., Astrophysics and Space Science Library Vol. 285, Information Handling in Astronomy - Historical Vistas. p. 109, doi:10.1007/0-306-48080-8_7

Gropp J. D., et al., 2022, GRB Coordinates Network, 32296, 1

Guetta D., Piran T., Waxman E., 2005, ApJ, 619, 412

Gulati A., et al., 2023, PASA, 40, e025

Gupta R., et al., 2022, Journal of Astrophysics and Astronomy, 43, 11

Guzman J., et al., 2019, ASKAPsoft: ASKAP science data processor software, Astrophysics Source Code Library, record `ascl:1912.003`

Hale C. L., et al., 2021, PASA, 38, e058

Hallinan G., et al., 2017, Science, 358, 1579

Hancock P. J., Gaensler B. M., Murphy T., 2013, ApJ, 776, 106

Harris C. R., et al., 2020, Nature, 585, 357

Harrison F. A., et al., 1999, ApJ, 523, L121

Heise J., et al., 1997, IAU Circ., 6654, 2

Hjorth J., et al., 2003, Nature, 423, 847

Hjorth J., et al., 2005, Nature, 437, 859

Ho A. Y. Q., et al., 2020a, ApJ, 895, 49

Ho A. Y. Q., et al., 2020b, ApJ, 902, 86

Ho A. Y. Q., et al., 2022, ApJ, 938, 85

Högbom J. A., 1974, A&AS, 15, 417

Horesh A., et al., 2015, ApJ, 812, 86

Horesh A., Cenko S. B., Arcavi I., 2021, Nature Astronomy, 5, 491

Hotan A. W., et al., 2021, PASA, 38, e009

Hotokezaka K., et al., 2019, Nature Astronomy, 3, 940

Huang Y. F., Dai Z. G., Lu T., 2002, MNRAS, 332, 735

Huang Y.-Y., et al., 2022, ApJ, 940, L36

Hunter J. D., 2007, Computing in Science and Engineering, 9, 90

Hurley-Walker N., et al., 2017, MNRAS, 464, 1146

Huynh M., et al., 2020, in Ballester P., et al., eds, Astronomical Society of the Pacific Conference Series Vol. 522, Astronomical Data Analysis Software and Systems XXVII. p. 263

Ighina L., et al., 2022, A&A, 663, A73

Ighina L., et al., 2023, MNRAS, 519, 2060

Intema H. T., et al., 2017, A&A, 598, A78

Izzo L., et al., 2017, GRB Coordinates Network, 22180, 1

Izzo L., et al., 2019, Nature, 565, 324

Izzo L., et al., 2020, A&A, 639, L11

Izzo L., et al., 2022, GRB Coordinates Network, 32291, 1

Johnston S., et al., 2007, PASA, 24, 174

Jonas J., MeerKAT Team 2016, in MeerKAT Science: On the Pathway to the SKA. p. 1, doi:10.22323/1.277.0001

Kalantari Z., et al., 2021, ApJ, 922, 77

Katz C. A., Moore C. B., Hewitt J. N., 1997, ApJ, 475, 512

Kent B. R., et al., 2020, in Pizzo R., et al., eds, Astronomical Society of the Pacific Conference Series Vol. 527, Astronomical Data Analysis Software and Systems XXIX. p. 571

Kesteven M. J. L., Bridle A. H., Brandie G. W., 1976, AJ, 81, 919

Kistler M. D., et al., 2009, ApJ, 705, L104

Klebesadel R. W., Strong I. B., Olson R. A., 1973, ApJ, 182, L85

Kouveliotou C., et al., 1993, ApJ, 413, L101

Krauss L. M., Small T. A., 1991, ApJ, 378, 22

Kulkarni S. R., et al., 1998, Nature, 395, 663

Kulkarni S. R., et al., 1999, ApJ, 522, L97

Lacy M., et al., 2020, PASP, 132, 035001

Lacy M., et al., 2022, VLASS Project Memo #13: Pilot and Epoch 1 Quick Look Data Release (v2), https://library.nrao.edu/public/memos/vla/vlass/VLASS_013.pdf

Lamb G. P., et al., 2021, Universe, 7, 329

Laskar T., et al., 2017, GRB Coordinates Network, 22216, 1

Laskar T., et al., 2019, ApJ, 884, 121

Laskar T., Hull C. L. H., Cortes P., 2020, ApJ, 895, 64

Law C. J., et al., 2018, ApJ, 866, L22

Lemoine M., Li Z., Wang X.-Y., 2013, MNRAS, 435, 3009

Leung J., et al., 2020, GRB Coordinates Network, 27812, 1

Leung J. K., et al., 2021a, MNRAS, 503, 1847

Leung J., et al., 2021b, GRB Coordinates Network, 29640, 1

Leung J., et al., 2021c, GRB Coordinates Network, 30324, 1

Leung J., et al., 2022a, GRB Coordinates Network, 32341, 1

Leung J., et al., 2022b, GRB Coordinates Network, 32618, 1

Leung J., Lenc E., Murphy T., 2022c, GRB Coordinates Network, 32736, 1

Leung J., et al., 2022d, GRB Coordinates Network, 32766, 1

Leung J. K., et al., 2023a, MNRAS, 523, 4029

Leung J., et al., 2023b, The Astronomer's Telegram, 15890, 1

Leung J. K., et al., 2023c, GRB Coordinates Network, 34518, 1

Levan A. J., et al., 2014, ApJ, 781, 13

Levan A. J., et al., 2023, arXiv e-prints, p. arXiv:2303.12912

Levinson A., et al., 2002, ApJ, 576, 923

Li Z.-Y., Chevalier R. A., 1999, ApJ, 526, 716

Li L.-X., Paczyński B., 1998, ApJ, 507, L59

Liang E., et al., 2007, ApJ, 662, 1111

Lien A., et al., 2016, ApJ, 829, 7

Lin S.-J., et al., 2022, ApJ, 931, 4

Lipunov V. M., et al., 2022, Astronomy Letters, 48, 623

Lloyd-Ronning N. M., Fryer C. L., 2017, MNRAS, 467, 3413

Lloyd-Ronning N. M., et al., 2019, ApJ, 871, 118

MacFadyen A. I., Woosley S. E., 1999, ApJ, 524, 262

Maindonald J., Braun W. J., 2006, Data Analysis and Graphics Using R: An Example-Based Approach. Cambridge University Press

Maity B., Chandra P., 2021, ApJ, 907, 60

Mao S., 1992, ApJ, 389, L41

Marcote B., et al., 2019, ApJ, 876, L14

Marscher A. P., Gear W. K., 1985, ApJ, 298, 114

Mauch T., et al., 2003, MNRAS, 342, 1117

Mazzali P. A., et al., 2014, MNRAS, 443, 67

McConnell D., et al., 2020, PASA, 37, e048

McKinney W., 2010, in Stéfan van der Walt Jarrod Millman eds, Proceedings of the 9th Python in Science Conference. pp 56–61, doi:10.25080/Majora-92bf1922-00a

McMullin J. P., et al., 2007, in Shaw R. A., Hill F., Bell D. J., eds, Astronomical Society of the Pacific Conference Series Vol. 376, Astronomical Data Analysis Software and Systems XVI. p. 127

Meegan C. A., et al., 1992, Nature, 355, 143

Meegan C., et al., 2009, ApJ, 702, 791

Mei A., et al., 2022, Nature, 612, 236

Mereghetti S., et al., 2003, A&A, 411, L291

Mészáros P., Rees M. J., 1997, ApJ, 476, 232

Metzger B. D., 2019, Living Reviews in Relativity, 23, 1

Metzger M. R., et al., 1997, Nature, 387, 878

Metzger B. D., Quataert E., Thompson T. A., 2008, MNRAS, 385, 1455

Metzger B. D., et al., 2010, MNRAS, 402, 2771

Metzger B. D., Williams P. K. G., Berger E., 2015, ApJ, 806, 224

Minniti D., et al., 2010, New Astron., 15, 433

Minniti D., Lucas P., VVV Team 2017, VizieR Online Data Catalog, p. II/348

Modjaz M., et al., 2016, ApJ, 832, 108

Mooley K. P., et al., 2013, ApJ, 768, 165

Mooley K. P., et al., 2016, ApJ, 818, 105

Mooley K. P., et al., 2018, Nature, 561, 355

Mooley K. P., et al., 2022, ApJ, 924, 16

Mukherjee O., Nemiroff R. J., 2023, arXiv e-prints, p. arXiv:2301.09436

Murphy T., et al., 2010, MNRAS, 402, 2403

Murphy T., et al., 2013, PASA, 30, e006

Murphy E. J., et al., 2018, in Murphy E., ed., Astronomical Society of the Pacific Conference Series Vol. 517, Science with a Next Generation Very Large Array. p. 3, doi:10.48550/arXiv.1810.07524

Murphy T., et al., 2021, PASA, 38, e054

Nakar E., 2015, ApJ, 807, 172

Nakar E., Piran T., 2011, Nature, 478, 82

Narayan R., Paczynski B., Piran T., 1992, ApJ, 395, L83

Nicuesa Guelbenzu A., Klose S., Rau A., 2022, GRB Coordinates Network, 32304, 1

Norris R. P., 2016, PASA, 33, e039

Norris R. P., et al., 2011, PASA, 28, 215

O'Dell S. L., 1988, ApJ, 327, 60

Odewahn S. C., et al., 1998, ApJ, 509, L5

Oguri M., 2019, Reports on Progress in Physics, 82, 126901

Onken C. A., et al., 2019, PASA, 36, e033

Paczynski B., 1986, ApJ, 308, L43

Paczyński B., 1998, ApJ, 494, L45

Panaitescu A., Kumar P., 2000, ApJ, 543, 66

Panaitescu A., Kumar P., 2001, ApJ, 560, L49

Paragi Z., et al., 2015, in Proceedings of Advancing Astrophysics with the Square Kilometre Array — PoS(AASKA14). p. 143 (`arXiv:1412.5971`), doi:10.22323/1.215.0143

Paynter J., Webster R., Thrane E., 2021, Nature Astronomy, 5, 560

Perets H. B., Beniamini P., 2021, MNRAS, 503, 5997

Perez-Torres M., et al., 2018a, GRB Coordinates Network, 22302, 1

Perez-Torres M., et al., 2018b, GRB Coordinates Network, 22350, 1

Perley D. A., Taggart K., 2017, GRB Coordinates Network, 22194, 1

Perley D. A., Schulze S., de Ugarte Postigo A., 2017, GRB Coordinates Network, 22252, 1

Peters C., et al., 2019, ApJ, 872, 28

Pian E., et al., 2000, ApJ, 536, 778

Pintaldi S., et al., 2022, in Ruiz J. E., Pierfedereci F., Teuben P., eds, Astronomical Society of the Pacific Conference Series Vol. 532, Astronomical Society of the Pacific Conference Series. p. 333 (arXiv:2101.05898)

Piran T., 2004, Reviews of Modern Physics, 76, 1143

Planck Collaboration et al., 2016, A&A, 594, A13

Planck Collaboration et al., 2020, A&A, 641, A6

Podsiadlowski P., Rees M. J., Ruderman M., 1995, MNRAS, 273, 755

Pritchard J., et al., 2021, MNRAS, 502, 5438

Raman G., et al., 2022, GRB Coordinates Network, 32287, 1

Rastinejad J. C., et al., 2022, Nature, 612, 223

Rees M. J., Mészáros P., 1992, MNRAS, 258, 41P

Rees M. J., Mészáros P., 1998, ApJ, 496, L1

Refsdal S., 1964, MNRAS, 128, 307

Reynolds J., 1994, A Revised Flux Scale for the AT Compact Array, https://www.atnf.csiro.au/observers/memos/d96783~1.pdf

Rhoads J. E., 1997, ApJ, 487, L1

Rhoads J. E., 1999, ApJ, 525, 737

Rhoads J. E., 2003, ApJ, 591, 1097

Rhodes L., et al., 2020, MNRAS, 496, 3326

Ricci R., et al., 2021, MNRAS, 500, 1708

Roberts O. J., et al., 2022, GRB Coordinates Network, 32288, 1

Robson E. I., et al., 1983, Nature, 305, 194

Roming P. W. A., et al., 2017, ApJS, 228, 13

Rossi E., Lazzati D., Rees M. J., 2002, MNRAS, 332, 945

Rossi E. M., Perna R., Daigne F., 2008, MNRAS, 390, 675

Rossi A., et al., 2022, ApJ, 932, 1

Rowlinson A., et al., 2019, Astronomy and Computing, 27, 111

Ruderman M., 1975, in Bergman P. G., Fenyves E. J., Motz L., eds, Annals of the New York Academy of Sciences Vol. 262, Seventh Texas Symposium on Relativistic Astrophysics. pp 164–180, doi:10.1111/j.1749-6632.1975.tb31430.x

Russell T. D., et al., 2020, MNRAS, 498, 5772

Ryan G., et al., 2015, ApJ, 799, 3

Salafia O. S., Ghirlanda G., 2022, Galaxies, 10, 93

Salafia O. S., et al., 2016, MNRAS, 461, 3607

Salvaterra R., 2015, Journal of High Energy Astrophysics, 7, 35

Santana R., Barniol Duran R., Kumar P., 2014, ApJ, 785, 29

Sari R., 1997, ApJ, 489, L37

Sari R., Piran T., 1999, ApJ, 520, 641

Sari R., Narayan R., Piran T., 1996, ApJ, 473, 204

Sari R., Piran T., Narayan R., 1998, ApJ, 497, L17

Sari R., Piran T., Halpern J. P., 1999, ApJ, 519, L17

Sarin N., et al., 2021, arXiv e-prints, p. arXiv:2105.10108

Sarin N., et al., 2022, MNRAS, 512, 1391

Sault R. J., Wieringa M. H., 1994, A&AS, 108, 585

Sault R. J., Teuben P. J., Wright M. C. H., 1995, in Shaw R. A., Payne H. E., Hayes J. J. E., eds, Astronomical Society of the Pacific Conference Series Vol. 77, Astronomical Data Analysis Software and Systems IV. p. 433

Scheers L. H. A., 2011, PhD thesis, University of Amsterdam

Shepherd M. C., 1997, in Hunt G., Payne H., eds, Astronomical Society of the Pacific Conference Series Vol. 125, Astronomical Data Analysis Software and Systems VI. p. 77

Shimwell T. W., et al., 2017, A&A, 598, A104

Sironi L., Giannios D., 2013, ApJ, 778, 107

Sironi L., Spitkovsky A., 2011, ApJ, 726, 75

Smith I. A., Tanvir N. R., 2017, GRB Coordinates Network, 22242, 1

Soderberg A. M., et al., 2006, ApJ, 638, 930

Speagle J. S., 2020, MNRAS, 493, 3132

Spingola C., et al., 2019, MNRAS, 483, 2125

Stanek K. Z., et al., 2003, ApJ, 591, L17

Suresh A., et al., 2022, GRB Coordinates Network, 32316, 1

Suzuki A., Maeda K., Shigeyama T., 2019, ApJ, 870, 38

Swinbank J. D., et al., 2015, Astronomy and Computing, 11, 25

Tanvir N. R., et al., 2013, Nature, 500, 547

Taylor J. H., Weisberg J. M., 1982, ApJ, 253, 908

Taylor G. B., Carilli C. L., Perley R. A., 1999, in Synthesis Imaging in Radio Astronomy II.

Taylor G. B., et al., 2004, ApJ, 609, L1

Thompson A. R., Moran J. M., Swenson George W. J., 2017, Interferometry and Synthesis in Radio Astronomy, 3rd Edition. Springer, doi:10.1007/978-3-319-44431-4

Tingay S. J., et al., 2003, PASJ, 55, 351

Tohuvavohu A., et al., 2020, ApJ, 900, 35

Toma K., Sakamoto T., Mészáros P., 2011, ApJ, 731, 127

Troja E., et al., 2022, Nature, 612, 228

Trushkin S. A., et al., 2017, GRB Coordinates Network, 22258, 1

Urata Y., et al., 2019, ApJ, 884, L58

Urry C. M., Padovani P., 1995, PASP, 107, 803

Verde L., Treu T., Riess A. G., 2019, Nature Astronomy, 3, 891

Veres P., et al., 2021, ApJ, 921, L30

Virgili F. J., et al., 2013, ApJ, 778, 54

Virtanen P., et al., 2020, Nature Methods, 17, 261

Walker M. A., 1998, MNRAS, 294, 307

Wang L., Höflich P., Wheeler J. C., 1997, ApJ, 483, L29

Wang X.-G., et al., 2015, ApJS, 219, 9

Wang J., et al., 2018, ApJ, 867, 147

Wang Y., et al., 2021a, ApJ, 918, L34

Wang Z., et al., 2021b, ApJ, 920, 45

Wang Z., et al., 2022, MNRAS, 516, 5972

Waxman E., 2004, ApJ, 602, 886

Waxman E., Kulkarni S. R., Frail D. A., 1998, ApJ, 497, 288

Weisberg S., 2005, Applied Linear Regression, 3 edn. John Wiley & Sons

Whiting M., Humphreys B., 2012, PASA, 29, 371

Wilms J., Allen A., McCray R., 2000, ApJ, 542, 914

Woosley S. E., 1993, ApJ, 405, 273

Woudt P. A., et al., 2018, in Proceedings of MeerKAT Science: On the Pathway to the SKA — PoS(MeerKAT2016). p. 013, doi:10.22323/1.277.0013

Wright E. L., et al., 2010, AJ, 140, 1868

Xie C., et al., 2016, ApJ, 824, L17

Xu F., Huang Y.-F., Geng J.-J., 2023, arXiv e-prints, p. arXiv:2304.09051

Yang X., et al., 2021, ApJ, 921, L29

Zauderer B. A., et al., 2011, Nature, 476, 425

Zhang B. B., et al., 2021, Nature Astronomy, 5, 911

Zhao F.-Y., Strom R. G., Jiang S.-Y., 2006, ChJAA, 6, 635

Zheng H., et al., 2017, MNRAS, 464, 3486

Zhou R., et al., 2021, MNRAS, 501, 3309

de Ruiter H. R., Willis A. G., Arp H. C., 1977, A&AS, 28, 211

de Ugarte Postigo A., et al., 2017a, GRB Coordinates Network, 22187, 1

de Ugarte Postigo A., et al., 2017b, GRB Coordinates Network, 22204, 1

de Wet S., et al., 2022, GRB Coordinates Network, 32289, 1

di Lalla N., et al., 2022, GRB Coordinates Network, 32283, 1

van Eerten H. J., MacFadyen A. I., 2011, ApJ, 733, L37

van Paradijs J., et al., 1997, Nature, 386, 686

van Velzen S., et al., 2012, A&A, 544, A18

van der Horst A. J., et al., 2008, A&A, 480, 35

van der Horst A. J., et al., 2014, MNRAS, 444, 3151

von Kienlin A., et al., 2020, ApJ, 893, 46